Title
Identification and Control of a Magnetic Bearing System for Boring Application

Author
Rai, Sandeep

Publication Date
2018

Peer reviewed|Thesis/dissertation

UNIVERSITY OF CALIFORNIA

Los Angeles

Identification and Control of a Magnetic Bearing System for Boring Application

A dissertation submitted in partial satisfaction
of the requirements for the degree
Doctor of Philosophy in Mechanical Engineering

by

Sandeep Singh Rai

2018

ABSTRACT OF THE DISSERTATION

Identification and Control of a Magnetic Bearing System for Boring Application

by

Sandeep Singh Rai
Doctor of Philosophy in Mechanical Engineering
University of California, Los Angeles, 2018
Professor Tsu-Chin Tsao, Chair

This dissertation presents modeling, identification, fault detection, and control of an active magnetic bearing system, and the experimental results for applications in metal cutting and dynamic vibration suppression. A high order ARX identification method conducted within stabilized feedback loops followed by balanced truncation model reduction was efficient and effective in obtaining the open loop unstable multivariable AMBS dynamic model, which agrees well with the system's frequency response data. Also the severe flexible nature of the spindle is seen in the frequency response both while stationary and spinning, which facilitates the need for robust controller design. The experimentally obtained model is augmented to include the tip dynamics by impulse hammer testing that allows for the inclusion on cutting dynamics into the overall control system.

In cutting application there are two main concerns: the tip tracking a profile and avoidance of chatter instability. Therefore, based on the identified model, a two-step optimal repetitive controller was designed for minimal error tracking. The first controller consisted of a control input weighted linear quadratic control with integral action that ensured stability, broadband performance, and robustness. Then a plug-in multivariable repetitive controller with modifications for enhanced performance and non-harmonic compensation was designed by optimal model matching that highlights the classical trade-off between robustness and performance. A cutting force model was incorporated into the overall system, and stability lobes obtained for optimal cutting conditions.

Vibration reduction is crucial in applications of magnetic bearings such as energy storage. An adaptive feedforward control was seen to be effective in reducing housing vibrations even while the spin frequency is changing. The regressors were filtered through a multivariable filter obtained from gradient descent. The adaptive controller has a linear time invariant state space representation from which the deviations of the add-on adaptive from the nominal sensitivity and complementary sensitivity can be analyzed. Experimental results did indeed show that vibrations can be reduced even while the spindle speed is changing.

The single input single output adaptive inverse control was extended to the multivariable case and demonstrated to be effective in rejecting narrow and broadband disturbances. Two formulations that can accommodate multivariable plants were considered: the receding horizon adaptive control and the decoupling adaptive control. Both methods need a multivariable adaptive filter such as RLS or LMS; in this thesis a multivariable lattice RLS filter was chosen for its numerical stability and $O(N)$ complexity. Experimental results on the magnetic bearing system show the effectiveness of both control schemes.

Lastly, there were two main results for the standard single phase boost rectifier: 1) The formulation of a linear model in the DQ domain suitable for controller design 2) A MIMO repetitive add-on controller with peak filter modification was designed using the linear model to reduce harmonics not compensated for by a nominal controller. In the process of deriving the linear model, analysis of the equilibrium points gave the boost condition for the rectifier. Experimental results proved the effectiveness of using the linear model for controller design and the repetitive controller for reducing harmonics. The methodology can be used for designing controllers that operate at near unity power factor.

The dissertation of Sandeep Singh Rai is approved.

Lieven Vandenberghe

Robert Thomas M'Closkey

James S Gibson

Tsu-Chin Tsao, Committee Chair

University of California, Los Angeles

2018

Table of Contents

1 Introduction 1

1.1 Geometrical Centering Using Repetitive Control Applied to Cutting 2

1.2 Inertial Balancing Using Adaptive Feedforward Control 3

1.3 Adaptive Internal Model for Varying Narrow Band Rejection 4

1.4 Unknown Disturbance Rejection for Geometrical Centering 4

1.5 Boost Rectifier 4

2 System Description, Identification, and Stabilizing Control for Active Magnetic Bearing 6

2.1 System Description 7

2.2 Bias Current and Linearization 8

2.3 System Identification 9

2.3.1 High-Order Multivariable ARX Identification 9

2.3.2 Non-Parametric Frequency Domain Identification 11

2.3.3 High-Order Results 12

2.3.4 Reduced Order Results 14

2.3.5 Flexible Modes and Frequencies 16

2.3.6 Gyroscopic Effect 19

2.4 Tip Dynamics Identification 21

2.4.1 Experimental Set-up for Tip Dynamics Identification 22

2.4.2 Static Calibration 23

2.4.3 Impulse Hammer Identification 25

2.5 Frequency Weighted LQGi 30

2.5.1 Linear Quadratic Control Design 30
2.5.2 Sensitivity and Robustness of LQGi 32

3 Orbital Motion Tracking 36
3.1 Repetitive Control Design 36
3.1.1 H_∞ minimization 39
3.1.2 Repetitive Control Sensitivity and Robustness 40
3.2 Repetitive Control with Peak Filter 43
3.2.1 Peak Filter Sensitivity and Robustness 44
3.3 Peak Filter with Phase Compensation 46
3.3.1 Peak Filter with Phase Compensation Sensitivity and Robustness . . 47
3.4 Experimental Results 49
3.4.1 Repetitive Control and LQGi 49
3.4.2 Peak Filter Modification 53
3.4.3 Peak Filter with Phase Compensation 56
3.4.4 Circles, Ovals, and Control Effort 58
3.4.5 Tip Tracking 62

4 Cutting Process 64
4.1 Reference Generation 64
4.2 Overall Cutting Process 65
4.2.1 Chatter Model 66
4.2.2 Stability Lobes 68
4.3 Experimental Results 70
4.3.1 Vibration Levels 73
4.3.2 Tracking Error 74

4.4 Fault Detection 78

5 Vibration Suppression 79

5.1 Problem Setup and Adaptive Algorithm 79

5.1.1 SISO Adaptive Feedforward 82

5.2 LTI Equivalent Controller 83

5.2.1 Stability and Convergence Rate 84

5.2.2 Sensitivity Transfer Functions 84

5.3 Implementation Details 85

5.4 LTI Equivalent Analysis 85

5.4.1 SISO vs MIMO Adaptive Feedforward Algorthm 86

5.4.2 Multiple Frequency Analysis 87

5.5 Magnetic Bearing Spin Results 92

5.5.1 Transient Spin-up Vibration Reduction 92

5.5.2 Steady-State Vibration Reduction 95

5.5.3 Two Frequency Control Input Reduction 97

6 Geometrical Centering of Varying Frequencies 99

6.1 Problem Setup 100

6.1.1 Internal Model 101

6.1.2 Inversion Filter 102

6.1.3 Disturbance Observer 103

6.1.4 Frequency Estimation 104

6.2 Experimental Results 105

6.2.1 Tuning 106

6.2.2 Spin up with Single Frequency Internal Model 107

6.2.3 Spin up and Constant Frequency with Two Internal Model 110
6.2.4 Spin up and Double Frequency with Two Internal Model 113
6.2.5 Spin up and Ramp with Two Internal Model 116

7 Unknown Multivariable Narrow and Broadband Disturbance Rejection 119
7.1 Introduction 119
7.2 Problem Setup 120
7.3 Receding Horizon Adaptive Control 121
7.3.1 Computing Optimal Gains 123
7.3.2 Adaptive Prediction 124
7.3.3 Multichannel Lattice RLS 124
7.3.4 Results 128
7.4 Receding Horizon as Delayed Inverse 135
7.5 Decoupling Adaptive Disturbance Rejection 136
7.5.1 Inverse Design 136
7.5.2 Adaptive Prediction 138
7.5.3 Results 138
7.5.4 Analysis of Decoupling Approach 141

8 Boost Rectifier for THD Minimization 143
8.1 Introduction 143
8.2 Modelling and System ID 145
8.2.1 Sinusoidal PWM and Sampling Synchronization 145
8.2.2 State Space Model and System Identification 146
8.3 DQ Linearized Model 148
8.3.1 DQ Model for Boost Rectifier 149

8.3.2 Equilibrium Points and Linearization 150
8.4 PI, Repetitive, and Resonator Control 151
8.4.1 PI Control 151
8.4.2 Repetitive Add-On 151
8.4.3 Resonator Add-on 153
8.4.4 Outer Voltage Loop 156
8.5 Experimental Results 156
8.5.1 Experiment Setup 156
8.5.2 Experimental Results 157
8.6 Conclusion 162

9 Conclusions and Future Directions 163

References 165

List of Figures

2.1 Picture of the magnetic bearing system considered in this paper 7

2.2 Schematic of the magnetic bearing system 7

2.3 Block diagram of the overall system 8

2.4 First 40 Hankel Singular Values of high order state space model 12

2.5 The effect of the number of data points chosen for the high order identification. The higher the number of data points, the better the identification. 13

2.6 The effect of the order chosen for the high order ARX model. The higher the order, the better the identification. 13

2.7 Multiplicative error comparison of open loop plant using two different high-order arx techniques and the high order model compared to the frequency response data 14

2.8 Error using low order models, reduced from the high order model 15

2.9 Multiplicative error bound used for robustness analysis 16

2.10 Singular values of the open loop plant model and frequency response data highlighting the flexible modes 17

2.11 The imaginary part of the frequency response at the 1 kHz resonant mode. . 18

2.12 Pictorial illustration of the first mode shape. 18

2.13 Singular Values of the frequency response for different rotor speeds near the 1^{st} natural mode 19

2.14 Singular Values of the frequency response for different rotor speeds near the 2^{st} natural mode 20

2.15 The top plot shows the 1^{st} mode splitting as the rotor speed is increased from 100 to 700 Hz, while the bottom shows the 2^{nd} mode. 21

2.16 Structure for the identification of plant and tip dynamics 21

2.17 Picture of the eddy current and impulse hammer set up at the tip. 23

2.18 Simple Kinematics for the static calibration tests. 23

2.19 Calibration results of the static test, showing both the fitted parameters and the experimental results when in translation and rotation. 24

2.20 Experimental impulse hammer test, showing the hammer impact, feedback sensor, and the tip sensor. 26

2.21 The experimental magnitude of the frequency response and identified model from the impact force to feedback sensor output. 27

2.22 The experimental phase of the frequency response and identified model from the impact force to feedback sensor output. 28

2.23 The experimental magnitude of the frequency response and identified model from the impact force to tip sensor output. 28

2.24 The experimental phase of the frequency response and identified model from the impact force to feedback sensor output. 29

2.25 Nominal plant model and controller for sensitivity analysis 32

2.26 Uncertain plant model and controller for robustness analysis 33

2.27 High-pass weighting transfer on the input used to increase robustness. The weighting is a broad-band high pass and a narrow band peak filter at the second resonant mode 33

2.28 Sensitivity of the LQGi feedback controller. The frequency weighting does not affect the performance too much 34

2.29 Robustness of the LQGi feedback controller. Adding frequency weighting attenuates high frequency control action that increases robustness 34

2.30 Step Responses of LQGi Controller, Experiment and Simulation. 35

3.1 Block Diagram of the Plug-in Repetitive Control 37

3.2 Equivalent Block Diagram of the Plug-in Repetitive Control suitable for small gain theorem 38

3.3 γ iterations finds the transfer function to minimize e and obtain an inversion filter for repetitive control 39

3.4 Robustness analysis of the repetitive design procedure varying the scalar control input weight 41

3.5 Sensitivity/performance analysis of the repetitive design while varying the control input weighting 42

3.6 Gain of the inversion filter while varying the control input weighting 42

3.7 Internal model modification with peak filter 43

3.8 Robustness analysis of the repetitive design procedure with the peak filter modification compared against classical repetitive and LQGi 45

3.9 Sensitivity/performance analysis of the repetitive design procedure with the peak filter modification compared against classical repetitive and LQGi . . . 45

3.10 Internal model modification with peak filter and phase compensation 46

3.11 Robustness analysis of the repetitive design procedure with the peak filter modification compared against classical repetitive and LQGi 48

3.12 Sensitivity/performance analysis of the repetitive design procedure with the peak filter modification compared against classical repetitive and LQGi . . . 48

3.13 200Hz Tracking Results–the spindle is tracking a 200 Hz reference on its front two axis while not spinning 50

3.14 200Hz Disturbance Rejection Results–the spindle is spinning without any reference 51

3.15 200Hz Reference and Disturbance Rejection Results – the spindle is spinning and a 200 Hz reference injected on its front two axis 52

3.16 200Hz Reference and Disturbance Rejection Results – the spindle is only spinning on the top and spinning while tracking on the bottom 54

3.17 400Hz Reference and Disturbance Rejection Results – the spindle is only spinning on the top and spinning while tracking on the bottom 55

3.18 200Hz Reference and Disturbance Rejection Results – the spindle is only spinning on the top and spinning while tracking on the bottom 57

3.19 400Hz Reference and Disturbance Rejection Results – the spindle is only spinning on the top and spinning while tracking on the bottom 57

3.20 The top two plots is tracking a circle profile at 200 Hz by translating both the front and rear axis (translational), while the bottom is tracking a circle by tracking a circle on the front and regulating the rear (Rotational). Clearly, the repetitive control with peak filter is able to track circles while the LQGi cannot. 58

3.21 The control signal of each of the four axis when tracking a circle using repetitive control. Tracking at both and front and rear (Translational) is compared to only tracking at the front while regulating the rear (Rotational). 59

3.22 The top two plots is tracking an oval profile at 200 Hz by translating both the front and rear axis (translational), while the bottom is tracking an oval by tracking a circle on the front and regulating the rear (Rotational). 60

3.23 The control signal of each of the four axis when tracking an oval using repetitive control. Tracking at both and front and rear (Translational) is compared to only tracking at the front while regulating the rear (Rotational). 61

3.24 Tracking at the tip using LQGi and repetitive control for both a circle and oval at 100 Hz, the spindle is not spinning. 62

3.25 Tracking at the tip using LQGi and repetitive control for both a circle and oval at 200 Hz, the spindle is not spinning. 63

4.1 Simple kinematics of the tracking problem for cutting 64

4.2 Overall block diagram of the linearized cutting process with the three main parts: 1) augmented plant with tip dynamics 2) internal model control for reference tracking 3) cutting dynamics 65

4.3 Simplified siso model for the prediction of chatter instability 68

4.4 Stability lobe diagram for the LQGi and repetitive controller 69

4.5 The crossover frequency at which instability occurs for the magnetic bearing system with cutting model 70

4.6 Vibration levels of the control input for various depth of cuts at a feed rate of 1.7 mm/s, no chatter was seen 71

4.7 Summary of the experiments conducted at a depth of cut of 20 μm to verify the validity of the stability lobe diagram. No chatter was observed when cutting at 150 Hz as the instability limit was approaching threading. 72

4.8 Actual workpieces: the left is a clean cut, and the right is a chattered piece. 72

4.9 Vibration levels of the control input for various feed rates at 20μm depth of cuts and a spin frequency of 100 Hz, chatter was seen at a feed rate of 3.5 mm/s 73

4.10 Vibration levels of the control input for various feed rates at 20μm depth of cuts and a spin frequency of 150 Hz, chatter was not observed at the higher spin frequency 74

4.11 Tracking results from a 20 μm circle cut that did not chatter. The top plots shows the error spectrum with and without cutting. The bottom plots show the feedback sensors tracking; the front sensors track a circle (blue) while the back regulates to zero (red). 75

4.12 Tracking results from a 20 μm circle cut that did chatter. The top plots shows the error spectrum with and without cutting. The bottom plots show the feedback sensors tracking; the front sensors track a circle (blue) while the back regulates to zero (red). 76

4.13 Tracking results from a 20/40 μm oval cut that did not chatter. The top plots shows the error spectrum with and without cutting. The bottom plots show the feedback sensors tracking; the front sensors track an oval (blue) while the back regulates to zero (red). 77

4.14 The fault detection scheme 78

5.1 Block diagram of the adaptive feedforward controller with sinusoidal regressors 79

5.2 Equivalent LTI feedback control system for the adaptive feedforward controller 84

5.3 Plot of the maximum eigenvalue versus the learning gain for several disturbance frequencies. The top plot is the MIMO AFC algorthm, while the bottom is the standard SISO AFC. 87

5.4 The top plot is the maximum singular value of the complementary sensitivity transfer function for various learning gains, while the bottom is the sensitivity. The disturbance frequency is 100 Hz 88

5.5 The top plot is the maximum singular value of the complementary sensitivity transfer function for various disturbance frequencies, while the bottom is the sensitivity. The learning gain is 100 89

5.7 The top plot is the maximum singular value of the complementary sensitivity transfer function for a single frequency, while the bottom is the complementary sensitivity for two frequencies at various learning gains and a disturbance frequency of 100 Hz. 89

5.6 The top plot is the maximum eigenvalue value of the overall LTI equivalent system for various disturbance frequencies, while the bottom is the maximum singular value of the overall LTI equivalent system for the same disturbance frequencies and its harmonic. 90

5.8 The top plot is the maximum singular value of the sensitivity transfer function for a single frequency, while the bottom is the sensitivity for two frequencies at various learning gains. 90

5.9 Short-time fft plot of the control input for a single channel (others are similar) during a transient spin-up to 500 Hz. The top is without the adaptive controller, while the bottom is with the adaptive controller turned on for a μ value of 20. 93

5.10 The weights for a single channel (others are similar) during the transient spin-up. The top is the weight corresponding to the sine term and bottom is the weight corresponding to the cosine term. 94

5.11 Short-time fft plot of the accelerometer mounted on the housing with and without the adaptive controller during the transient. 95

5.12 Power Spectral Density of the control input for one channel with the spindle spinning at 500 Hz and the controller converged. The blue shows the control input without adaptive and the green with adaptive. 96

5.13 Power Spectral Density of the accelerometer mounted on the housing while the spindle is spinning at 500 Hz.The blue shows the control input without adaptive and the green with adaptive. 96

5.14 Power Spectral Density of the control input for one channel, while the spindle was spinning at 250 Hz. The blue is without the AFC algorthm, the green is the one frequency AFC algorthm, and the red is the two frequency AFC algorthm. 98

6.1 Set-up of the unknown sinusoidal disturbance/reference problem 100

6.2 The internal model is updated as estimations of the disturbance frequencies is computed. 101

6.3 Rearrangement of the overall control scheme suitable for small gain, in the adaptive case the filter $L(z)$ is time-varying. 102

6.4 Lattice structure for the all pass state,θ_1 controls the location of the notch and is adaptive to minimize the error while θ_1 determines the bandwidth of the notch. 104

6.5 Single frequency adaptive frequency estimation algorithm can be cascaded to estimate multiple frequencies provided the bandwidth is small. 105

6.6 The frequency estimates during spin up and down from both the adaptive algorithm and from the encoder. 107

6.7 Time domain of the output of each of the four axis for the three controllers. The adaptive estimation performs just as well as encoder speed estimates . . 108

6.8 Spectrogram of the output error during the spin up and down. 109

6.9 The frequency estimates during spin up and down from both the adaptive algorithm and from the encoder/injection reference. Zoomed in plot for the crossover region is also shown. 110

6.10 Time domain of the output of each of the four axis for the three controllers. The adaptive estimation performs just as well as encoder speed estimates . . 111

6.11 Spectrogram of the output error during the spin up and down. The adaptive algorithm has larger error during the crossover region when compared to encoder updates. 112

6.12 The frequency estimates during spin up and down from both the adaptive algorithm and from the encoder and injection reference. The injected frequency is twice that of the spin frequency 113

6.13 Time domain of the output of each of the four axis for the three control. The adaptive estimation performs just as well as encoder speed estimates 114

6.14 Spectrogram of the output error during the spin up and down. 115

6.15 The frequency estimates during spin up and down from both the adaptive algorithm and from the encoder and injection reference. An opposite chirp was injected, making sure they cross at some point 116

6.16 Time domain of the output of each of the four axis for the three controllers. The adaptive estimation performs just as well as encoder speed estimates . . 117

6.17 Spectrogram of the output error during the spin up and down. The adaptive algorithm has larger error in the crossover region. 118

7.1 Set-up of the unknown disturbance problem 120

7.2 The SISO adaptive disturbance rejection control 121

7.3 The $U(z)$ system of the controller, where the state-feedback portion is embedded in the open-loop observer and the portion due to the future disturbance value are an input to the system 122

7.4 The overall Receding Horizon Adaptive Control consisting of an observer for w and adaptive prediction for the non-causal part 125

7.5 The McWhirter structure of the QR algorithm. The rotations obtained from the regressors are used on the rotated output data and the incoming output to produce the error. 127

7.6 The overall structure of the lattice algorthm giving the forward and backward normalized prediction errors with the taps as the rotated output vector. . . . 127

7.7 the position of one of the axis during spin up to 350 Hz and then back down. The first 5 seconds the rotor is simply levitating. 128

7.8 The effect of the adaptive control during only levitation. 129

7.9 While spinning at 350 Hz the adaptive controller is able to attenuate the position error by 40 dB. 130

7.10 During transient spin-up the adaptive controller is able to reduce the position error by 40 dB. 131

7.11 The position error when broadband disturbance is injected. At 12 and 34 seconds the adaptive controller is turned off. 132

7.12 Power spectrum of the error with and without the adaptive controller during broadband disturbance injection. 133

7.13 Plot of the position error for one of the axis during spin-up with disturbance injection. 134
7.14 Spectrogram of the position during spin up with broadband disturbance injection. 134
7.15 maximum singular value of the receding horizon delayed inverse error. 135
7.16 The H^∞ adaptive control diagram. 136
7.17 The typical internal model controller. 136
7.18 The H^∞ problem setup. 137
7.19 The adaptive controller stead-state error while spinning at 350 Hz. 138
7.20 Spectrogram of the position error during spin-up. 139
7.21 Power Spectrum of the position error with the broadband output disturbance injected. 140
7.22 Delayed inversion matching error for both the aggressive and robust inversion. 141
7.23 Robustness criteria for an aggressive high performance inversion and a robust inversion. 142
7.24 The gain of both the aggressive and robust inversion. 142

8.1 Schematic of the Boost Rectifier 144
8.2 Comparator for the PWM 145
8.3 Bode Plot of Boost Rectifier with .3 Duty 147
8.4 Bode Plot of Boost Rectifier with .5 Duty 148
8.5 Diagram of the Single Phase DQ Transformation for the Boost Rectifier . . . 149
8.6 Block Diagram of the Plug-in Repetitive Control 151
8.7 Block Diagram of the Plug-in Resonator 155
8.8 Outer PI Loop for Voltage Control 156
8.9 Duty Cycle for the Three Controllers 158

8.10 Current in the DQ Coordinates for PI and Add-on Repetitive 159

8.11 Output Voltage for the Three Controllers 160

8.12 Harmonic Content for the Three Controllers 161

List of Tables

3.1 RMS error for repetitive controller when (1)just levitating, (2) only tracking,(3) only spinning, and (4)both spin and track. All units are μm. 52

3.2 RMS error for LQGi controller when (1)just levitating, (2) only tracking,(3) only spinning, and (4)both spin and track. All units are μm. 53

6.1 RMS error for single frequency adaptive during spin up and down with (1)just LQGi, (2) Updating using encoder,(3) updating using adaptive estimation. All units are μm. 109

6.2 RMS error for 2 frequency disturbance with one constant adaptive during spin up and down with (1)just LQGi, (2) Updating using encoder,(3) updating using adaptive estimation. All units are μm. 112

6.3 RMS error for 2 frequency during spin up and down with the other at twice the spin frequency for (1)just LQGi, (2) Updating using encoder,(3) updating using adaptive estimation. All units are μm. 114

6.4 RMS error for 2 frequency with one constant adaptive during spin with (1)just LQGi, (2) Updating using encoder,(3) updating using adaptive estimation. All units are μm. 118

8.1 Experimental Parameters 157

8.2 THD in DB for the Three Controllers 161

8.3 Phase for the Three Controllers 161

Acknowledgments

I would like to thank Professor Tsao for his guidance and unique style of teaching. I've gotten the opportunity to work on many projects while being in the lab and learning many different things. TC's knowledge about about technical content never ceases to amaze me. Also, I'd like to thank Professor Gibson for the many hours in his office discussing system, control, and many other off topics. I feel like I've learned from the best in the business with these two.

To my colleagues in the Mechatronics and Controls Laboratory at UCLA, of which there are many, my heart-felt appreciation. Herrick Chang, David Luong, Yen-Chi Chang, Kuo-Tai Teng, Ryan Beech, Rashid Yasin, James Simonelli, Niloufar Esfandi, Chris Kang, Grant Cavalier, Chengwei Chen, Matt Gerber, Martin Lee, and Jack LeCheng all made coming to work enjoyable and without any dull moments. Special thanks to Chris from whom I copied the last two sentences from and who always gave me the big picture about grad school. I don't think this thesis would have been nearly as good without James; one of the best all around engineer that I know. I am also grateful to have met Kuo-Tai, aka Clyde, aka Taiger, who really helped me get started and showed me the hardwork it takes to succeed in grad school.

Also I'd like to thank my parents, my brother, and all my family whose been very supportive throughout all these years. I've always loved to escape campus by coming home and hanging out with Randy and DC. They have a way of putting the right things in the right perspective. Finally, I'd like to thank my mom and dad again, they didn't have to support this long endeavour as much as they did but I think I came out a better person.

Vita

2008	B.S. (Mechanical Engineering), UC Berkeley.
2007	Intern at Brechtel Manufacturing. Hayward, Ca
2009–2011	Mechanical Engineer at China Lake Navair.
2013-present	Teaching Assistant at UCLA

Publications

Rai, S., Cavalier, G., Simonelli, J., Tsao, T. C. (2016). MIMO Repetitive Control of an Active Magnetic Bearing Spindle. IFAC-PapersOnLine, 49(21), 192-199.

Rai, S., Yang, S. Y., Tsao, T. C. (2017, May). Wind turbine system identification and individual pitch control. In American Control Conference (ACC), 2017 (pp. 1371-1376). IEEE.

Rai, S., Simonelli, J., Chu, K., Chang, H., Kang, C., Lim, C., ... Tsao, T. C. (2017, May). Mechatronics pedagogy in mechanical engineering capstone design. In American Control Conference (ACC), 2017 (pp. 5343-5348). IEEE.

CHAPTER 1

Introduction

Active magnetic bearings are used in many applications such as molecular pumps, compressors, magnetic levitating vehicles, and flywheels ([BCK09]), to name a few. An active magnetic bearing spindle (AMBS) has also been of interest for its use in high speed machining (HSM) because of its potential benefits of mitigating wears, thermal-mechanical effects, and creating high bandwidth and dynamic stiffness for precision machining [CK07]. However, AMBS is a challenging mechatronic system, as it presents unstable, nonlinear, and coupled-axis MIMO open-loop dynamics that require careful modeling, identification, and control to enable the realization of the potential benefits. This thesis presents the methods and results of real-time control instrumentation, system identification, and digital control we conducted on a commercial grade AMBS for applications in high-speed machining, vibration rejection, and broadband disturbance rejection.

Control approaches to AMBS mainly address establishing stability or compensating unbalanced spindle motion. Compensation can take the form of either minimizing unbalance force transmitted to the housing or minimizing rotor runout [ZS01]. In this thesis, we discuss control methods that can compensate both. First, we discuss a fixed filter internal model approach for geometrical centering as would be encountered in high speed machining application of magnetic bearings and in subsequent chapters discuss both narrow band and broadband adaptive approaches that can accommodate varying disturbance characteristics.

1.1 Geometrical Centering Using Repetitive Control Applied to Cutting

Because precision is valued above vibration suppression in the HSM application, the first part of this thesis will focus exclusively on runout minimization. [FHM93] and [BSW11] use a H_∞ loop shaping approach to design a robust levitating controller. In most control design considerations, the magnetic bearing can be decoupled, so SISO techniques can be used ([NSL15], [KT16]). In [PDA09], a SISO repetitive controller based on the decoupled plant model for an active air bearing system was developed for disturbance rejection. In [NI96], a μ synthesis approach was used to design a controller for a flexible shaft on a magnetic bearing system similar to the one considered in this paper.

For conventional HSM applications, the spindle runout motion must be eliminated to create desirable axis-symmetric surfaces. This requires control that rejects the spindle runout motion, which is synchronous to the spindle rotation. Another special machining application that creates irregularly shaped surfaces, termed non-circular or axis-asymmetric machining, requires precise tracking of specified spindle orbital motion. A specific example motivating our investigation here is boring of non-circular holes for wrist pin holes in internal combustion engine pistons.

Current production engine piston's pin bore profiles have elliptical cross sections and tapered diameters to increase the fatigue limit of the pin bore under cyclic combustion loads ([WT86]). To create this non-circular bore shapes, various fast tool servos have been developed to either rapidly move the cutting tip mounted on the rotating boring bar ([Cse03], [ZZW08]), or to move the non-rotating piston ([Lia13]). AMBS has the potential of performing this task if spindle orbital motion can be controlled precisely to generate tool tip motion for creating the specified non-circular bore. This presents a tracking control problem of a periodic signal whose fundamental frequency is an integer multiple of the spindle speed. Therefore, in chapter 3 a multivariable repetitive controller is designed and used for cutting. In chapter 5, the influence of the cutting the on the overall dynamics of the system is considered and the model is augmented to take this into account. Actual cutting

experimental results are shown to verify the validity of the overall identification and control methodology.

1.2 Inertial Balancing Using Adaptive Feedforward Control

When compensating for mass imbalance, the goal is to have the spindle spin about its inertial axis, which minimizes the force transmitted to the housing and the control effort on the amplifiers. The traditional approach for achieving this is to place a notch filter in the control so the synchronous spin frequency does not enter [KHF95]. The drawback is this approach may perturb the feedback control loop too much and may result in instability especially when the spin frequency is changing. An alternative is to use an adaptive feedforward algorithm, which injects the proper sinusoidal signal to cancel the disturbance in a feedforward manner [SZQ04] [SBL94]. In [HBG96], a combination of the two was used to tackle the balancing problem.

In [MB95] and [GB10], they showed that the adaptive feedforward algorithm is equivalent to an LTI internal model controller, therefore AFC is somewhat of an alternative implementation of LTI sinusoidal internal model controllers. This is a powerful result since it opens up LTI stability, robustness, and performance analysis to the time varying adaptive controller, essentially the learning gain can be analytically chosen. In most control design considerations, the magnetic bearing can be decoupled, so SISO techniques can be used ([NSL15]; however, our test set-up exhibits significant coupling so the multivariable approach is necessary. This thesis extends the traditional AFC to the multivariable case and for the minimization of both the output and control input in a unified manner, as is needed for magnetic bearings. The main results of chapter 3 is the AFC can reduce vibrations to the housing and minimize the control current input.

1.3 Adaptive Internal Model for Varying Narrow Band Rejection

Once again considering the geometrical centering problem, the spin frequency can be varying in some applications. In this case, the fixed filter designs will have poor performance. In chapter 6, an internal model that adapts with the spin frequency is considered. Selective inversion only in the band of the unknown disturbance is used to enhance robustness. Also, an observer is used to obtain an estimate of the disturbance which is used in the adaptive frequency estimation algorithm. Results are shown for both single and double unknown frequencies during spin up of the magnetic bearing. The pure adaptive approach is compared to using the encoder for speed updates and is shown to have similar performance.

1.4 Unknown Disturbance Rejection for Geometrical Centering

Less work has been done considering both broadband and narrow band disturbances in magnetic bearing application. In chapter 7, we consider the problem of rejecting unknown disturbances for the geometrical centering problem which may be able to be applied to HSM. We use a multivariable adaptive inverse control approach, that extends the typical siso formulation of [WW08]. Specifically, both a receding horizon adaptive control and a decoupling adaptive inverse controller is used for the unknown disturbance rejection problem. Furthermore, this type of algorithm is able to reduce the fundamental spin frequency without the need of an encoder while also reducing the broadband components.

1.5 Boost Rectifier

Rectification is concerned with converting AC power into DC. However, often rectification techniques introduce unwanted current harmonics in the utility. It is well known that these harmonics cause voltage distortion, heating, noise, and reduce the capability of the line to provide energy [SSC03]. Thus, it is no surprise that utility companies enforce standards on the levels of harmonics [GCP03]. Because of this fact, there has been plenty of research interest in rectifiers from both a circuit design and control perspective.

Power factor correction uses power transistors to shape the input current in order to achieve unity power factor. By controlling the switching of the transistors, a properly designed power factor scheme can achieve close to unity power factor. In this work, a typical boost rectifier is used to showcase the control algorithm. While it is true that different topology has a great impact on the power factor, the interest in this work is the control algorithm. The goal of the controller is threefold: 1) make the current in phase with the input voltage 2) reduce the harmonics in the input current 3) regulate the output DC voltage.

To meet the aforementioned goals, researchers have studied many different strategies. The typical strategy is a high bandwidth current loop and a low bandwidth voltage loop based on simplified models [WJ97]. Aside from linear controllers, in [MDM08] a sliding mode controller was applied to a linear model obtained from feedback linearization for a single phase active filter. Additionally, in [PRC09] a predictive controller based on a model of the current was used.

A challenging aspect of the rectifier is that it is a nonlinear system, and not amendable to the abundant linear control techniques. Additionally, the point to linearize about is not well defined (the current and voltage are sinusoids). In [SSP03], the linearization points of the AC quantities are chosen to be the RMS value, but this is not the true equilibrium point. In this paper, we expand on [MRA05] and propose to linearize the system in the DQ rotating frame where all the AC quantities become DC variables, so that linear control techniques can be readily applied. Specifically, repetitive control and a selective harmonic repetitive type controller targets harmonics other than the fundamental.

CHAPTER 2

System Description, Identification, and Stabilizing Control for Active Magnetic Bearing

A challenging aspect of magnetic bearings is obtaining a model to facilitate controller design since the system is multivariable and unstable. Therefore closed loop identification techniques must be used and it is well known that closed loop identification introduces correlation between the input and noise that gives biased estimates of the plant parameters [Lju99]. In [GH95] and [GMH97] a frequency domain SISO/MIMO identification was used to overcome this correlation, while [BHW10] used a predictor based supspace identification (PBSID). In [LM96], it was shown if there is a one step delay in the system, a one step predictor with higher orders recursively built from the one step predictor (a high-order ARX) will overcome the correlation issues in closed loop. Recent work in CLid (Closed loop identification) have built upon this; specifically, a high order ARX is used to estimate the Markov parameters and then followed by subspace identification [Jan03]. As noted in [VBL13], these new methods are all high order ARX followed by model reduction. In this dissertation, a HOARX followed by balanced reduction is used to for the mutlivariable closed loop identification. The attractiveness of this identification scheme is that it is simple to implement, works well in both open and closed loop, and is computationally efficient.

In cutting applications, the main concern is the tip dynamics where the cutting force is concentrated. Using an impulse hammer, the tip dynamics is identified by a frequency domain approach and is augmented to the existing magnetic bearing model. As might be expected, the tip dynamics is related to the resonant frequencies and mode shapes of the spindle. In this chapter, the mode shapes and tip dynamics of the magnetic bearing system is also identified. Lastly, a baseline Linear Quadratic Gaussian controller is designed to

stabilize and provide nominal performance for the magnetic bearing system.

2.1 System Description

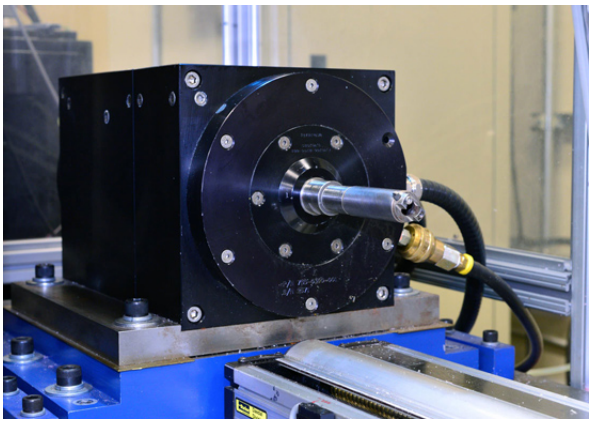

Figure 2.1: Picture of the magnetic bearing system considered in this paper

An industrial grade magnetic bearing (Figure 2.1) for use in high-speed machining application was used as the test bed for this thesis. Figure 2.2 shows the major components of the system. There are two radial magnetic bearing, one in the front and another in the rear, along with a thrust magnetic bearing. The front magnetic bearing is capable of loads up to 1400 N, while the rear is rated for 600 N. There is also an AC induction motor that is capable of spinning the rotor up to 50,000 RPM at 10 kW. The position of the rotor is sensed by eddy current sensors. The coils are energized by 10 amplifiers (one for each electromagnet). The power amplifier is a PWM type that regulates the current into the coils. A block diagram

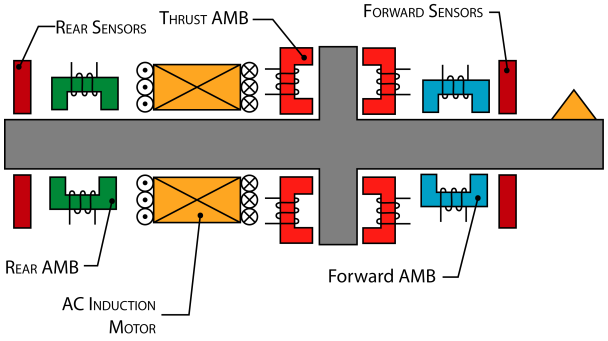

Figure 2.2: Schematic of the magnetic bearing system

of the overall system is shown in Figure 2.3. The Real-Time operating system is using a National Instruments R-series card (NI PCI7852R) for data acquisition and analog output. The card is equipped with an FPGA that can be programmed to read encoders, upsample, and generate sine and cosine signals for the processor. This is useful for alleviating some of the computational demands from the processor. The loop rate was 10 kHz for all system identification and control tasks.

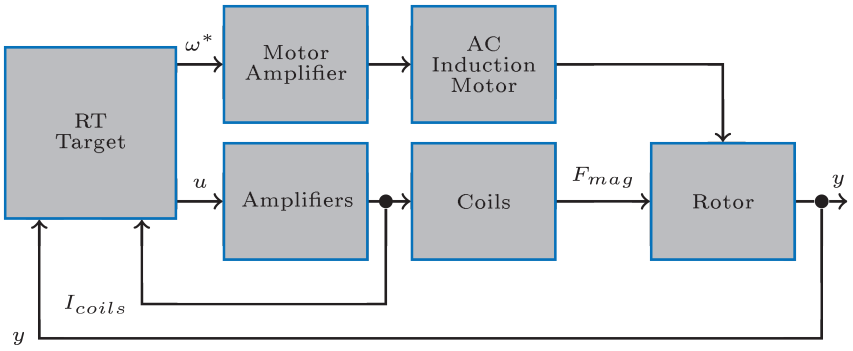

Figure 2.3: Block diagram of the overall system

2.2 Bias Current and Linearization

The system gives full control of the amount of current going into each of the coils, therefore a bias current scheme must be done in software. To see the necessity of bias currents in the coil consider the following simplified 1 DOF equations of motion for a magnetic levitation system

$$m\ddot{y} = k[\frac{(I_b - i)^2}{(y_g - y)^2} - \frac{(I_b + i)^2}{(y_g + y)^2}] \tag{2.1}$$

linearizing this equation about $y_g = 0$

$$\frac{df}{di}|_{y_g=0} = \frac{2I_b}{y_g^2} \tag{2.2}$$

therefore the linearization around the nominal gap with respect to the current is linear when using the bias current. Also,

$$\frac{df}{dy}|_{y_g=0} = 2\frac{I_b^2 + i^2}{y_g^3} \tag{2.3}$$

from this equation, it is seen that the linearization with respect to the position is more linear when the bias current is large. Therefore, using a larger bias current will result in a more linear system.

2.3 System Identification

There are several challenges in the identification the magnetic bearing system. For one, the axes of the sensors are not co-located with those of the actuators, which introduces strong off-diagonal coupling. Also, the electromagnetic force is nonlinear with respect to the coil current and the air gap. As is commonly done, we add bias currents to the opposing coils to render the system more linear. Lastly, the rotor is essentially suspended in the mid-air, so the rotor dynamics are non-linear. But despite these issues, many researchers haver shown that a linear model suffices around a sufficiently small equilibrium point.

In order to begin system identification, the system is assumed to be described by a linear system in its innovation form as in equation 2.18. $\begin{bmatrix} A & B & C \end{bmatrix}$ are the system matrices sought after, L is the kalman gain characterizing the noise, and $e(t)$ is a white noise sequence.

$$\begin{aligned} x(t+1) &= Ax(t) + Le(t) + Bu(t) \\ y(t) &= Cx(t) + e(t) \end{aligned} \tag{2.4}$$

Since the system is open-loop unstable, the identification has to be done in closed-loop. From equation 2.18, if the output is fedback then there exists correlation between the noise and the input which renders biased results [LM96]. Many times the correlation can be ignored and open-loop methods such a N4sid can be used. However, we use high-order ARX methods for identification and found that it performs more consistently than open loop methods since there is significant noise in the system.

2.3.1 High-Order Multivariable ARX Identification

Key in high-order ARX modelling is the one step Kalman predictor. From the innovation form, the one step Kalman predictor is as stated in equation 2.5.

$$\begin{aligned}\hat{x}(t+1) &= [A - LC]\hat{x}(t) + Ly(t) + Bu(t) \\ \hat{y}(t) &= C\hat{x}(t)\end{aligned} \tag{2.5}$$

The impulse response of equation 2.5 is given by equation 2.6

$$\hat{y}(t+1) = \sum_{k=1}^{\infty} C[A - LC]^{k-1}[L\hat{y}(t-k) + B\hat{u}(t-k)] \tag{2.6}$$

The main idea behind high order ARX methods is that the system's markov parameters, $A_k = C[A - LC]^{k-1}L$ and $B_k = C[A - LC]^{k-1}B$, can be estimated as k goes to ∞ using an ARX identification. Given a y and u data sequence, equation 2.7 can be casted as an ordinary least squares problem to estimate that markov parameters using a large N. From [LM96], assuming a delay in the feedback loop, the high order arx model gives non-biased results even in closed loop.

$$y(t) + \sum_{k=1}^{N} A_k y(t-k) = \sum_{k=0}^{N} B_k u(t-k) \tag{2.7}$$

Once the markov parameters (A_k and B_k) are estimated, a model reduction step is usually needed for a low order model suitable for control design. A particulary simple approach is to directly parameterize the high order ARX model into state space observer form as shown in equation 2.8, where $\Gamma = [A_1 A_2 ... A_N]^T$, and then perform a balanced reduction. In [Jan03], the markov parameter estimates are used to perform a subspace identification, where the lower order model is obtained by the SVD. The main idea in both these methods is a high-order ARX followed by model order reduction performs well.

$$\begin{aligned} x(k+1) &= \left[\begin{array}{c|c} & I \\ \Gamma F & \\ & 0^T \end{array}\right] x(k) + \Gamma B u(k) \\ y(k) &= \left[\begin{array}{cc} I & 0^T \end{array}\right] x(k) \end{aligned} \tag{2.8}$$

2.3.2 Non-Parametric Frequency Domain Identification

In order to assess the effectiveness of the identified models, a non-parametric frequency domain identification was conducted and compared to parameterized model. To obtain the frequency response data (FRD), four separate experiments that excited only one input of the closed loop system for frequencies ranging from 10 to 2500 Hz. The reference given was multitone sinusoids in the form of

$$r(t) = \sum_{k=1}^{N} a_k sin(\omega_k t) \tag{2.9}$$

The sinusoids have to be chosen such that they sufficiently excite the system, especially around resonant modes.

The reference, plant input, and plant output were recorded and processed to obtain a matrix of frequency responses. The transfer function from r to u can be built up one at a time using eqn. 2.10

$$\hat{h}^{ur}_{l,m}\left(e^{j\omega}\right) = \frac{\Psi_{u_l r_m}(e^{j\omega})}{\Psi_{u_m}(e^{j\omega})}, \quad l = 1...4, m = 1...4 \tag{2.10}$$

where $\Psi_{u_l r_m}$ is the fourier transform of the cross-correlation of u_l and r_m. Similarly, the transfer function from r to y can be built up as

$$\hat{h}^{yr}_{l,m}\left(e^{j\omega}\right) = \frac{\Psi_{y_l r_m}(e^{j\omega})}{\Psi_{y_m}(e^{j\omega})}, \quad l = 1...4, m = 1...4 \tag{2.11}$$

Once the overall transfer functions were obtained, the open loop unstable frequency response is the point-by-point matrix inversion, as shown in eqn 2.12.

$$\hat{H}^{yu}\left(e^{j\omega_k}\right) = \hat{H}^{yr}\left(e^{j\omega_k}\right)\left(\hat{H}^{ur}\left(e^{j\omega_k}\right)\right)^{-1} \tag{2.12}$$

The frequency response data is used to compare how good the models obtained from the time-domain ARX identification are and to obtain approximate error bounds for robustness analysis. Assuming a multiplicative error, eqn.2.13 is the error, where $H^{yu}(e^{j\omega}$ is the frequency response data used as the truth model and P_{mod} the identified model.

$$E(e^{j\omega_k}) = P^{-1}_{mod}(e^{j\omega_k})(H^{yu}(e^{j\omega_k}) - P_{mod}(e^{j\omega_k})) \tag{2.13}$$

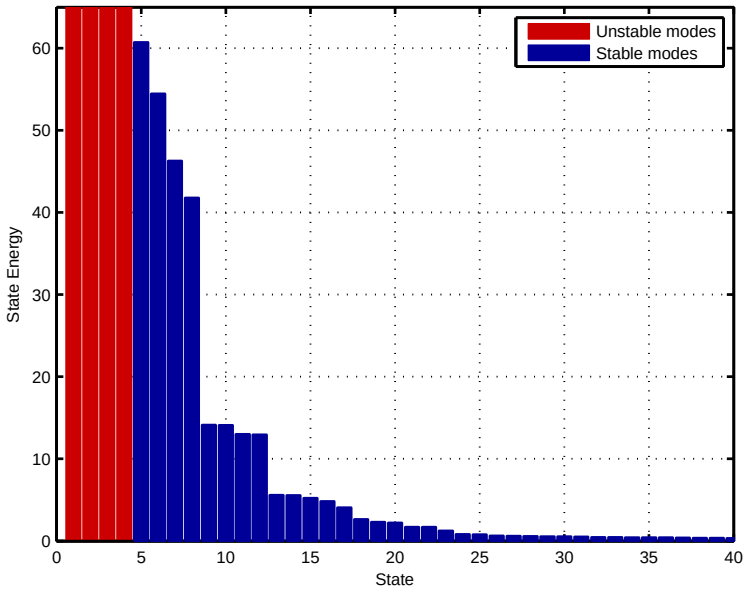

h

Figure 2.4: First 40 Hankel Singular Values of high order state space model

2.3.3 High-Order Results

A time-domain identification using Pseudo-Random Burst Sequence (PRBS) reference input was performed to identify the open loop unstable plant. A high-order ARX least squares was used to find the A and B Markov parameters which are both 4x4 matrices, while both $y(t)$ and $u(t)$ are 4x1 vectors. Figure 2.4, shows the Hankel Singular Values of the high order ARX model which is able to correctly estimate the 4 unstable modes.

Two major considerations when identifying high order models are: first, the order of the high order ARX model and second, the number of data points needed for the least squares problem. Figures 2.5 and 2.6 illustrates the effect of these. The plots show the maximum singular value of the error, eqn 2.13. Larger data length keeps the matrix tall even when identifying many parameters, which is crucial for identification. As suspected, the identification gets worse as the number of data points decrease, for the magnetic bearing system $>$ 4000 points were used for identification. Also, increasing the the order has diminishing return after a 120^{th} order model, but low orders can give incorrect models.

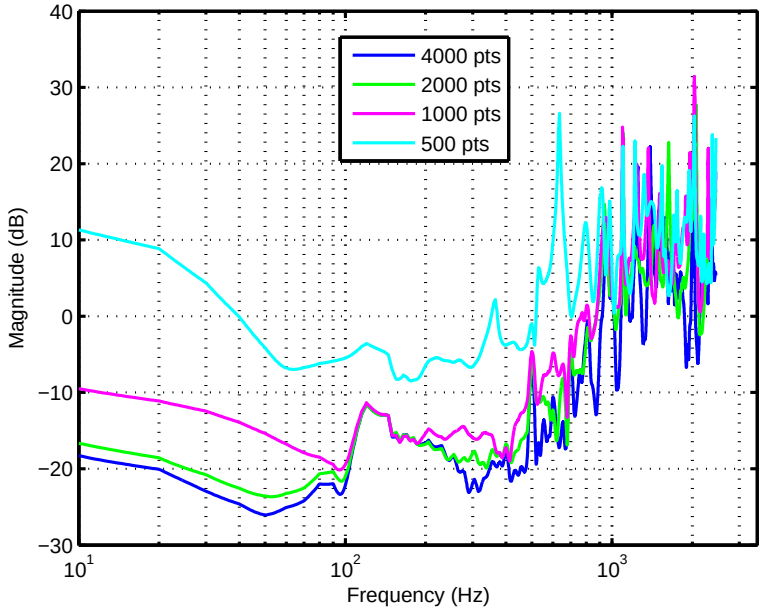

Figure 2.5: The effect of the number of data points chosen for the high order identification. The higher the number of data points, the better the identification.

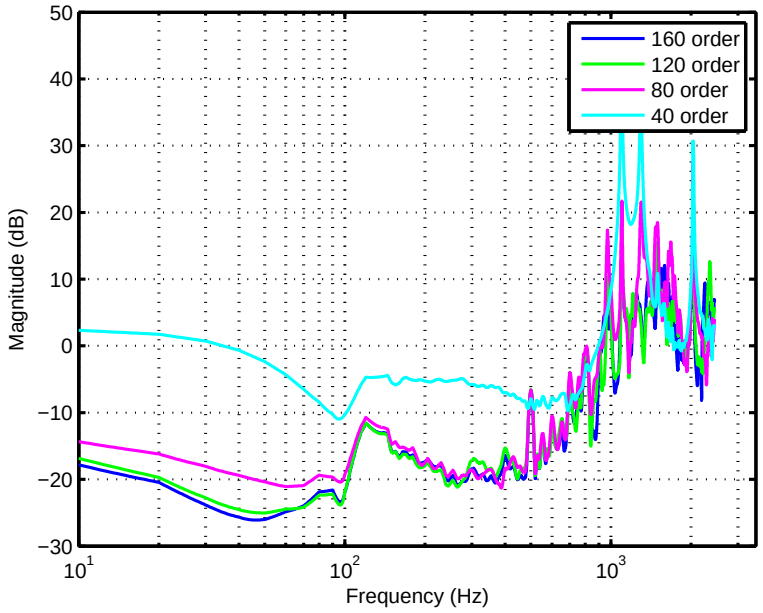

Figure 2.6: The effect of the order chosen for the high order ARX model. The higher the order, the better the identification.

2.3.4 Reduced Order Results

The high-order models obtained in the previous section are not suitable for low order control design. Two different identification schemes were used to determine the low order open-loop plant: 1) a high-order arx followed by balanced reduction 2) Matlab's implementation of the Jansson's SSARX scheme [Jan03].

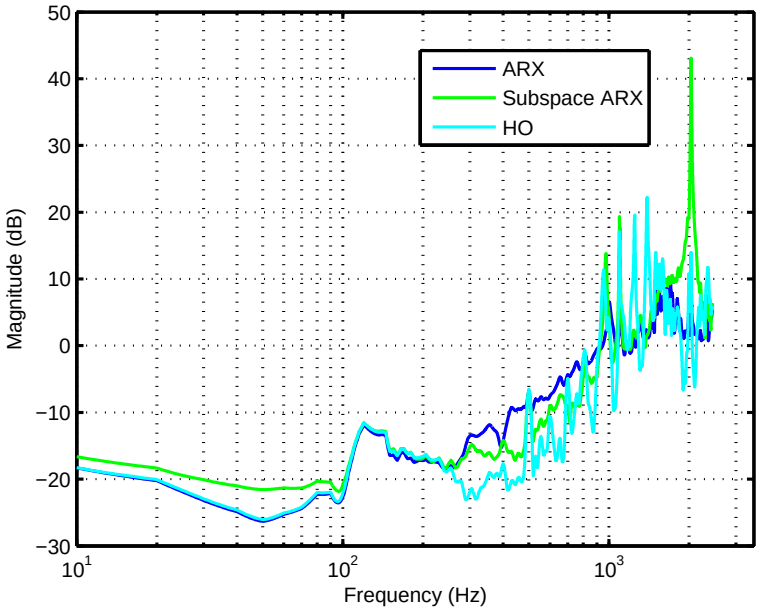

Figure 2.7: Multiplicative error comparison of open loop plant using two different high-order arx techniques and the high order model compared to the frequency response data

Figure 2.7 sums up the results of the identification, which shows the error of both methods and the high order identified model against the frequency response data. Both methods identified a 20^{th} order model while the high order model was the 120^{th} model. Both methods gave useable models for control design, but the ARX followed by balanced truncation was used for design since it has less error at the 2 kHz resonant model. Figure 2.8 shows the error for various reduced order lengths; this was the main consideration in choosing a 20^{th} order model. The primary conclusion drawn from the identification experiments is that it is difficult to obtain an accurate plant model after 1 kHz. Figure 2.9 shows the error bound $W_r(z)$ used for robustness analysis where the actual plant is assumed to be contained in

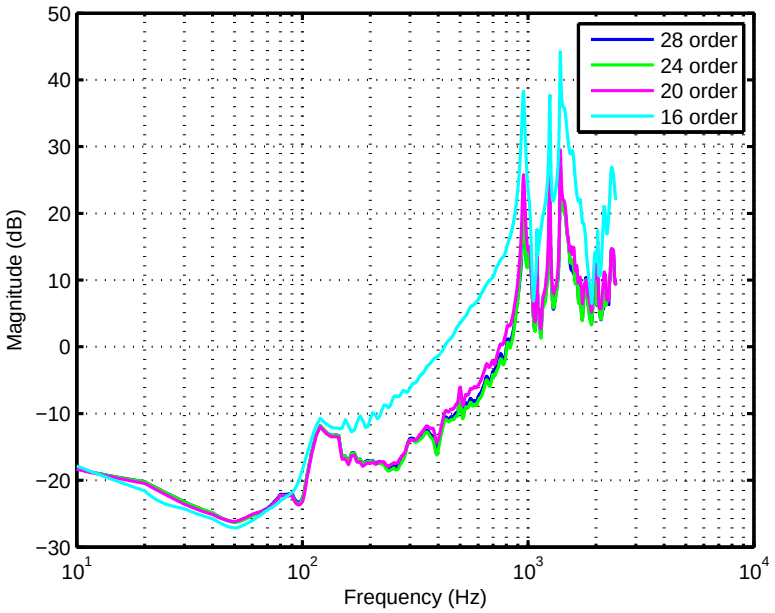

Figure 2.8: Error using low order models, reduced from the high order model

equation 2.14; Δ is a full block 4x4 dynamic uncertainty with a norm less than one. Clearly, $W_r(z)$ is just an approximation of the plant uncertainty used to facilitate analysis and design of controllers while taking an estimation of the plant uncertainty into account.

$$P(z) = P_{nom}(z)(I + W_r(z)\Delta(z)) \tag{2.14}$$

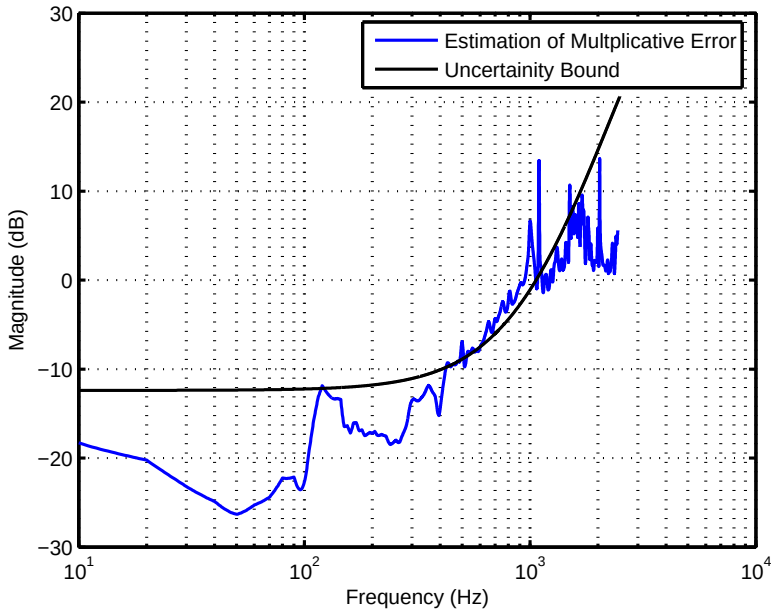

Figure 2.9: Multiplicative error bound used for robustness analysis

2.3.5 Flexible Modes and Frequencies

Viewing the rotor as a flexible structure, the general equations of motion is

$$M\ddot{x} + (C_1 + C_2(\omega))\dot{x} + (K + H(\omega))x = f \tag{2.15}$$

M is the symmetric mass matrix, C_1 is the symmetric damping matrix, K is symmetric stiffening matrix, and C_2 and H are the anti-symmetric matrices depending heavily on the rotor spin frequency. The identification procedure was done with the rotor not spinning, figure 2.10 shows the raw Frequency Response Data (FRD) and the reduced state-space model's maximum singular value. The open loop frequency response show resonant modes of the rotor at 1.1 kHz and 2 kHz, which appear strongly in the cross terms and make a decoupling transformation difficult to obtain. The figure also shows the rigid body modes, which can be visualized by neglecting the flexible modes.

Aside from the natural frequencies, the associated mode shapes are also important. The mode shapes of a system describe the pattern of motion for a vibrating system at the resonant frequencies. A spinning rotor's first mode shape is cylindrical where the rotor is moving up

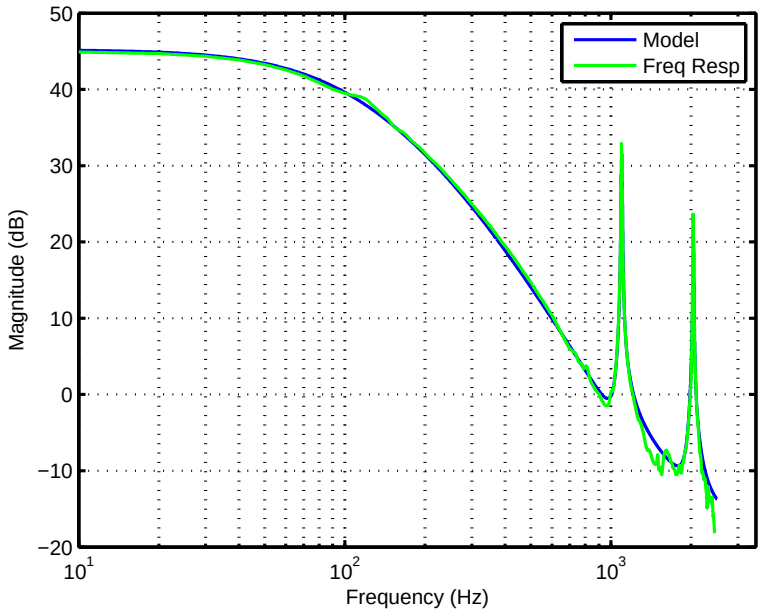

Figure 2.10: Singular values of the open loop plant model and frequency response data highlighting the flexible modes

and down, while the second forms a conical shape. Assuming the modes are lightly damped, the mode shape can be determined by the "Quadrature Peak Picking" method. This method relies on the assumption

$$Real(G(\omega_r) = 0 \tag{2.16}$$

$$\mathbf{e} = peak(Imag(G(\omega_r)) \tag{2.17}$$

The mode shape can be determined by examining the peak of the imaginary part of the frequency response function at the resonant modes. Figure 2.11 shows the imaginary part of the frequency response for the V axis sensor and actuator pair. Noting that the sensor/actuator are not collocated, the peaks indicate the motion at both sensors are out of phase with the motion at the first actuator while being in phase with the motion at the second actuator. This also indicates the node is located in between the first sensor/actuator pair and in front of the second pair (figure 2.12. The increased magnitude of the frequency response at the rear axis compared to the front indicates a node is close to the front sensor.

The first mode vibrations are more observable at the rear sensors than the front.

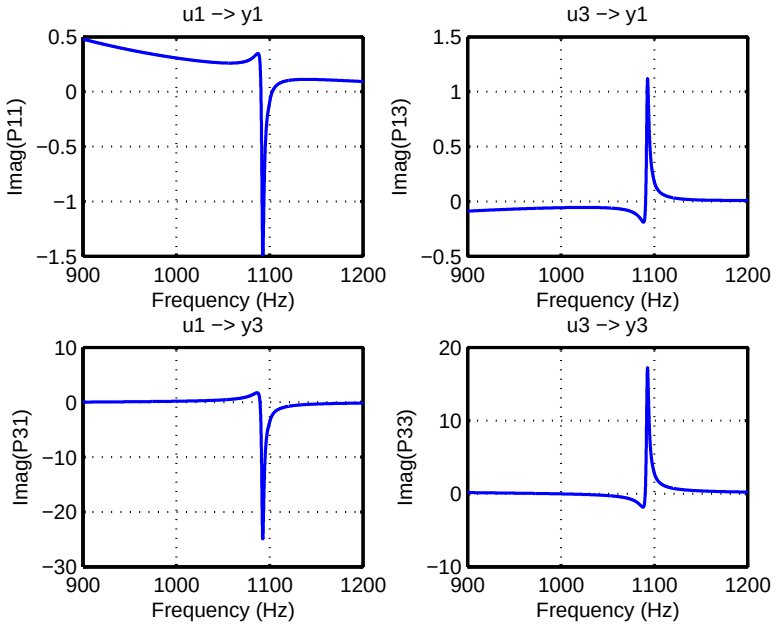

Figure 2.11: The imaginary part of the frequency response at the 1 kHz resonant mode.

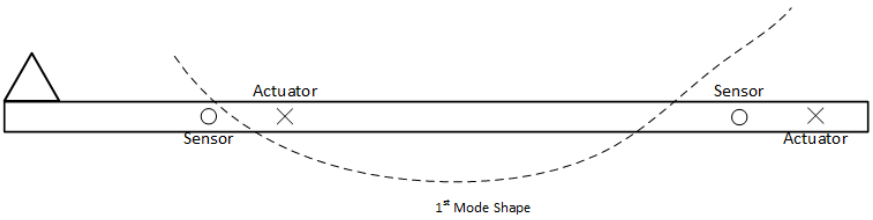

Figure 2.12: Pictorial illustration of the first mode shape.

2.3.6 Gyroscopic Effect

From eqn. 2.15, it is seen that the spin frequency (ω) impacts the natural frequencies of the rotor system. This is termed the "gyroscopic effect", where the natural frequencies split into a forward and backward whirl component. The moment caused by the spinning of the rotor increases the forward whirl frequency while decreasing the backward whirl, termed "gyroscopic stiffening" and "gyroscopic weakening" respectively. In order to identify the effect of the gyroscopic effect, a white noise sequence was fed into reference and the frequency response obtained by the fourier transform of the correlations as detailed in section 2.3.2.

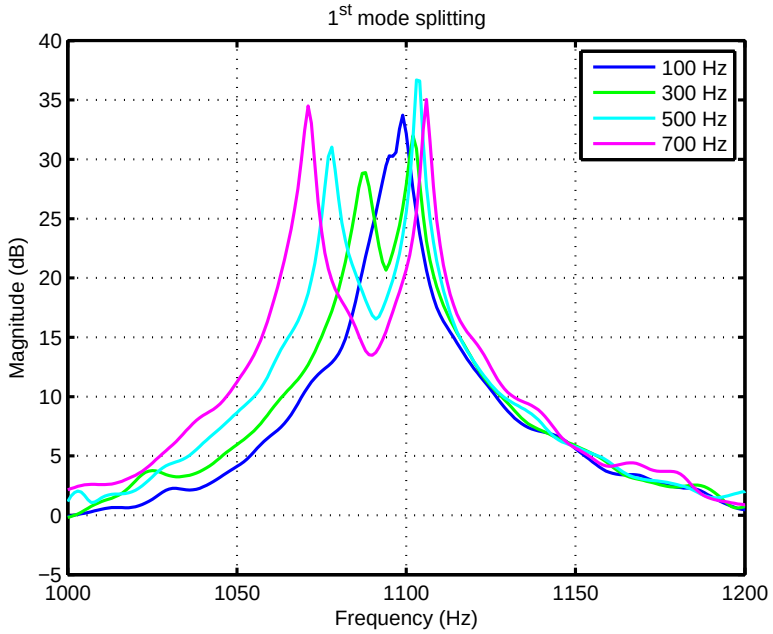

Figure 2.13: Singular Values of the frequency response for different rotor speeds near the 1^{st} natural mode

Figures 2.13 and 2.14 show the singular values of the frequency response of the open loop AMBS for rotor speeds ranging from 100 to 700 Hz around the 1^{st} and 2^{nd} natura modes. They both show a separation of the natural frequency that increases as the rotor speed increases. The first cylindrical mode is less affected by the rotor speed while the second conical mode is more so. Figure 2.15 shows the modal frequencies as the rotor speed increases, which illuminate these insights further. From a control perspective, instability can

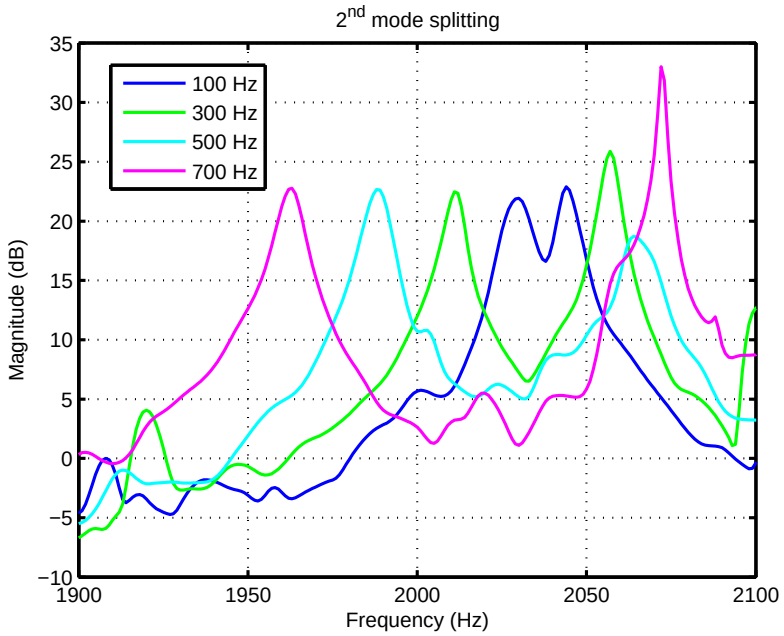

Figure 2.14: Singular Values of the frequency response for different rotor speeds near the 2^{st} natural mode

result if the controller is not robust to these plant variation due to rotor speed changes.

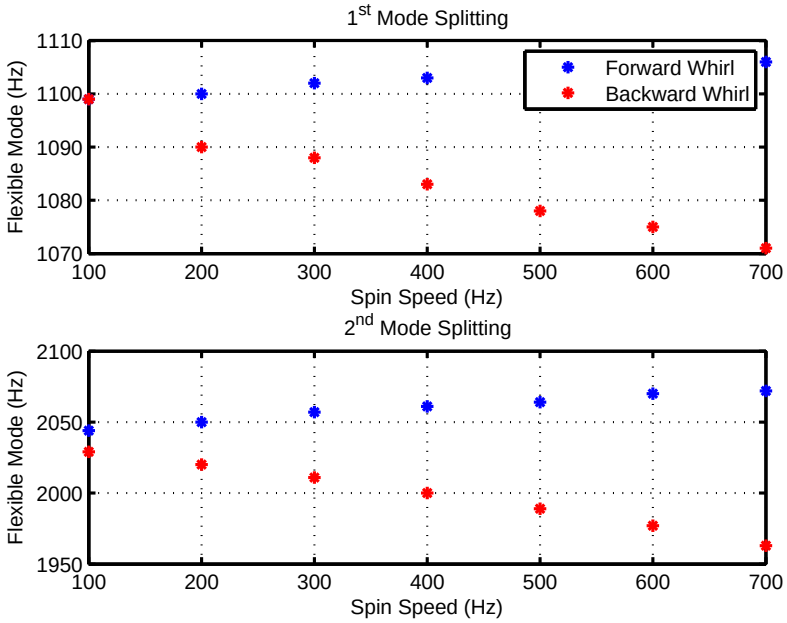

Figure 2.15: The top plot shows the 1^{st} mode splitting as the rotor speed is increased from 100 to 700 Hz, while the bottom shows the 2^{nd} mode.

2.4 Tip Dynamics Identification

For cutting applications, the dynamics of the tip of the rotor is critical. It is a requirement that for a given reference and rotor speed the tip is moving in a known manner. From section 2.3.5, the mode shapes indicate that the tip is more excited at the flexible modes than the sensor indicate, so treating the rotor as a rigid body will not give accurate tip dynamics. During cutting, the cutting forces are concentrated at the tip so a reasonably accurate model of the tip dynamics is necessary.

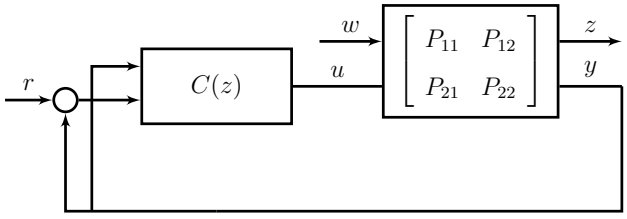

Figure 2.16: Structure for the identification of plant and tip dynamics

Figure 2.16, shows a block diagram of the overall system with the cutting dynamics

included. The main assumption is that the cutting dynamics can be represented as an additional input and output to the linear model. This assumption implies the tip motion is the sum of the modes of the rotor. The expanded system can be described as

$$\begin{aligned} x(t+1) &= Ax(t) + Bu(t) + B_w w(t) \\ y(t) &= Cx(t) \\ z(t) &= C_w x(t) \end{aligned} \tag{2.18}$$

So the identification goal is to find the input and output matrices. The challenging part of the identification is the tip is difficult to excite in a known fashion while exciting the reference as well. Also, the identification must be done in closed loop so setting the plant input (u) to zero and then injecting a disturbance (w) is not possible. Given these considerations, the identification is done in two steps:

1. The $\begin{bmatrix} A & B & C \end{bmatrix}$ of the AMBS are identified as a 4 input and 4 output multivariable system as done previously using time domain methods.

2. The B_w and C_w due to the tip force and displacement are then identified using the given system matrices by a least squares fit using the frequency response obtained by striking the tip with an impulse hammer. These are two input and two output matrices.

The following sections describe the procedure, culminating in an expanded model of the system that includes the tip dynamics.

2.4.1 Experimental Set-up for Tip Dynamics Identification

Figure 2.17 shows the major components for the rotor tip analysis. A special fixture was manufactured to mount two external Kaman eddy current displacement sensors— one for each axis. Although not shown, the eddy current sensors was calibrated using a Sony Magnescale probe with 1 μm of resolution. A PCB Piezotronics 086C03 impulse hammer capable of impulsive forces up to 500 lbs was used to inject a force at the tip.

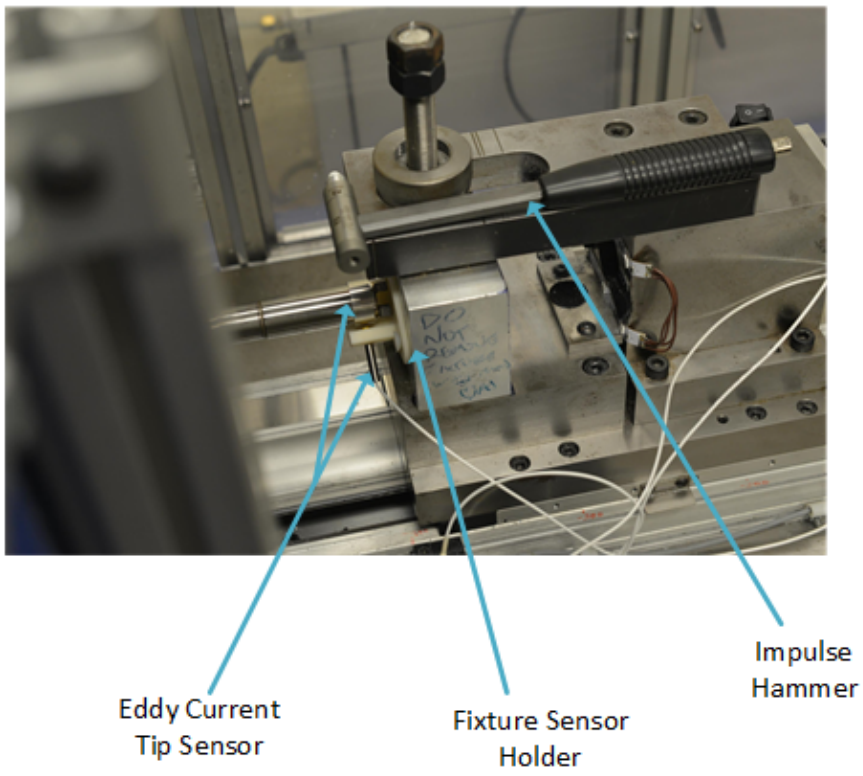

Figure 2.17: Picture of the eddy current and impulse hammer set up at the tip.

2.4.2 Static Calibration

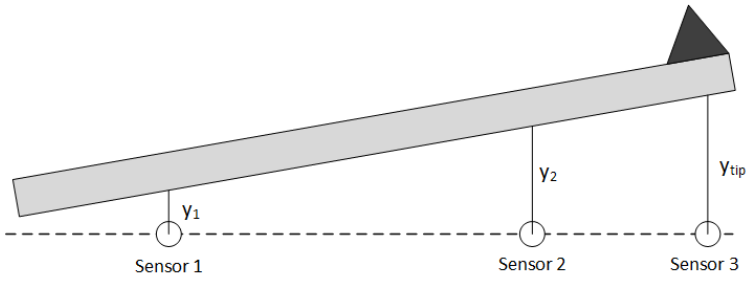

Figure 2.18: Simple Kinematics for the static calibration tests.

Figure 2.18 shows a simple kinematics diagram of the rotor useful for static calibration. The goal of the static calibration is to relate the feedback sensors measurements to the actual tip displacement. This allows us to be confident the tip is actually moving as expected when injecting a reference to the feedback sensors. Exploiting similar triangles, the following

expression for the tip position can be obtained

$$y_{tip} = a(y_1 - y_2) + by_1 \tag{2.19}$$

where a and b are parameters that depend on the distance between the sensors. However, this is unknown so the calibration will experimentally find these parameters. The first parameter represents the rotation of the rotor, while the second is the translation component. By evaluating the tip position at various different y_1 and y_2 positions, a least squares fit can be done to obtain the unknown parameters. Figure 2.19 shows the fit for one axis (the other

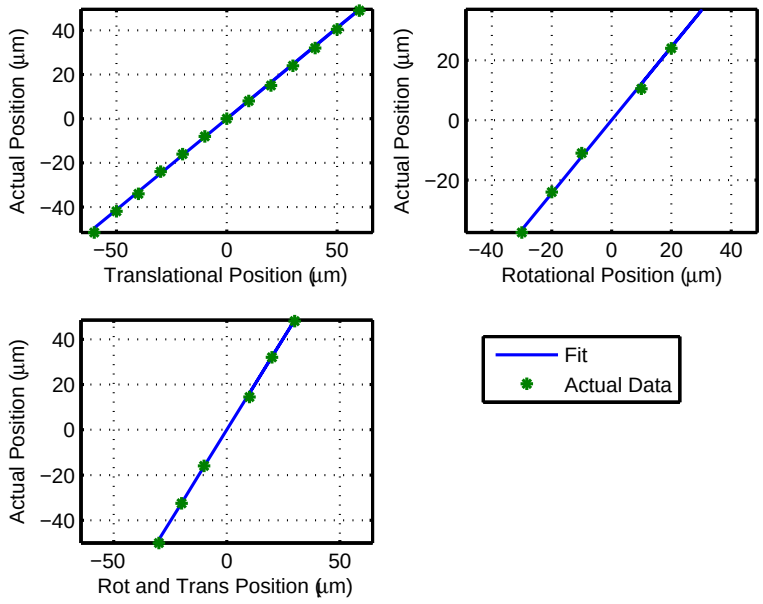

Figure 2.19: Calibration results of the static test, showing both the fitted parameters and the experimental results when in translation and rotation.

is almost identical). The figure in the leftmost top is purely translational with both y_1 and y_2 moving the exact same, which amounts to only identifying the "b" parameter in eqn. 2.19. The rightmost top figure is with $y_1 = 0$ and only y_2 moving, which amounts to only identifying the "a" parameter. The last figure is with $y_1 = -y_2$ to test the accuracy of both parameters.

2.4.3 Impulse Hammer Identification

Using the impulse hammer and tip position sensors, the unknown input and output matrices B_w and C_w can be identified after first identifying the system matrices $\begin{bmatrix} A & B & C \end{bmatrix}$. From figure 2.16, the following expressions can be obtained for the outputs z and y

$$\begin{aligned} y &= S(z)P_{21}(z)w + S(z)P_{22}(z)C_2(z)r \\ z &= (P_{11}(z) + P_{12}(z)[C_1(z) - C_2(z)]S(z)P_{21}(z))w + (P_{12}(z)[C_2(z) + S(z)P_{22}(z)C_2(z)])r \end{aligned} \tag{2.20}$$

Where

$$S(z) = (I + P_{22}(z)[C_2(z) - C_1(z)])^{-1} \tag{2.21}$$

is the sensitivity and is given since it is a function of the plant parameters identified from the original experiment and the controller. Also, since the reference is 0 when the impulse hammer is striking the tip, the part due to the reference can be ignored. Then, by noting that $P_{21}(z) = C(zI - A)^{-1}B_w$, equation 2.20 can be expanded at each frequency as

$$\begin{bmatrix} \hat{G}_{yw}(e^{j\omega_1}) \\ . \\ . \\ . \\ \hat{G}_{yw}(e^{j\omega_N}) \end{bmatrix} = \begin{bmatrix} S(e^{j\omega_1})C(e^{j\omega_1}I - A)^{-1} \\ . \\ . \\ . \\ S(e^{j\omega_N})C(e^{j\omega_N}I - A)^{-1} \end{bmatrix} B_w \tag{2.22}$$

$\hat{G}_{yw}$ is the estimated transfer function using the impulse hammer as the input and feedback sensors as the output (Section 2.3.2). This is a least squares problem, $G = HB_w$, with the frequency axis gridded that has a real solution

$$\hat{B}_w = Re(H^*H)^{-1}Re(H^*G) \tag{2.23}$$

once B_w is estimated, then $P_{21}(z)$ is fully defined. Similarly, equation 2.20 can be expanded as

$$\begin{bmatrix} \hat{G}_{zw}(e^{j\omega_1})^T \\ . \\ . \\ . \\ \hat{G}_{zw}(e^{j\omega_N})^T \end{bmatrix} = \begin{bmatrix} B_w^T(e^{j\omega_1}I - A)^{-1} + P_{21}(e^{j\omega_1})S(e^{j\omega_1})(C_1 - C_2)(e^{j\omega_1})B^T(e^{j\omega_1}I - A)^{-1} \\ . \\ . \\ . \\ B_w^T(e^{j\omega_N}I - A)^{-1} + P_{21}(e^{j\omega_N})S(e^{j\omega_N})(C_1 - C_2)(e^{j\omega_N})B^T(e^{j\omega_N}I - A)^{-1} \end{bmatrix} C_w^T \tag{2.24}$$

which can be solved similarly for the output matrix C_w.

2.4.3.1 Tip Identification Results

Figure 2.20 shows a sample impulse hammer hit. Most notably, the tip motion is excited at the first flexible mode far more than the feedback sensor, which further verifies the mode shape.

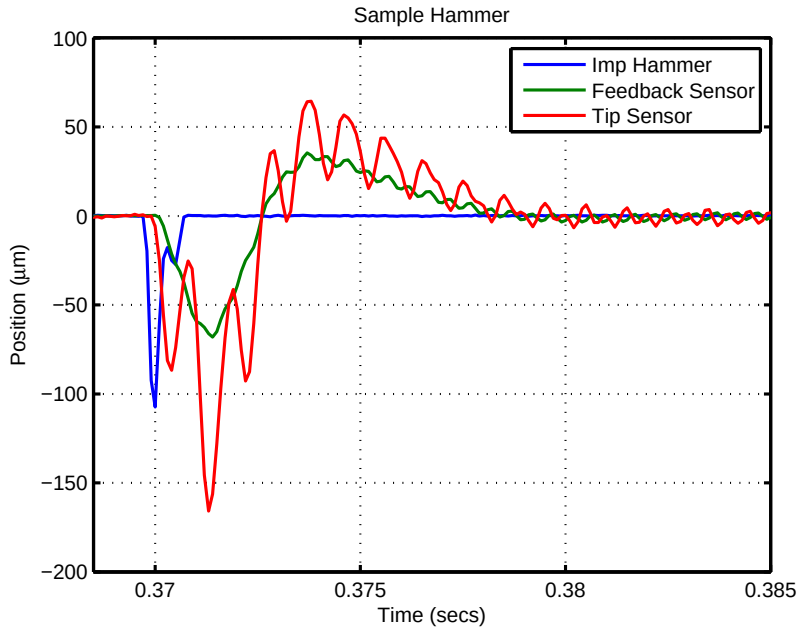

Figure 2.20: Experimental impulse hammer test, showing the hammer impact, feedback sensor, and the tip sensor.

Figures 2.21 and 2.22, show the results of fitting the input B_w matrix. It is important to

note that it was assumed the force on the V axis did not affect the displacement on the W axis and vice versa. Both the magnitude and phase show good agreement out to the useable sensor bandwidth of 2200 Hz.

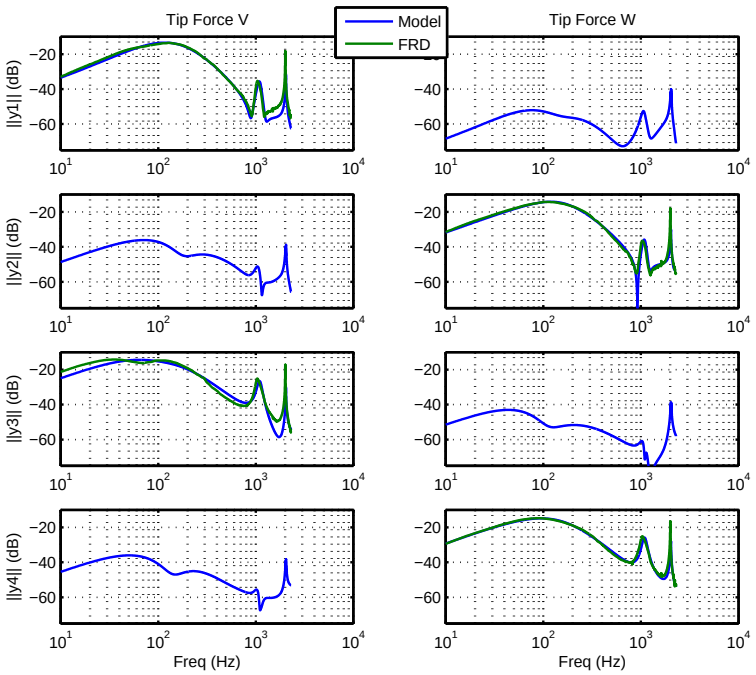

Figure 2.21: The experimental magnitude of the frequency response and identified model from the impact force to feedback sensor output.

Finally, the results of fitting the impulse force to the tip displacement is shown in figures 2.23 and 2.24. The overall identification fits well with the first and second flexible modes being excited as expected.

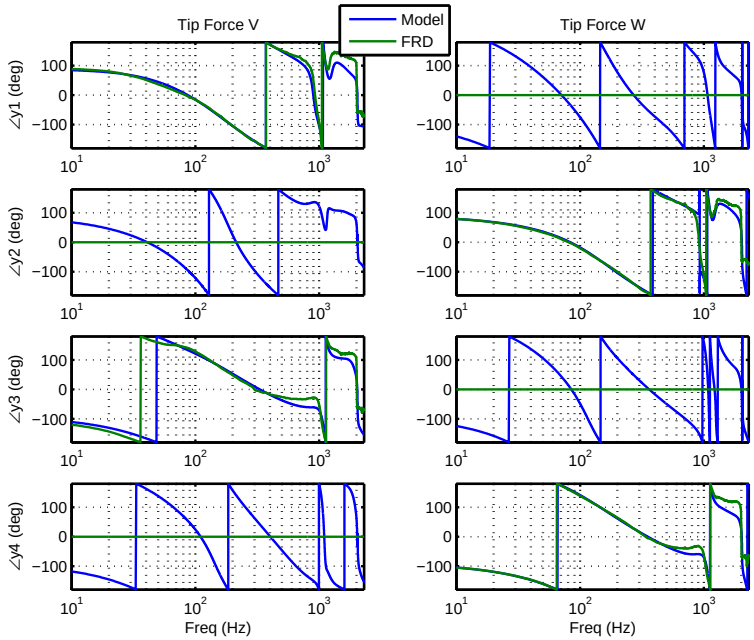

Figure 2.22: The experimental phase of the frequency response and identified model from the impact force to feedback sensor output.

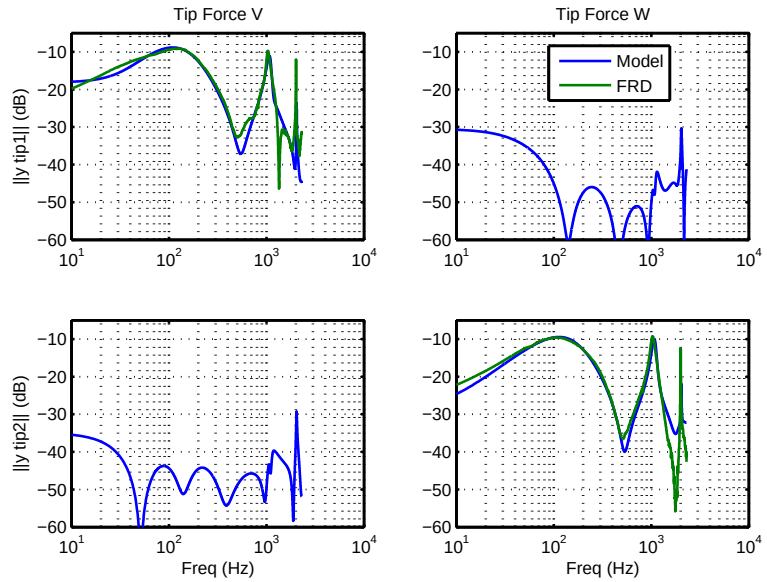

Figure 2.23: The experimental magnitude of the frequency response and identified model from the impact force to tip sensor output.

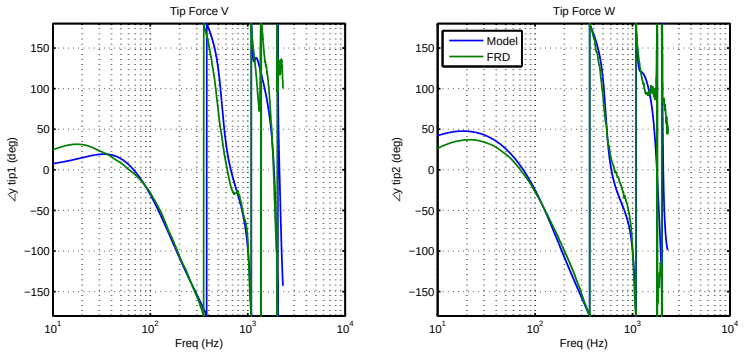

Figure 2.24: The experimental phase of the frequency response and identified model from the impact force to feedback sensor output.

2.5 Frequency Weighted LQGi

2.5.1 Linear Quadratic Control Design

In order to stabilize the open loop plant and attenuate low frequency disturbances, a Linear-Quadratic-Gaussian with Integral action (LQGi) controller that took robustness into consideration was designed. The main design considerations for the LQGi controller were bandwidth, saturation, and stiffness. Obviously, higher inner loop bandwidth is desired, but comes at a cost of saturation and robustness.

LQGi control is well known, but the design process is briefly summarized here for completeness. Given a plant as in Equation 2.25,

$$P(z) = \left[\begin{array}{c|c} A_p & B_p \\ \hline C_p & 0 \end{array}\right] \tag{2.25}$$

For constant tracking, such as levitation the plant needs to include an integrator

$$z_{k+1} = Iz_k + r_k - y_k \tag{2.26}$$

To weight the control action at different frequencies, the control input is filtered through a user defined system

$$\begin{aligned} w_{k+1} &= A_w w_k + B_w u_k \\ u'_k &= C_w w_k + D_w u_k \end{aligned} \tag{2.27}$$

The overall augmented system is given by

$$\begin{bmatrix} x_{k+1} \\ z_{k+1} \\ w_{k+1} \end{bmatrix} = \begin{bmatrix} A_p & 0 & 0 \\ -C_p & I & 0 \\ 0 & 0 & A_w \end{bmatrix} \begin{bmatrix} x_k \\ z_k \\ w_k \end{bmatrix} + \begin{bmatrix} B_p \\ 0 \\ B_w \end{bmatrix} u_k \tag{2.28}$$

The cost to minimize is

$$J = \begin{bmatrix} x_k^T & z_k^T & w_k^T \end{bmatrix} \begin{bmatrix} Q_p & 0 & 0 \\ 0 & Q_i & 0 \\ 0 & 0 & 0 \end{bmatrix} \begin{bmatrix} x_k \\ z_k \\ w_k \end{bmatrix} + u_k'^T R_w u'_k \tag{2.29}$$

u' is the filtered state used to shape the frequency response. Substituting equation 2.27 for the weight into the cost, the problem is then a standard LQR one with crossterms, provided D_w is not zero.

$$J = \begin{bmatrix} x_k^T & z_k^T & w_k^T \end{bmatrix} \begin{bmatrix} Q_p & 0 & 0 \\ 0 & Q_i & 0 \\ 0 & 0 & C_w^T R_w C_w \end{bmatrix} \begin{bmatrix} x_k \\ z_k \\ w_k \end{bmatrix} + w_k^T C_w^T R_w D_w u_k + u_k^T D_w^T R_w D_w u_k \tag{2.30}$$

The solution to this problem is a state feedback controller

$$u_k = -\begin{bmatrix} K_x & K_i & K_w \end{bmatrix} \begin{bmatrix} x_k \\ z_k \\ w_k \end{bmatrix} \tag{2.31}$$

The plant states cannot be measured so an observer is needed

$$\hat{x}_{k+1} = A_p \hat{x}_k + B_p u_k + L(y - C_p \hat{x}_k) \tag{2.32}$$

The overall LQGi controller is given by Eqn 2.33. The optimal controller is 2-dof where the inputs are the plant output and the error,y and $r - y$ respectively.

$$\begin{aligned} \begin{bmatrix} \hat{x}_{k+1} \\ z_{k+1} \\ w_{k+1} \end{bmatrix} &= \begin{bmatrix} A_p - B_p K_x - L C_p & -B_p K_i & -B_p K_w \\ 0 & I & 0 \\ -B_w K_x & -B_w K_i & A_w - B_w K_w \end{bmatrix} \begin{bmatrix} \hat{x}_k \\ z_k \\ w_k \end{bmatrix} \\ &\quad + \begin{bmatrix} L & 0 \\ 0 & I \\ 0 & 0 \end{bmatrix} \begin{bmatrix} y \\ r - y \end{bmatrix} \\ u_k &= -\begin{bmatrix} K_x & K_i & K_w \end{bmatrix} \begin{bmatrix} \hat{x}_k \\ z_k \\ w_k \end{bmatrix} \end{aligned} \tag{2.33}$$

By combining the plant (Eq. 2.25) and the LQGi (Eq. 2.33), the closed loop plant $G(z)$ can be obtained. Notice the overall closed system does not include the observer dynamics,

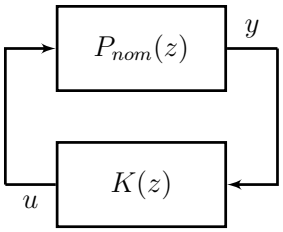

Figure 2.25: Nominal plant model and controller for sensitivity analysis

in that sense the order is minimal, which is helpful in designing a low order $F(z)$ for the plug in repetitive controller.

$$G(z) = \left[\begin{array}{ccc|c} A_p - B_pK_x & -B_pK_i & -B_pK_w & 0 \\ -C_p & I & 0 & I \\ B_wK_x & -B_wK_i & A_w - B_wK_w & 0 \\ \hline C_p & 0 & 0 & 0 \end{array}\right] \tag{2.34}$$

2.5.2 Sensitivity and Robustness of LQGi

By assuming $r = 0$, the LQGi controller (eqn 2.33) can be put into feedback form with the plant as shown in figure 2.25, where $K_{lq} = C_1(z) - C_2(z)$. Then the sensitivity, for performance analysis, is defined as in eqn 2.35. Also robustness can be analyzed by using the multiplicative uncertainty and putting the plant into standard form as in figure 2.26. Then a condition for robust stability is $\bar{\sigma}(T(z)) < 1$, where $T(z)$ is given in equation 2.36.

$$S(z) = (I + P(z)K_{lq}(z))^{-1} \tag{2.35}$$

$$T(z) = lft(\left[\begin{array}{cc} 0 & I \\ P(z)W_r(z) & P(z) \end{array}\right], K_{lq}(z)) \tag{2.36}$$

Figure 2.27 shows the weighting transfer function used to shape the sensitivity. A high pass weighting decreased control activity in the higher frequency region while a peak filter at the second resonant attenuated control activity near the second resonant mode.

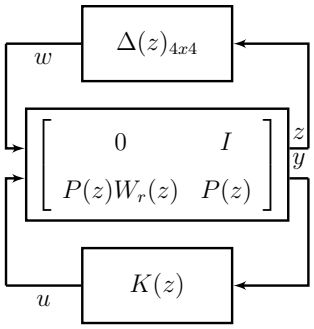

Figure 2.26: Uncertain plant model and controller for robustness analysis

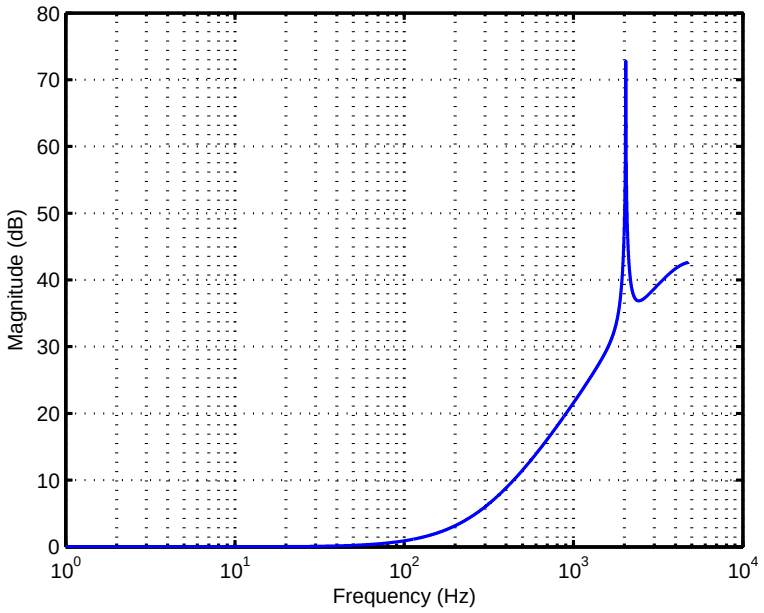

Figure 2.27: High-pass weighting transfer on the input used to increase robustness. The weighting is a broad-band high pass and a narrow band peak filter at the second resonant mode

Figure 2.28 and 2.29 summarizes the results of the inner-loop control design. From the sensitivity plot, the LQGi controller has a bandwidth of approximately 50 Hz, given actuator constraints, this was the highest comfortable bandwidth for a broadband controller, and is well within the first resonant mode. The frequency weighting does not affect the sensitivity too much. The frequency weighted LQGi is robust to the error bound, while the non-weighted severely violates the bounds after the second resonant mode.

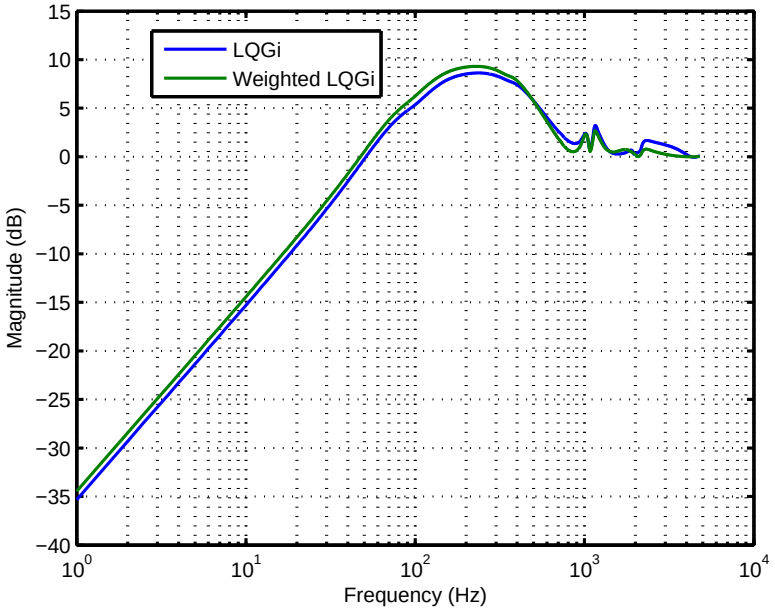

Figure 2.28: Sensitivity of the LQGi feedback controller. The frequency weighting does not affect the performance too much

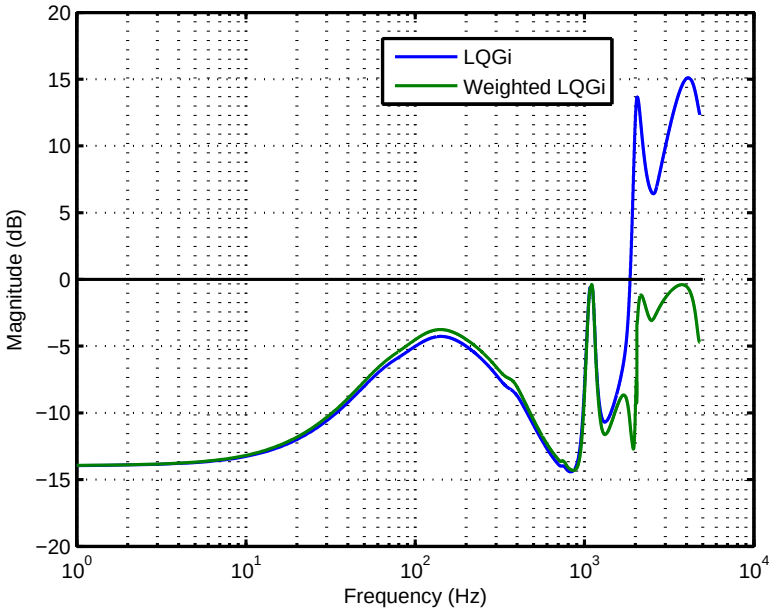

Figure 2.29: Robustness of the LQGi feedback controller. Adding frequency weighting attenuates high frequency control action that increases robustness

Lastly figure 2.30 shows good agreement between simulation and experimental results.

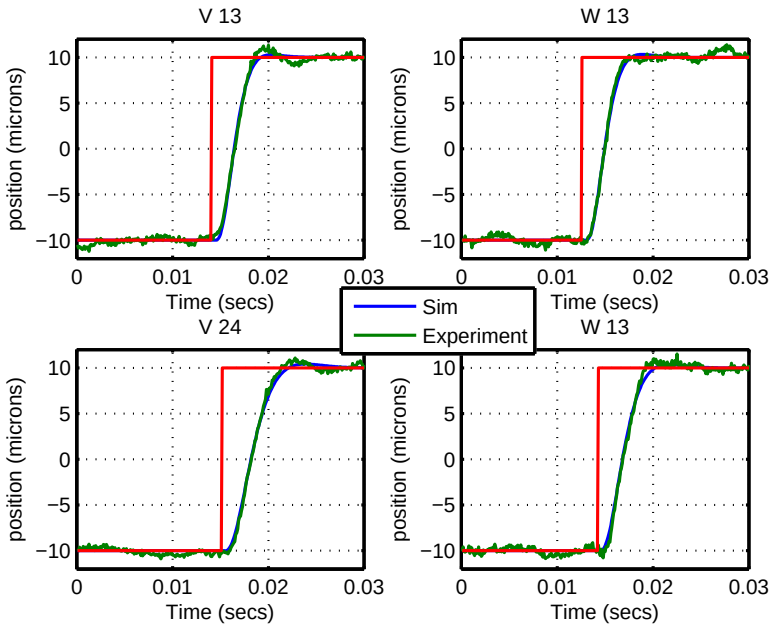

Figure 2.30: Step Responses of LQGi Controller, Experiment and Simulation.

CHAPTER 3

Orbital Motion Tracking

In order to machine circles and ovals, the control system must be able to track sinusoidal references in the high speed machining region. To achieve that goal, we propose high-gain feedback control— specifically a multivariable Repetitive Control. Repetitive control is based on the internal model principle of [FW76a] that states that to achieve zero tracking error, a model of the reference/disturbance must be contained in the controller. Repetitive control places an internal model at a fundamental frequency and its harmonics. Traditional repetitive control methods ([TTC89a], [CDX04]) are SISO formulations, therefore it is not clear how to easily extend these methods to the multivariable setting. In [KLT04], μ-synthesis is used to design a repetitive controller and can be extended to the multivariable setting, but it is highly sensitive to the weighting parameters. In [Lon10a], a FIR interpolation method is discussed; this method extends naturally to the MIMO setting, but cannot claim optimality and may result in long FIR filters. In this thesis, a multivariable repetitive control is designed by solving the model matching problem using γ iteration, avoiding DK iterations. Also, modifications to the repetitive control internal model is used to increase performance and target non-integer frequencies such as 60 Hz electrical noise.

3.1 Repetitive Control Design

The plug-in repetitive control structure shown in figure 3.1 is considered. The goal of this structure is to add tracking or disturbance rejection to an existing controller without perturbing the nominal sensitivity too much. If the controller $C(z)$ is placed directly in the error path, then the problem can be formed as μ-synthesis problem [KLT04]. However, this

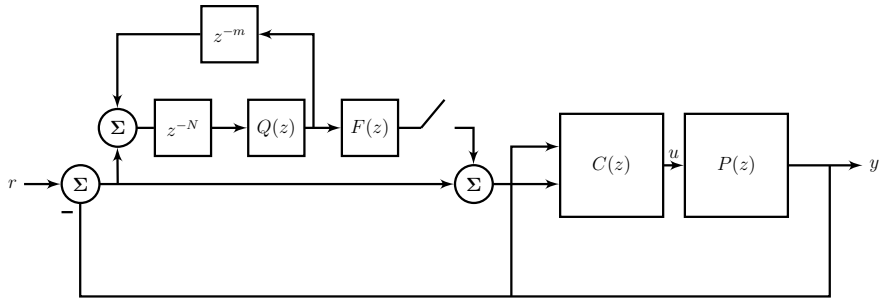

Figure 3.1: Block Diagram of the Plug-in Repetitive Control

approach involves using DK iterations which can be difficult to tune, does not decouple the nominal and plug-in controller, and can result in very high order controllers. To address these issues, we propose a two step design: first a nominal H_2 optimal controller which results in a closed loop system with the same order as the plant and secondly a simple weighted H_∞ model matching problem for add-on control action at the desired frequencies.

The first controller, denoted as $C(z)$ in the diagram 3.1, is designed using an optimal frequency weighted LQGi controller. The main purpose the controller serves is to stabilize the magnetic bearing system. The other major consideration is to attenuate low frequency disturbances, so it should be tuned for broadband performance. Also, the controller should be robust especially in the high frequency region. Lastly, for implementation purposes, the order should not be very high.

The second controller, denoted as $F(z)$, is designed using an optimal H_∞ model matching approach solved using γ iterations. The primary objective is stabilize the add-on repetitive controller given the nominal controller. The controller should properly attenuate disturbances at the desired frequencies, while being robust to plant uncertainty.

When the switch in Figure 3.1 is closed, the repetitive controller is added on to the existing LQGi control. Similar to single variable case, the main objective is to produce high gain at a desired frequency to track references or reject disturbances and its harmonics. This is accomplished by the internal model generator in Eqn 3.1, where N is the number of samples constituting one period of the desired frequency.

$$D(z) = \frac{1}{z^N - 1} I \tag{3.1}$$

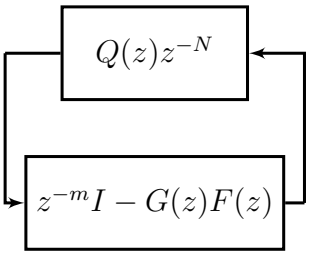

Figure 3.2: Equivalent Block Diagram of the Plug-in Repetitive Control suitable for small gain theorem

In order to design a repetitive controller, filters $F(z)$ and $Q(z)$ need to be determined. The design of these filters is much more difficult when the plant is multivariable; methods such as zero phase error tracking (ZPETC) and zero magnitude inversion are single-variable formulations, and cannot be used. Assuming $r = 0$, the add-on repetitive control can be put into feedback form as shown in figure 3.2; then using the small gain theorem the inequality in Equation 8.11 is a sufficient stability condition.

$$\|(z^{-m}I - F(z)G(z))Q(z)\|_\infty < 1 \tag{3.2}$$

$G(z)$ is the nominal closed-loop transfer function, from reference input to output with the LQGi controller given in equation 2.34. From the stability equation, it is easy to see that the inequality is satisfied when $F(z) = G^{-1}(z)$. However, when the system is non-minimum phase, there will be unstable pole-zero cancellation, so a naive inversion will not work. m is a tuning parameter that depends on how close the non-minimum phase zeros of the system are to the unit circle. From [Tsa94], it is known that the optimal $F(z)$ is such that the optimal cost in Equation 3.5 is an all-pass filter, and that increasing the preview length, m, decreases the error of the model matching problem.

$Q(z)$ (Equation 8.15) is a zero phase low pass filter that limits the bandwidth of the inversion filter, so that high frequency noise will not be amplified and the system is robust

to plant model uncertainty. For the magnetic bearing system under consideration, the Q filter is comprised of four SISO filters (Equation 8.15) in block diagonal form. $Q(z)$ is noncausal, but the preview steps can be emulated. Also, N_q was chosen to be 5 which at 10 KHz is a low pass with a cut off at 800 Hz.

$$q(z) = (.25z + .5 + .25z^{-1})^{N_q} \tag{3.3}$$

Once $q(z)$ is incorporated into the internal model, then

$$D(z) = \frac{z^{-N}q(z)}{1 - z^{-N}q(z)} \tag{3.4}$$

which gives high gain in the passband of $q(z)$ and low gain in the stopband.

3.1.1 $\mathbf{H}_\infty$ minimization

$$\min_{F(z)\in RH_\infty} \left\| \begin{matrix} [z^{-m}I - F(z)G(z)]Q(z)r(t) \\ \alpha u(t) \end{matrix} \right\|_\infty \tag{3.5}$$

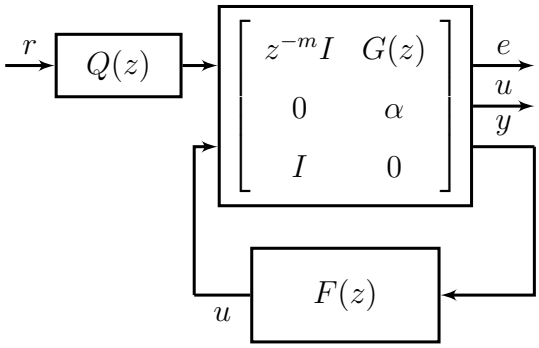

Figure 3.3: γ iterations finds the transfer function to minimize e and obtain an inversion filter for repetitive control

Motivated by the stability condition, the H_∞ problem (Equation 3.5) can be solved for the inversion filter $F(z)$. Figure 3.3 shows the generalized plant in a form suitable for H_∞ solvers. Since there is no uncertainty, H_∞ solvers using γ iterations can minimize equation 3.5. If the transfer function from r to e is less than one then stability of the repetitive control system is guaranteed. $Q(z)$ is determined by the model uncertainty and reduces high gain at high frequency, while m is increased until the stability criterion is met. α in the cost function

limits the magnitude of the controller which leads to a trade off between performance and robustness. The weighting used in this thesis is a simple scalar, but can also be a transfer function to shape the inversion at various frequencies.

3.1.2 Repetitive Control Sensitivity and Robustness

Similar to the LQGi case, the add-on repetitive control from figure 3.1 can be put into feedback form (figure 2.25)when $r = 0$ for sensitivity analysis.

$$S_{rep}(z) = (I + P(z)K_{rep}(z))^{-1} \tag{3.6}$$

After some block diagram manipulation, it can be seen that overall controller is as in equation 3.7.

$$K_{rep}(z) = K_{lq}(z) + C_1(z)F(z)[\frac{z^{-N+m}q(z)}{1 - z^{-N}q}I_{4x4}] \tag{3.7}$$

From which the robustness can be analyzed by the norm of equation 3.8

$$T_{rep}(z) = lft(\begin{bmatrix} 0 & I \\ P(z)W_r(z) & P(z) \end{bmatrix}, K_{rep}(z)) \tag{3.8}$$

Figure 3.4 shows maximum singular value of T_{rep} for the γ iteration inversion filter with $Q(z)$ weighting filter and the input weighted at various levels. The best robustness expected is that of the LQGi controller with the add-on repetitive turned off ($F(z) = 0$), so it is also shown for comparison. The effect of the weighting is easily seen, as α is weighted more a less robust controller is obtained; while a lower weighting will limit the add-on and the robustness approaches that LQGi controller.

Figure 3.5 shows the maximum singular value of the sensitivity, S_rep, which indicates the frequencies that can be tracked or rejected. By adjusting the weighting the α, the sensitivity approaches LQGi only or more aggressive attenuation at the desired frequencies. This plot shows the classical robustness vs performance trade-off as the more aggressive controllers have deeper notches in the sensitivity at the desired frequencies but are less robust to plant model mismatch (figure 3.8.

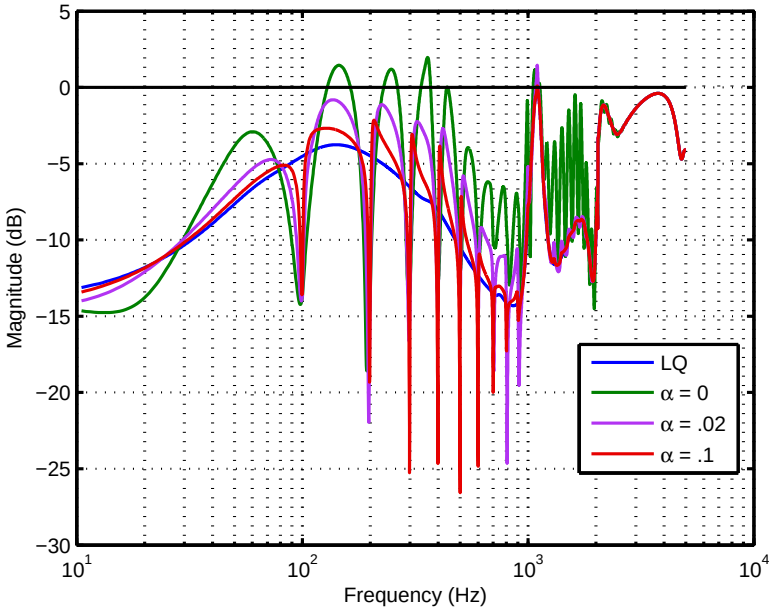

Figure 3.4: Robustness analysis of the repetitive design procedure varying the scalar control input weight

It is also interesting to look at the maximum singular values of the inversion filter itself, since this gives an indication of the frequencies at which control effort can be excessive. From figure 3.6, lower α weighting have much higher gain across all frequencies. On the actual experiment it was seen that high gain caused noisy actuation and excessively excited some frequencies. On the other hand, scaling α too low gives very low actuation across the frequency band and suffers in terms of performance. Therefore, a compromise such that one of the filter in purple was chosen for the inversion filter.

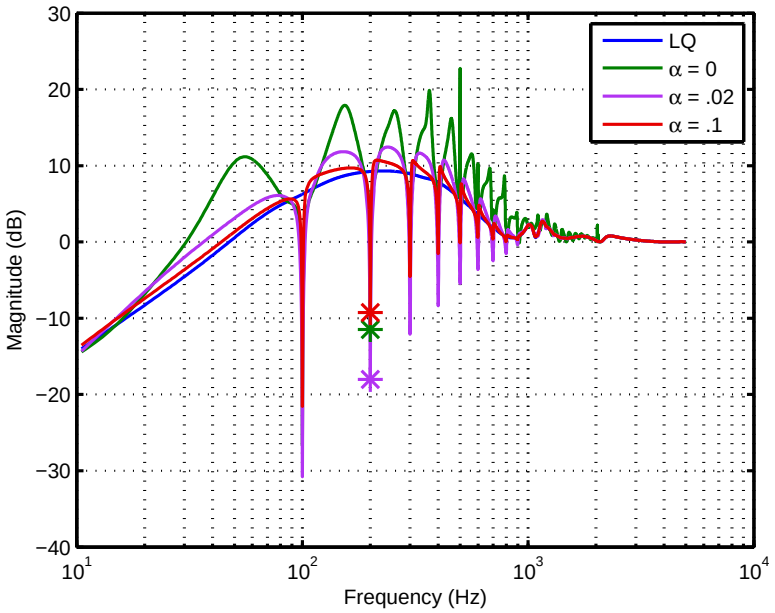

Figure 3.5: Sensitivity/performance analysis of the repetitive design while varying the control input weighting

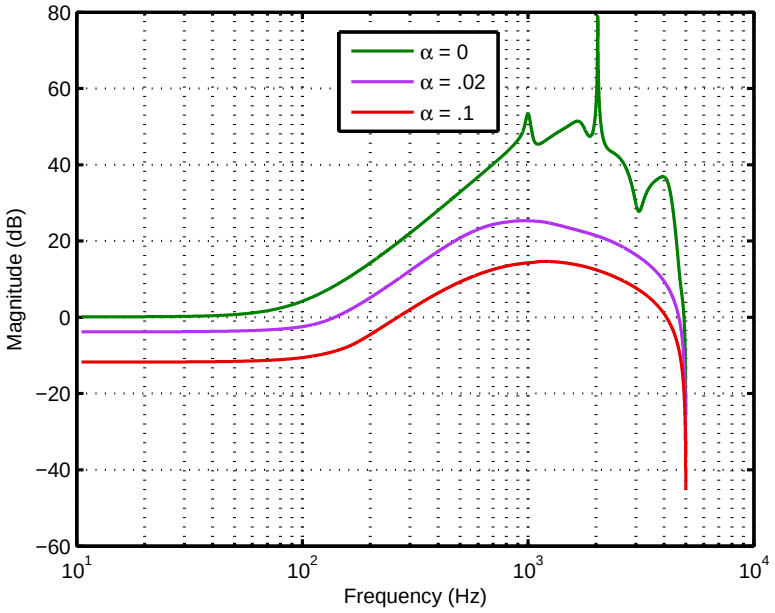

Figure 3.6: Gain of the inversion filter while varying the control input weighting

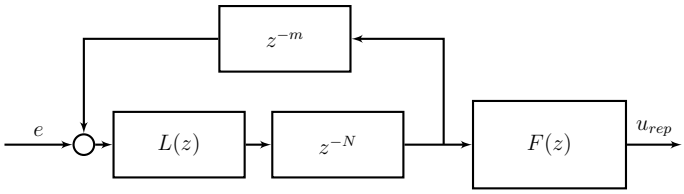

Figure 3.7: Internal model modification with peak filter

3.2 Repetitive Control with Peak Filter

The performance of the classical repetitive control internal model structure can be significantly enhanced by replacing the $q(z)$ filter. From figure 3.7, the transfer function from input to output is

$$D(z) = \frac{z^{-N}L(z)}{1 - z^{-N}L(z)} \tag{3.9}$$

where $L(z)$ is a peak filter 8.18 that picks out discrete frequencies and ideally leaves the others unaltered. The ideal peak filter is given as

$$L(z) = \begin{cases} L = 1 \text{ if } \omega = \omega_{k=1,2,...M} \\ L \approx 0 \text{ if } \omega \neq \omega_k \end{cases} \tag{3.10}$$

If $z^{-N+m}L(z) = 1$ if $\omega = \omega_{k=1,2,...M}$ then $D(z)$ will have infinite gain the desired frequencies and perfect disturbance rejection is achieved.

For repetitive control, the $L(z)$ is usually a low-pass zero phase Q filter. The major issue with using a low pass Q filter is that when rejecting higher frequencies the magnitude is not exactly equal to 0 which effects the quality of the internal model generator. Also for severely non-minimum phase systems, many inversion filters such as zero phase tends to have low gain. A low gain inversion filter coupled with a low quality internal model generator because of the Q filter makes rejecting high frequency disturbances problematic. Therefore, the $L(z)$ filter in the proposed controller is a peak filter that has exactly unity gain at the desired frequency. Since plant and model mismatch is usually at high frequencies, using a $L(z)$ that attenuates these frequencies will make equation 3.11 easier to satisfy.

$$\|(z^{-m}I - F(z)G(z))L(z)\|_\infty < 1 \tag{3.11}$$

A simple way to construct a peak filter is through an all-pass filter as

$$L(z) = \frac{1}{2}(1 - A(z)) \tag{3.12}$$

This corresponds to phase constraints of 0 degrees at the desired frequency and 90 degrees at the bandwidth which also leads to a monotonically decreasing phase that can be realized using a stable all-pass filter.

3.2.1 Peak Filter Sensitivity and Robustness

The sensitivity and robustness of repetitive control with the peak filter modification can be analyzed similarly to the previous section but with the internal model adjusted accordingly. Moreover, the same inversion filter can be used if the passband of $L(z)$ is in the passband of $q(z)$ then

$$\|(z^{-m}I - F(z)G(z))L(z)\|_\infty \leq 1\|(z^{-m}I - F(z)G(z))Q(z)\|_\infty \tag{3.13}$$

The same inversion filter is used for repetitive control and its peak filter modification.

Figure 3.8 shows maximum singular value of the complementary sensitivity function for LQGi, classical repetitive, and its peak filter modification. When compared to the classical repetitive control, the peak filter modification has better robustness properties in the inter harmonics and high frequency region. The level of attenuation in these region depends on the bandwidth of the peak filter design. This highlights another added benefit of using the peak filter modification, namely that bandwidth and roll off of the internal model can be adjusted.

Figure 3.9 shows the maximum singular value of the sensitivity. The classical repetitive controller has nearly 20 dB attenuation at 200 Hz and even less at high frequencies because of the $q(z)$ and inversion filter pair. However, using the peak filter modification with internal models at 100, 200, 300, and 400 Hz the level of attenuation at these frequencies is effectively 0. This highlights the main benefit of the peak filter modification— that it decreases the sensitivity at higher frequencies while improving robustness.

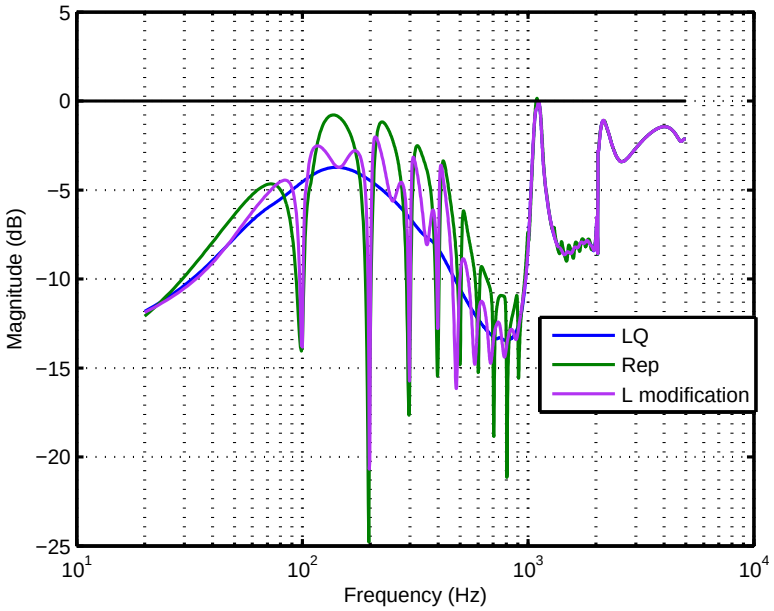

Figure 3.8: Robustness analysis of the repetitive design procedure with the peak filter modification compared against classical repetitive and LQGi

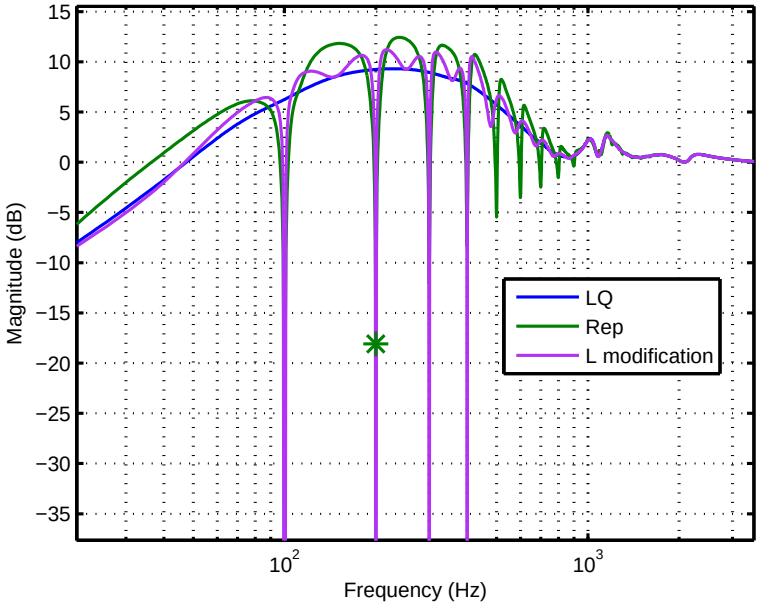

Figure 3.9: Sensitivity/performance analysis of the repetitive design procedure with the peak filter modification compared against classical repetitive and LQGi

3.3 Peak Filter with Phase Compensation

The main drawback of repetitive control with the peak filter modification is that only integer harmonics can be targeted. However, by replacing the large delay with a phase compensation filter, non-integer harmonics can be targeted. For the inversion of non-minimum phase systems, delays must be introduced and the internal model generator must compensate for the added delays. In repetitive control, the internal model generator is z^{-N} and the non-causal operator z^m can be absorbed by z^{-N+m} but this only allows for integer harmonics to be targeted. A useful feature of all-pass filters is that it can be used to add phase advance at specific frequencies. Obviously, a non-causal operator such z^m cannot be implemented in real-time, however at discrete frequencies an all-pass filter that has the correct phase advance can be constructed. The key idea is from equation 3.14

$$\angle z^m = \angle e^{jm\omega} = m\omega \tag{3.14}$$

Then the phase constraints on the desired all pass filter is $\theta_A(\omega_n) = m\omega_n$.

To design the all pass filter, the approach described in [PT97] is used. It can be verified that phase of an all pass filter is given by

$$\theta_A = -2M\omega + 2\arctan(\frac{\sum_{k=1}^{2M} a_k \sin(k\omega)}{1 + \sum_{k=1}^{2M} a_k \cos(k\omega)}) \tag{3.15}$$

given a desired phase response at $2M$ points then equation 8.20 can be cast as linear system as in equation 8.25 where $\beta_i = \theta_A + 2M\omega$ and i ranges from 1 to $2M$.

$$\tan(\beta_i) = \sum_{k=1}^{2M} [\sin(k\omega_i) - \tan(\beta_i)\cos(k\omega)]a_k \tag{3.16}$$

The main benefit of the designing an all-pass using equation 8.25 is the phase can be as desired at specific frequencies, however it is not guaranteed to return a stable system. As

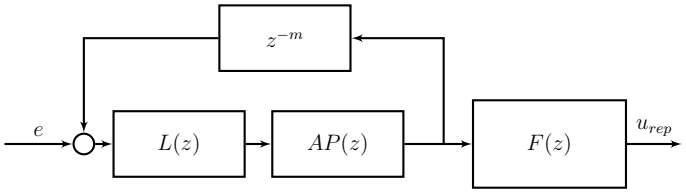

Figure 3.10: Internal model modification with peak filter and phase compensation

long as the desired frequencies is monotonically decreasing, a stable high order all-pass will be generated.

From figure 3.10, the transfer function from input to output is

$$D(z) = \frac{AP(z)L(z)}{1 - z^m AP(z)L(z)} \tag{3.17}$$

where $L(z)$ is a peak filter and $AP(z)$ is an all-pass filter that compensates for the phase z^m at the desired frequencies. If the $AP(z)$ compensates for the phase exactly and $L(z)$ is 1 at the desired frequencies than there will be infinite gain at those frequencies.

3.3.1 Peak Filter with Phase Compensation Sensitivity and Robustness

Since $AP(z)$ has unity gain the stability condition is the same as for the repetitive control with peak filter. Therefore, the same inversion filter can be used and the sensitivity and robustness can be analyzed similar to the classical repetitive control. For controller design on the AMBS, an internal model was placed at 60, 180, 200, 300, and 400 Hz to account for the 60 and 180 Hz noise from the AC lines.

Figure 3.11 shows maximum singular value of the complementary sensitivity function for LQGi, repetitive with peak filter modification, and peak filter with phase compensation. When compared to the peak filter modification, the addition of phase compensation minimally affects the robustness. Figure 3.12 shows the maximum singular value of the sensitivity. The phase advance internal model gives the desired deep notches in the sensitivity, but sacrifices some performance in the region where the frequencies are close together such as 180 Hz and 200 Hz. It is important to note to place internal modes close together is another advantage of this formulation since the bandwidth can be adjusted easily when designing the peak and phase compensation filters.

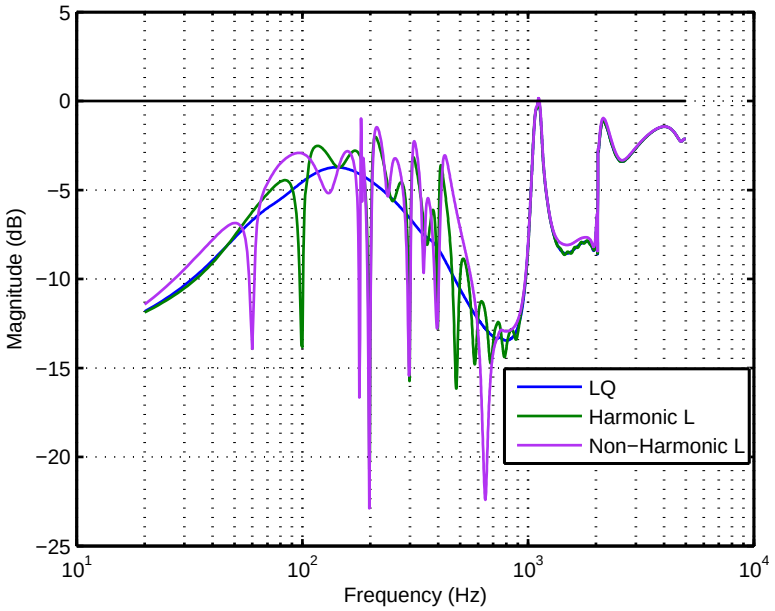

Figure 3.11: Robustness analysis of the repetitive design procedure with the peak filter modification compared against classical repetitive and LQGi

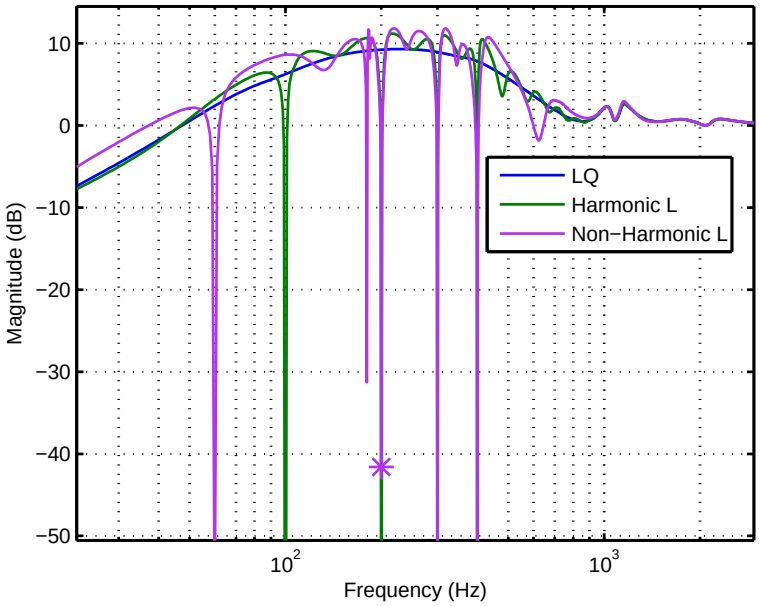

Figure 3.12: Sensitivity/performance analysis of the repetitive design procedure with the peak filter modification compared against classical repetitive and LQGi

3.4 Experimental Results

The effectiveness of the controllers were verified on the AMBS. The control used a real-time target, sampling at 10 kHz. The experimental results are presented in a manner to show the advantages of the different controllers. First, the classical repetitive with robust inversion design is shown along side the LQGi controller. Secondly, the classical repetitive controller is compared against the peak filter modification for both 200 and 400 Hz. Lastly, the phase advance controller is compared the peak filter modification to highlight the attenuation of 60 and 180 Hz.

3.4.1 Repetitive Control and LQGi

The repetitive controller designed used a 5th order Q filter with a cutoff at 800 Hz and 10 preview steps.The add-on repetitive controller was verified on the system under three conditions:

1. first a reference of 200 Hz and amplitude of 7.5 μm was tracked on the front two axis, while the back to regulated to zero. This is a simple circle cutting type profile.

2. secondly, the spindle was spun to 200 Hz and was tested whether the controller can regulate it about its geometrical axis.

3. lastly the reference was again injected while the rotor was spinning, testing both disturbance and reference tracking of the controller.

3.4.1.1 Reference Tracking

The results of the reference only tracking experiment is shown in figure 3.13. The plot is only shown for **one** of the front axis because the others are similar. The top plot shows the reference (red), tracking with only LGQi (green), and with the add-on repetitive (blue) in the time domain; while the bottom shows a spectral plot of the error, $r - y$. Clearly, repetitive track much better, with 40 dB less error at the main fundamental. The second-largest

component is at 180 Hz, most likely a manifestation of the mains hum. The controllers are stable and able to track the reference with less than one micron of error, tracking a 15μm (peak-to-peak) reference. Tracking performance is good, without amplifying sideband frequencies.

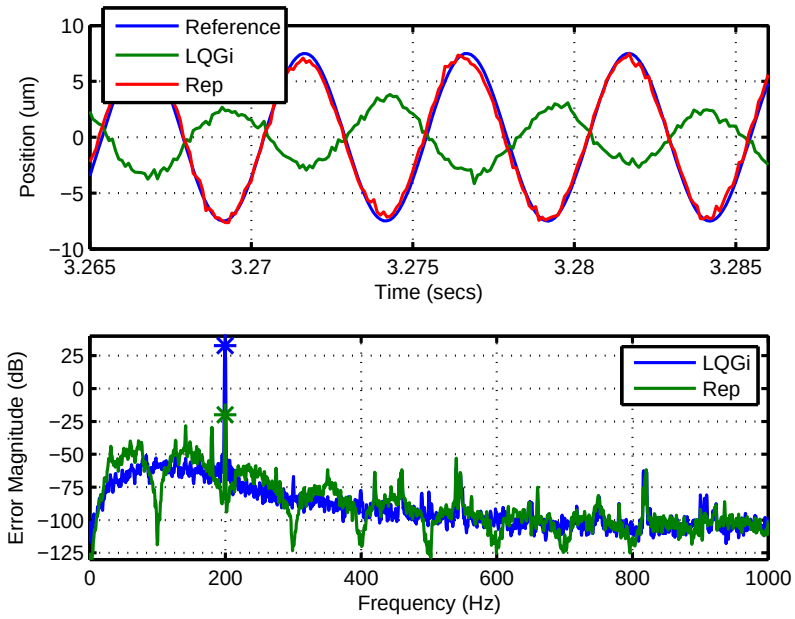

Figure 3.13: 200Hz Tracking Results–the spindle is tracking a 200 Hz reference on its front two axis while not spinning

3.4.1.2 Disturbance Rejection

The disturbance caused by the spindle spinning at 200 Hz amounts to 12,000 RPM—in the acceptable high speed machining region. Figure 3.14 shows both time-domain and spectral results of this experiment. Due to mass imbalance, spinning the spindle causes it to vibrate at the spin frequency. From the time domain results, it is seen that the LQGi controller has about 7.5 μm vibration. This is unacceptable for cutting applications that need precision tracking. The repetitive controller is able to reject this disturbance and center itself. Also, from the LQGi spectral plot, the spinning at 200 Hz introduces vibrations 300 Hz, 400 Hz, 500Hz, and 600Hz albeit smaller magnitude than the fundamental. One of the main

advantages of repetitive controller is that by placing the internal model at 100 Hz, it is able to target integer frequencies as well. The spectral plot show that the repetitive controller have control action at integers of 100 Hz as is expected, but tapers off after 600 Hz due to the Q filter. Therefore it is able theses harmonic disturbances.

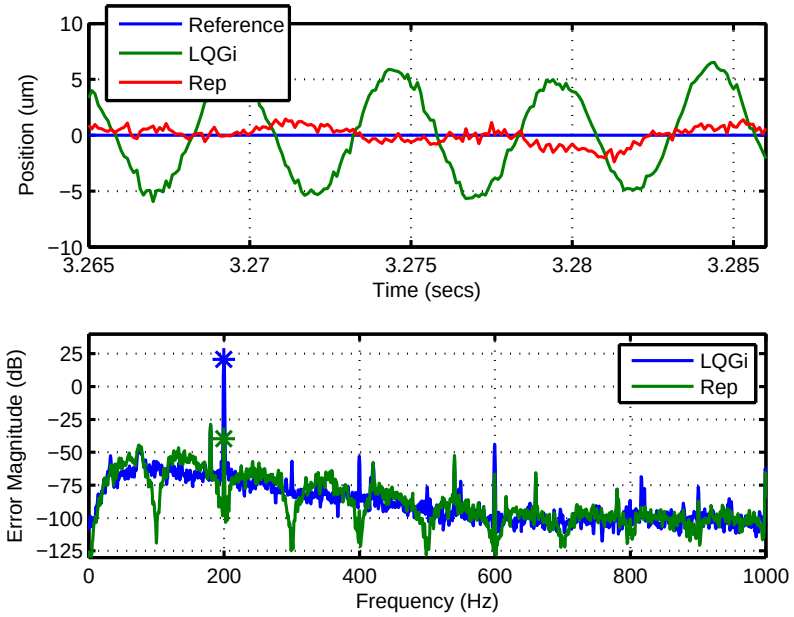

Figure 3.14: 200Hz Disturbance Rejection Results–the spindle is spinning without any reference

3.4.1.3 Reference Tracking and Disturbance Rejection

In the final experiment, the spindle was spun to 200 Hz and the front to axis attempted to track a 200 Hz reference. The results are shown in figure 3.15. From the time domain results the LQGi controller cannot track the reference, it is even 180 degrees phase shifted from the reference and heavily affected by the spinning. The repetitive controller is able to reject the disturbance which occurs on all four axis while tracking at non-spinning levels on the front two. Main conclusion to be drawn is the repetitive controller is able to reject the spin frequencies and its harmonics, while tracking as if the spindle was not spinning.

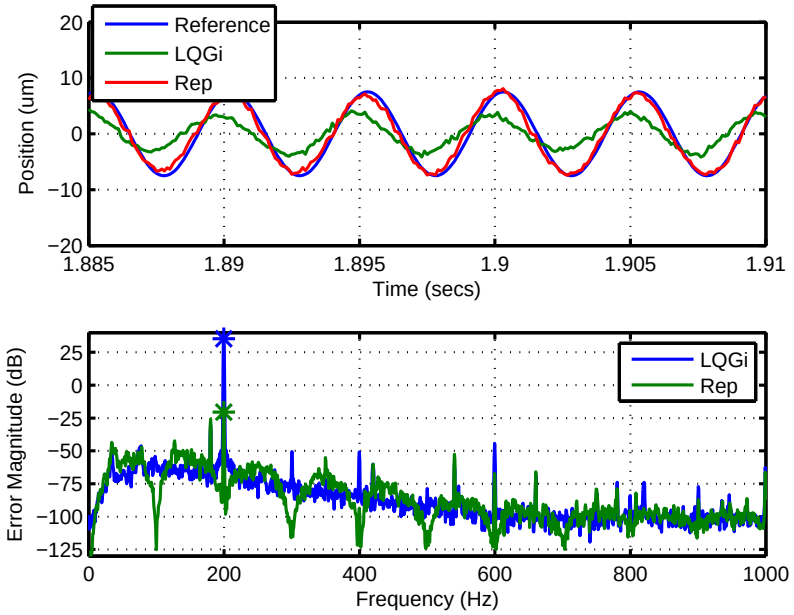

Figure 3.15: 200Hz Reference and Disturbance Rejection Results – the spindle is spinning and a 200 Hz reference injected on its front two axis

Results of the three experiments are summarized in Table 3.1 and 3.2. The repetitive add-on outperforms the LQGi controller in terms of RMS error. The results show that including the repetitive controller can bring tracking/disturbance error to almost purely levitating levels on all axis.

Channel	**RMSe**[1]	**RMSe**[2]	**RMSe**[3]	**RMSe**[4]
V13	.41	.76	.55	.66
W13	.46	.82	.60	.77
V24	.48	.60	.70	.67
W24	.45	.65	.62	.63

Table 3.1: RMS error for repetitive controller when (1)just levitating, (2) only tracking,(3) only spinning, and (4)both spin and track. All units are μm.

Channel	RMSe[1]	RMSe[2]	RMSe[3]	RMSe[4]
V13	.41	7.06	4.95	7.37
W13	.46	7.53	3.96	9.5
V24	.48	.53	5.56	4.9
W24	.45	.62	5.84	5.5

Table 3.2: RMS error for LQGi controller when (1)just levitating, (2) only tracking,(3) only spinning, and (4)both spin and track. All units are μm.

3.4.2 Peak Filter Modification

The peak filter placed an internal model at 100, 200, 300, and 400 Hz. The controller was then compared to both classical repetitive and LQGi under the following conditions:

1. first the spindle was spun to 200 Hz and a circle reference was injected.

2. the spindle was spun to 400 Hz and the corresponding circle reference was injected

Figures 3.16 and 3.17 show the error spectrum of the position for both 200 and 400 Hz. The top plots on both is when the spindle is just levitating, without any tracking, while the bottom is both spinning and tracking as would be encountered in a cutting application. The main takeaway is that by modifying the internal model using a peak filter, better performance is achieved when compared to repetitive control. This especially true when tracking 400 Hz while spinning where the targeted frequencies are attenuated by over 20 dB as suggested by the sensitivity analysis. In terms of maximum rms error for each of the four axis, at 400 Hz tracking, repetitive control has 1.2 μm while the peak filter modification has only .85 μm.

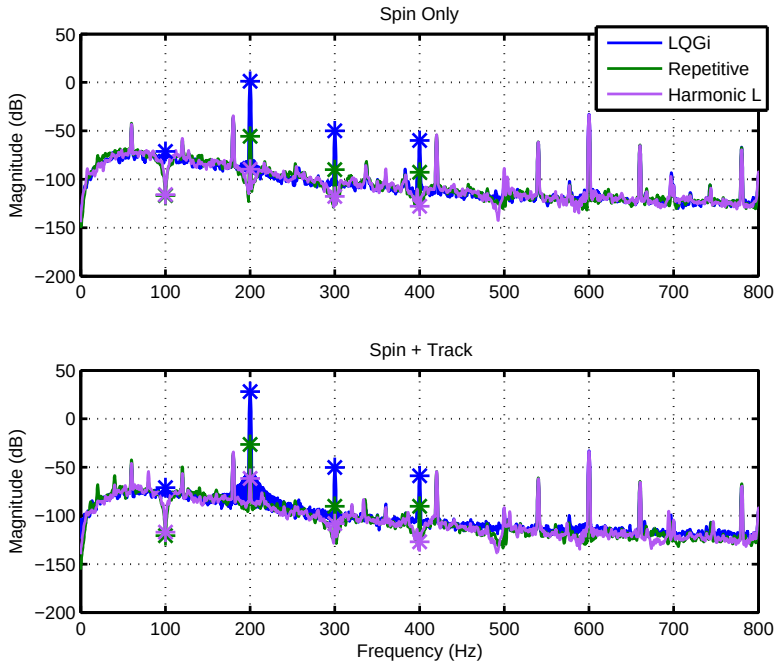

Figure 3.16: 200Hz Reference and Disturbance Rejection Results – the spindle is only spinning on the top and spinning while tracking on the bottom

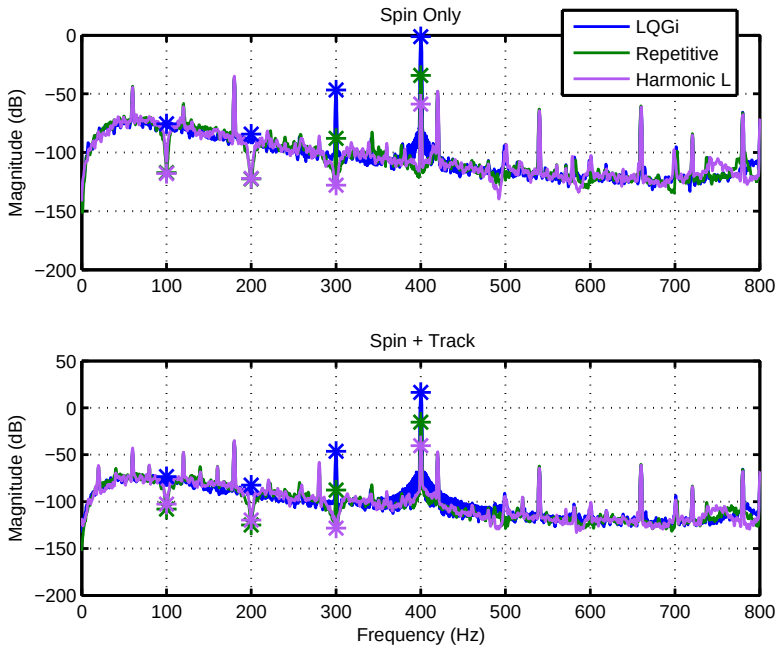

Figure 3.17: 400Hz Reference and Disturbance Rejection Results – the spindle is only spinning on the top and spinning while tracking on the bottom

3.4.3 Peak Filter with Phase Compensation

The peak filter with phase compensation placed an internal model at 60, 180, 200, 300, and 400 Hz. The controller was then compared to the peak filter modification under the following conditions:

1. first the spindle was spun to 200 Hz and a circle reference was injected.

2. the spindle was spun to 400 Hz and the corresponding circle reference was injected

Figures 3.18 and 3.19 show the position error spectrum of the peak filter with phase compensation and repetitive peak filter. In both the 200 Hz and 400 Hz case, using the phase compensation technique allows for targetting of the 60 and 180 Hz noise present in the system. From the figures, it is apparent there is large 60 and 180 Hz and indeed targeting these frequencies reduces the overall rms error. The maximum rms error for repetitive control with peak filter is .85 μm while using phase compensation lowers it to .73 μm.

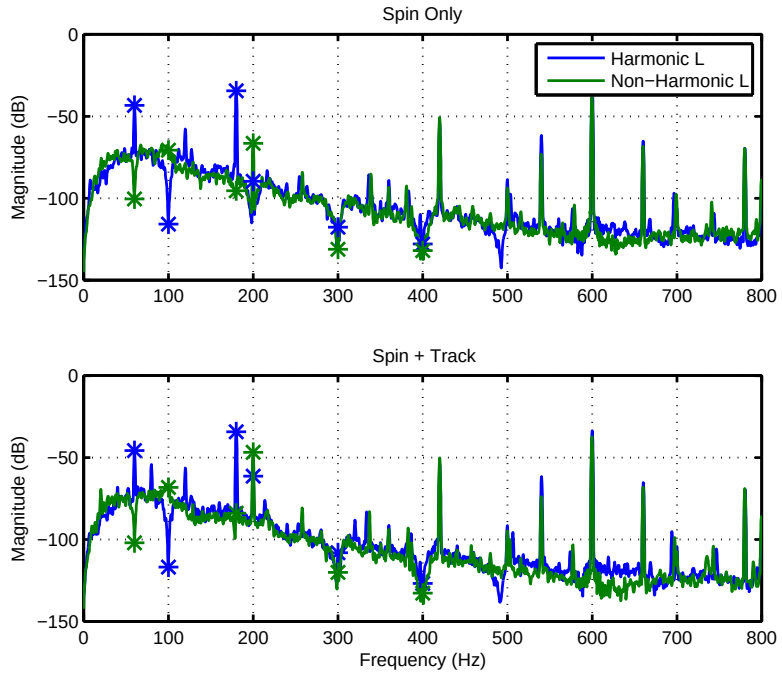

Figure 3.18: 200Hz Reference and Disturbance Rejection Results – the spindle is only spinning on the top and spinning while tracking on the bottom

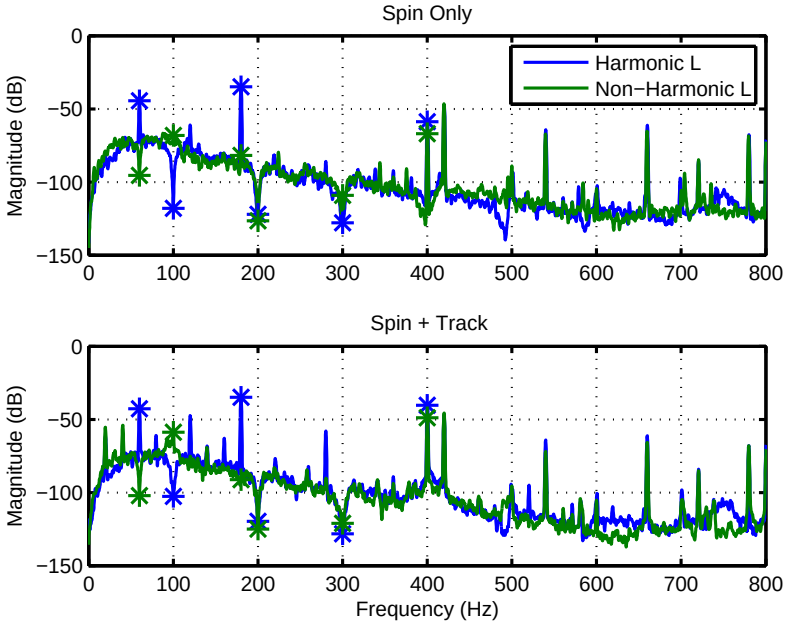

Figure 3.19: 400Hz Reference and Disturbance Rejection Results – the spindle is only spinning on the top and spinning while tracking on the bottom

3.4.4 Circles, Ovals, and Control Effort

There are two obvious ways to move the spindle such that the tip carves out a specific trajectory: 1) Translate both the front and rear sensors so that whole spindle translates 2) Regulate the rear sensors while tracking a specific trajectory in the front to get an amplification effect, this is called rotational. Figure 3.20 shows the phase portrait of both the front and rear sensors when tracking a 200 Hz circle using both LQGi and repetitive control; the top two plots are the translational approach, while the bottom two is the rotational. The LQGi cannot track trajectories while repetitive can.

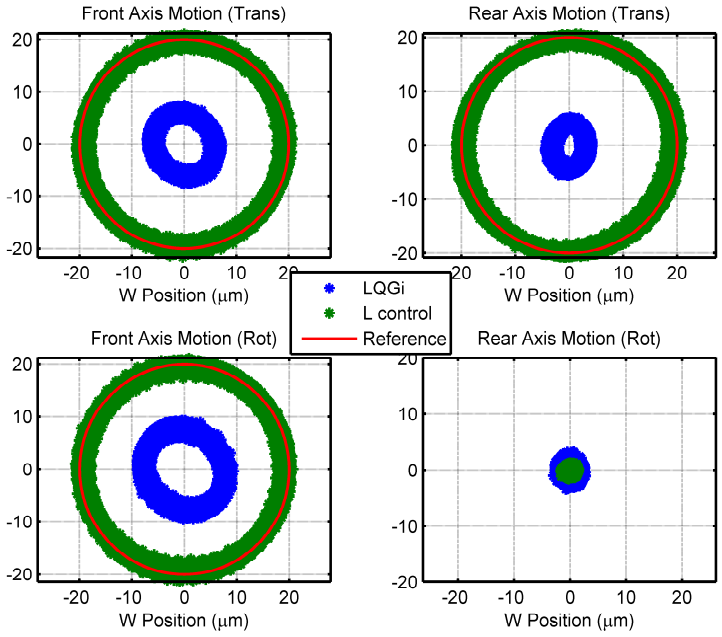

Figure 3.20: The top two plots is tracking a circle profile at 200 Hz by translating both the front and rear axis (translational), while the bottom is tracking a circle by tracking a circle on the front and regulating the rear (Rotational). Clearly, the repetitive control with peak filter is able to track circles while the LQGi cannot.

Figure 3.21 shows the control effort using the translational and rotational approach. This highlights the main advantage of using the rotational approach, the control signal is reduced by over 100 percent.

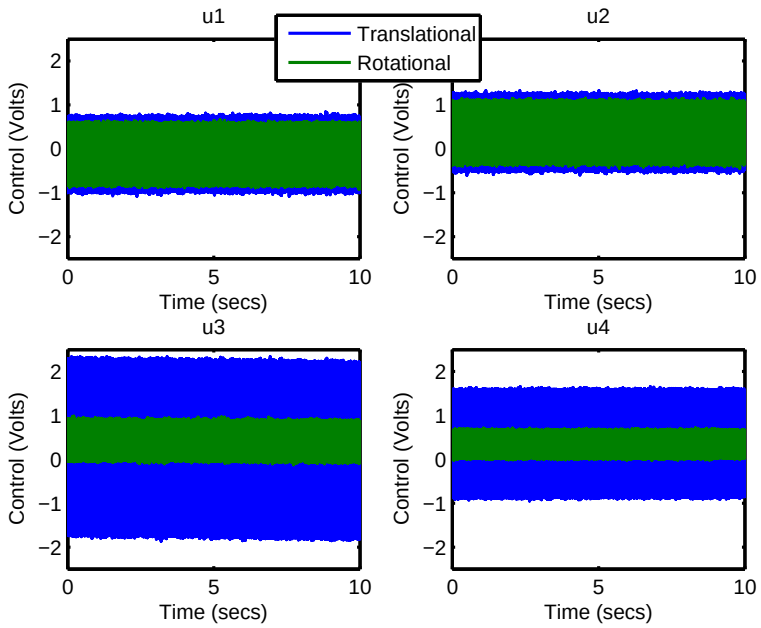

Figure 3.21: The control signal of each of the four axis when tracking a circle using repetitive control. Tracking at both and front and rear (Translational) is compared to only tracking at the front while regulating the rear (Rotational).

3.22 shows the tracking results for an oval profile, that is obtained by tracking a sine and cosine of different magnitudes.

Figure 3.23 shows the control effort tracking an oval. Using the rotational approach, the control effort is reduced.

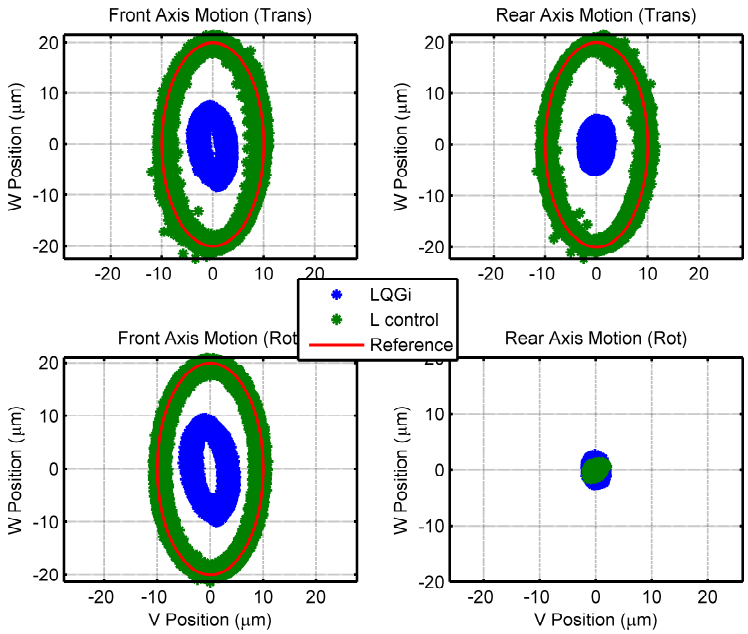

Figure 3.22: The top two plots is tracking an oval profile at 200 Hz by translating both the front and rear axis (translational), while the bottom is tracking an oval by tracking a circle on the front and regulating the rear (Rotational).

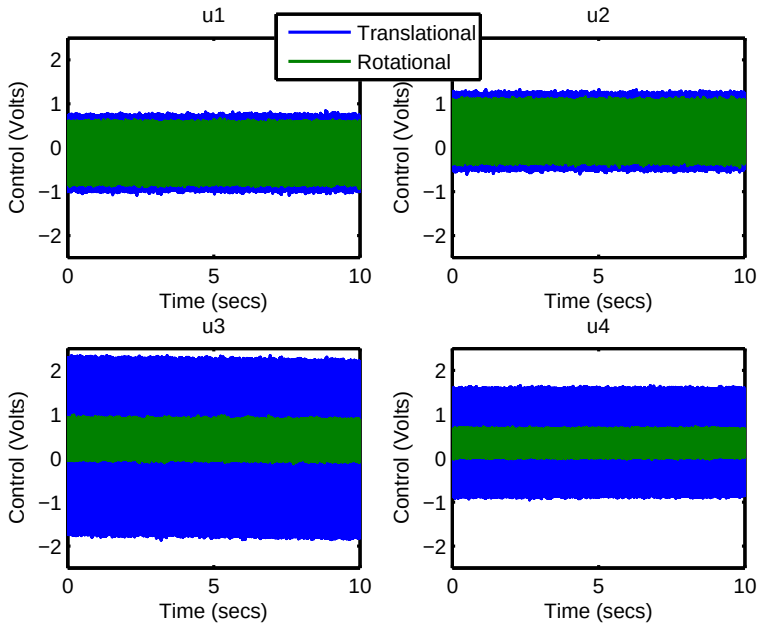

Figure 3.23: The control signal of each of the four axis when tracking an oval using repetitive control. Tracking at both and front and rear (Translational) is compared to only tracking at the front while regulating the rear (Rotational).

3.4.5 Tip Tracking

In a cutting application, the primary concern is the tool tip tracking performance. It is expected that tracking of the feedback sensors are directly correlated with the tip tracking performance, figures 3.24 and 3.25 verify this. The figures show the tip tracking for a circle and oval using LQGi and repetitive control at 100 and 200 Hz. Repetitive control is able to track the tip adequately while LQGi cannot. It is also important to note that the spindle is **not** spinning, since the eddy current position sensors at the tip are not able to give reliable measurements while spinning.

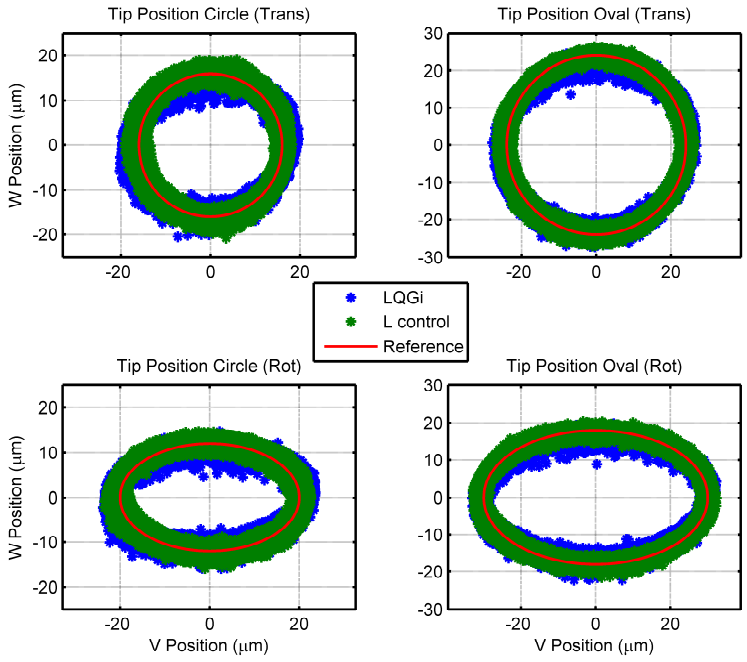

Figure 3.24: Tracking at the tip using LQGi and repetitive control for both a circle and oval at 100 Hz, the spindle is not spinning.

Since the spindle is not spinning, the LQGi seems to have better performance than in actuality. At 200 Hz, the benefit of using repetitive control is seen more clearly.

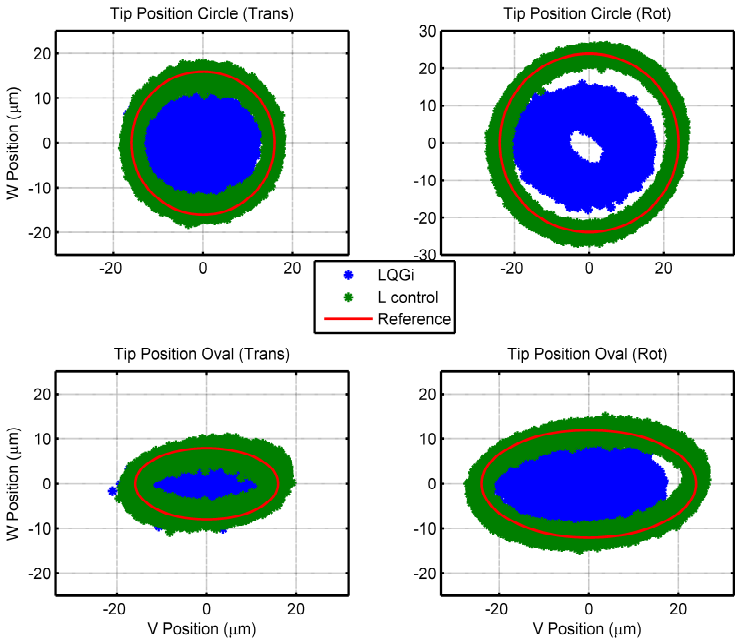

Figure 3.25: Tracking at the tip using LQGi and repetitive control for both a circle and oval at 200 Hz, the spindle is not spinning.

CHAPTER 4

Cutting Process

In this chapter, the inclusion of a cutting model is considered in the overall control system. The stability of the control system with the tracking controllers is analyzed for the onset of chatter. Furthermore, experimental cutting experiments verify the validity of the overall control design procedure.

4.1 Reference Generation

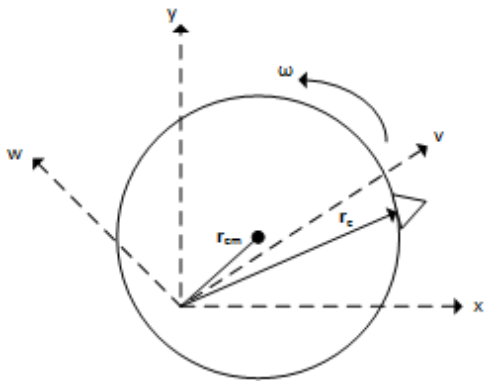

Figure 4.1: Simple kinematics of the tracking problem for cutting

Figure 4.1 shows the simple kinematics for the tracking problem. The objective is to carve out a trajectory by keeping the cutter on the surface of the work piece by moving the center of mass. To that effect, it can be seen that the position of the cutter is given by

$$\mathbf{r_c} = (x_{cm} + rcos(\theta_c))\hat{x} + (y_{cm} + rsin(\theta_c))\hat{y} \tag{4.1}$$

where θ_c is the angle of the cutter that is dependant on the spin frequency ω. Therefore to carve out circle or ellipses, the reference should track

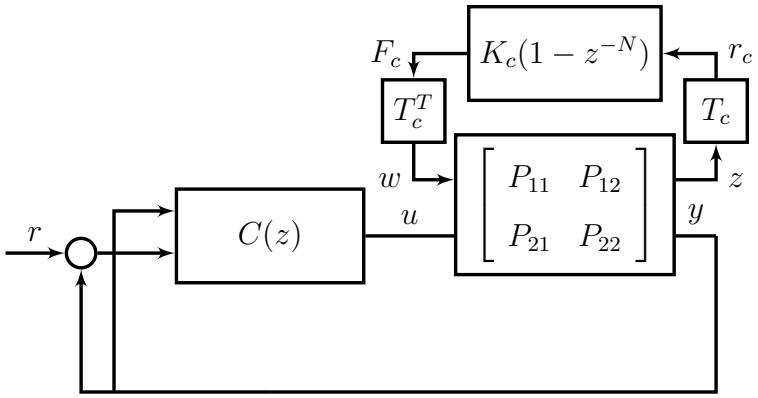

Figure 4.2: Overall block diagram of the linearized cutting process with the three main parts: 1) augmented plant with tip dynamics 2) internal model control for reference tracking 3) cutting dynamics

$$\begin{aligned} r_x &= acos(\theta_c) \\ r_y &= bsin(\theta_c) \end{aligned} \tag{4.2}$$

The reference is generated by the encoder angle while the spindle is spinning, which gives the cutter angle.

4.2 Overall Cutting Process

Figure 4.2 shows the overall schematic of the linearized cutting process. There are three major parts of the process:

1. The six input and six output augmented plant. The inputs are the four current commands for the coils and two cutting forces at the tip. the outputs are the four displacements near the coils and two displacements at the tip. In chapter 2, the model was derived in detail.

2. The controller $C(z)$ stabilizes the magnetic bearing and contains and internal model to track the reference as required by the application to minimize tracking error. The controller design and analysis was detailed in chapters 2 and 3.

3. The cutting dynamics that relates the tip displacements to cutting forces. The inclusion of this model is essential as it predicts chatter instability and can be used to determine optimal cutting speeds. This is the main focus of this chapter.

The following summarizes the dimensions of the various signals in the system

$$\begin{aligned} r, u, y &\in \mathbb{R}^{4x1} \\ w, z &\in \mathbb{R}^{2x1} \\ r_c, F_c &\in \mathbb{R} \end{aligned} \tag{4.3}$$

r is the reference that is determined by the trajectory profile for cutting, u is the input current to the coils, y is the displacement near the coils, w is the cutting forces in the two axis, z is the tip displacement for the two axis, r_c is the radial displacement at the cutter, and F_c is the cutting force in the radial direction at the cutter.

4.2.1 Chatter Model

Chatter is self-excited vibrations induced by variations in the cutting force that manifests itself as noticeable marks on the surface that directly affect productivity. Chatter is a complex phenomenon that depends on the tool, workpiece geometry, and mounting. The cutting conditions, such as depth of cut (doc), width of cut, and cutting speed greatly affect the onset of chatter.

The commonly used model for cutting force is that it is proportional to the cutting area by a factor known as the "cutting stiffness"

$$F_c = K_c A_c \tag{4.4}$$

In a boring type application, such as the magnetic bearing system in this thesis, the area can be expressed as

$$A_c = (\frac{f}{\Omega})(\delta) \tag{4.5}$$

where f is the feedrate, Ω is the spin frequency in Hertz, and δ is the depth of cut. The depth of cut depends on surface of the previous pass, which causes the variation in the

cutting force, and can be expressed as

$$\delta = r_c(0) + r_c(t) - r_c(t-\tau) \tag{4.6}$$

where $\tau = \frac{1}{\Omega}$ and is the time it takes to make one revolution. Combining the above equations, the widely used linear cutting force model is obtained

$$F_c = \frac{K_c F R}{\Omega}(r_c 0 + r_c(t) - r_c(t-\tau)) \tag{4.7}$$

This relates the radial tip displacement to the radial cutting force and forms a feedback loop in the cutting process as shown in figure 4.2. The forces and displacements at the tip are in two perpendicular axis which is related to the radial cutting direction by

$$r_c = \begin{bmatrix} cos(\theta_c) & sin(\theta_c) \end{bmatrix} z \tag{4.8}$$

$$w = \begin{bmatrix} cos(\theta_c) \\ sin(\theta_c) \end{bmatrix} F_c \tag{4.9}$$

and $Tc = \begin{bmatrix} cos(\theta_c) & sin(\theta_c) \end{bmatrix} z$ is the transformation of the rectangular displacements to the radial cutting direction. Also, without loss of generality, r can be assumed to be 0 since it has no impact on chatter instability. Therefore,

$$G = lft(P(z), K(z)) \tag{4.10}$$

where $P(z)$ is the augmented plant and $K(z)$ is the controller assuming $r = 0$. Furthermore, the tip displacements and cutting forces are independent and the off-diagonal terms are small so the closed loop system has the form

$$G = g(z) I_{2x2} \tag{4.11}$$

where $g(z)$ is now siso. Putting all these insights together, the overall block diagram (figure 4.2) can be greatly simplified into figure 4.3. The delay term in the cutting model is put into its discrete equivalent and the linear cutting stiffness is

$$K_{cl} = \frac{K_c f}{\Omega} \tag{4.12}$$

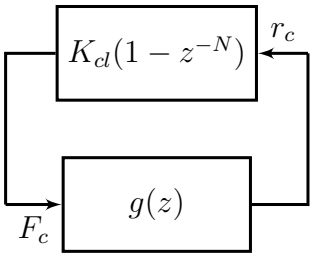

Figure 4.3: Simplified siso model for the prediction of chatter instability

4.2.2 Stability Lobes

The value of K_{cl} which the feedback system in figure 4.3 is stable for a given cutting speed $N = \frac{1}{\Omega}$ is used to create the stability lobe diagram. This value is simply the gain margin of the overall feedback system and can be obtained by

$$K_{cl}(N) = \frac{1}{|g(e^{j\omega_{cp}T_s})(1 - e^{j\omega_{cp}NT_s})|} \tag{4.13}$$

where ω_{cp} is the phase crossover frequency (180 degree crossover). Practically this can be determined by looking at the leftmost point in the Nyquist plot. Also in the worst case $e^{j\omega_{cp}NT_s}) = -1$ and the above equation becomes speed independent and a critical cutting stiffness can be obtained, which gives the stiff below which the cutting process is stable for all speeds

$$K_{cl}^{crit} = \frac{1}{|2g(e^{j\omega_{cp}T_s})|} \tag{4.14}$$

Figure 4.4 shows the stability lobe diagram for the magnetic bearing system with the LQGi controller and add-on repetitive with peak filter. The closed loop system was obtained for the identified augmented plant and the given feedback controller. The LQGi controller is stable for all cutting process with a linear stiffness less than $.2\frac{N}{\mu m}$, while the add-on repetitive controller is stable for values less than $.15\frac{N}{\mu m}$. The cutting stiffness being lowered by the add-on repetitive structure is expected since the added performance comes at the cost of robustness. It is important to note that the LQGi controller cannot be used for actual cutting since it is unable to reject the spin disturbance or track sinusoidal references. Also interesting is the stability lobe diagram is determined experimentally through system identification procedures.

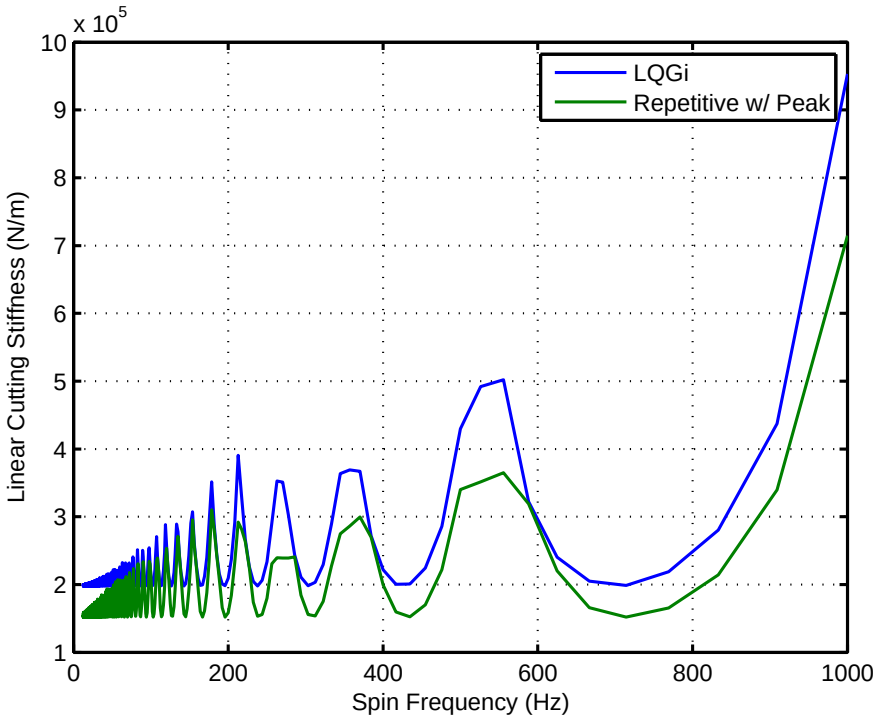

Figure 4.4: Stability lobe diagram for the LQGi and repetitive controller

Figure 4.5 shows the crossover frequency as the spin frequency increases for both LQGi and repetitive controller. Most striking is that the crossover frequency is at near the first mode for almost all spin frequencies, which indicates chatter instability. However, at some frequencies, the crossover is at the rigid body modes which indicates the cutting process will cause traditional instability.

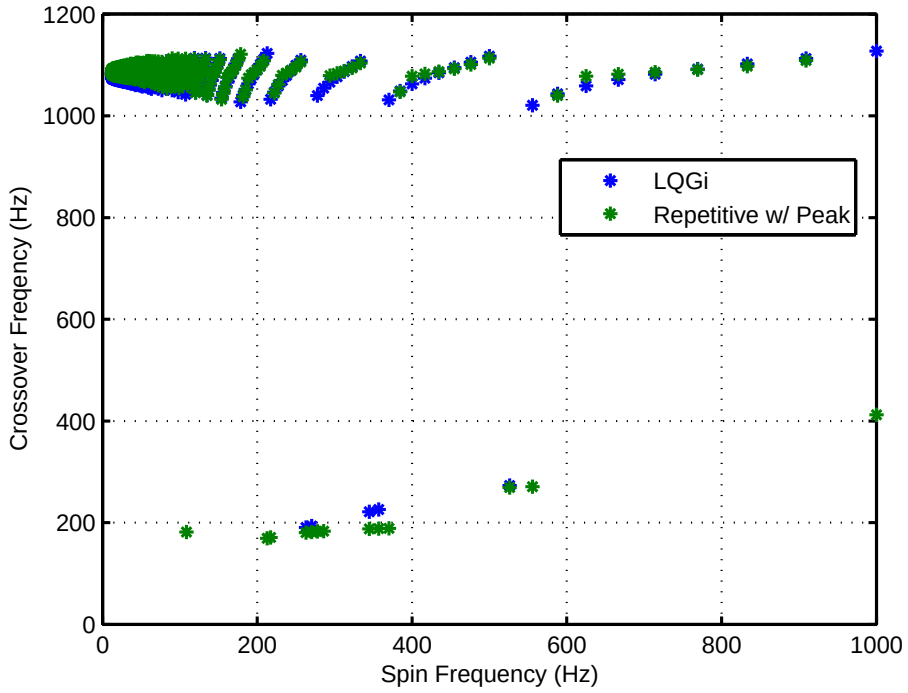

Figure 4.5: The crossover frequency at which instability occurs for the magnetic bearing system with cutting model

4.3 Experimental Results

Cutting experiments were conducted to verify the control design procedure for various depth of cuts and feedrates. An aluminium workpiece was used to bore out circles. Figure 4.6 shows the vibration level for $40\mu m$, $60\mu m$, and $80\mu m$ depth of cuts at a feedrate of 1.7 mm/s and spin frequency of 100 Hz (6000 RPM). Although a change in the vibration levels is seen, it is relatively small and most importantly no chatter was seen during these set of experiments. This reinforces the linear cutting model where the gain is determined by the feedrate and spin frequency.

Figure 4.7 summarizes the cutting experiments conducted at a depth of cut of 20 μm and various feedrates and spin frequencies of 100 and 150 Hz with respect to the stability lobe diagram. Chatter was observed at a feedrate of 3.5 mm/s when spinning at 100 Hz which was used to obtain the cutting stiffness and the other points were created with respect

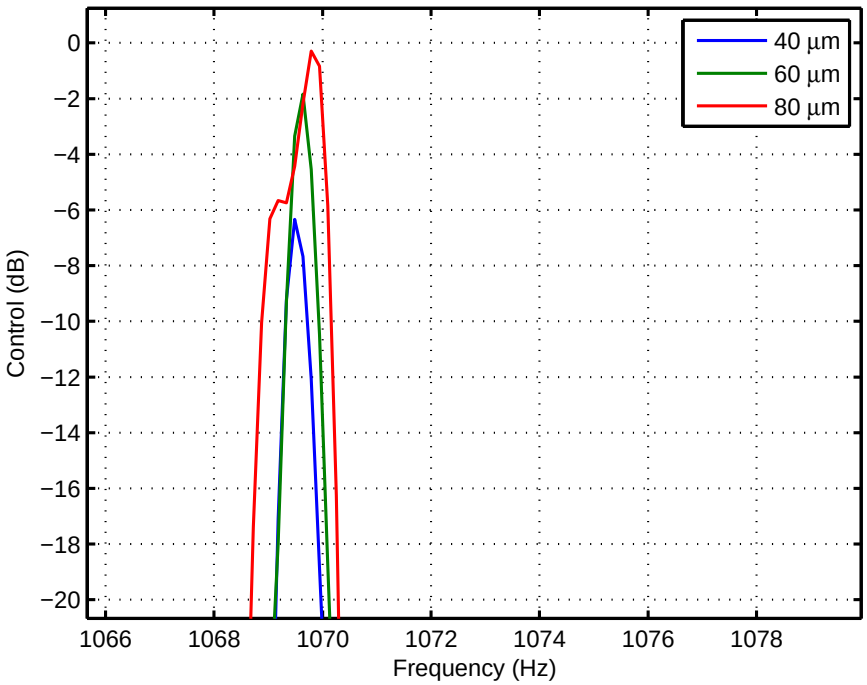

Figure 4.6: Vibration levels of the control input for various depth of cuts at a feed rate of 1.7 mm/s, no chatter was seen

to that point. Therefore, changing the feedrate and spin frequency corresponds to moving up and down on the stability lobe. At higher spin frequencies, the linear cutting stiffness is increased and less chatter is observed. This was experimentally seen, as at 150 Hz (9000 Hz), no chatter was observed even as the feedrate was increased to 7.5 mm/s. Feedrates faster than this actually starts threading the work piece. Figure 4.8 shows two actual cut pieces: the one of the left is a clean cut, while the one on the right is a chattered piece with the marks clearly visible.

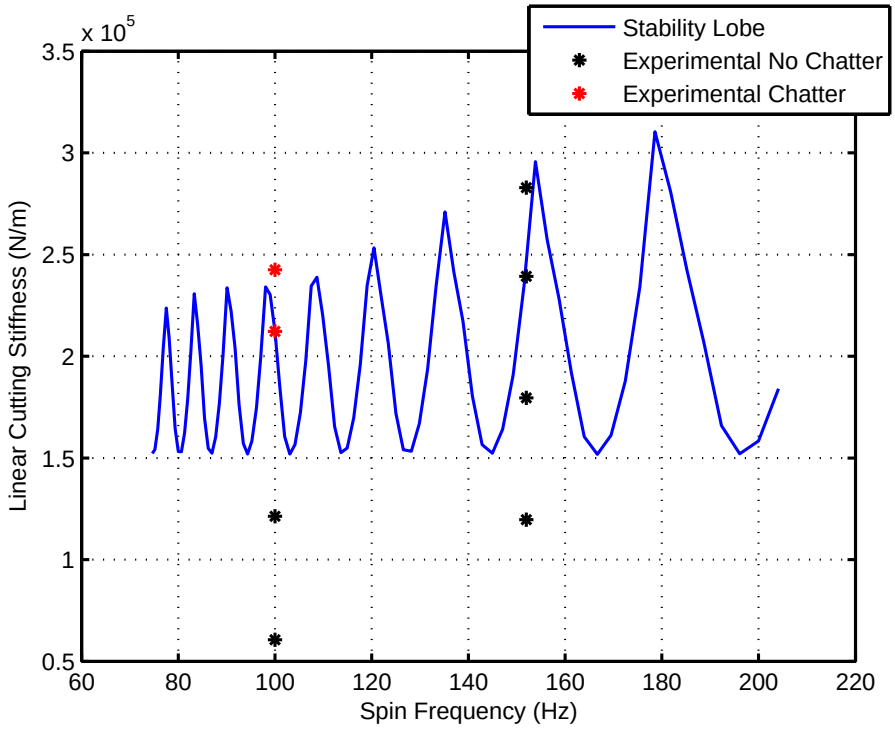

Figure 4.7: Summary of the experiments conducted at a depth of cut of 20 μm to verify the validity of the stability lobe diagram. No chatter was observed when cutting at 150 Hz as the instability limit was approaching threading.

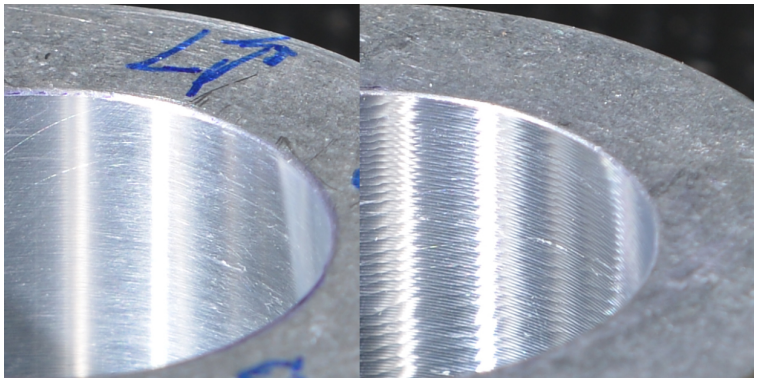

Figure 4.8: Actual workpieces: the left is a clean cut, and the right is a chattered piece.

4.3.1 Vibration Levels

Figure 4.9 shows the vibration levels for feed rates of 1 mm/s, 2 mm/s, and 3.5 mm/s when cutting at 100 Hz. As the feed rate increases, the vibration levels increase as well. Figure 4.10 shows the vibration levels at the higher spin frequency of 150 Hz (9000 RPM). The vibration frequency when cutting at 100 Hz is around 1069 Hz, while at 150 Hz it is shifted down to 1033 Hz; this is expected from the crossover frequency analysis and is indeed seen during experiments.

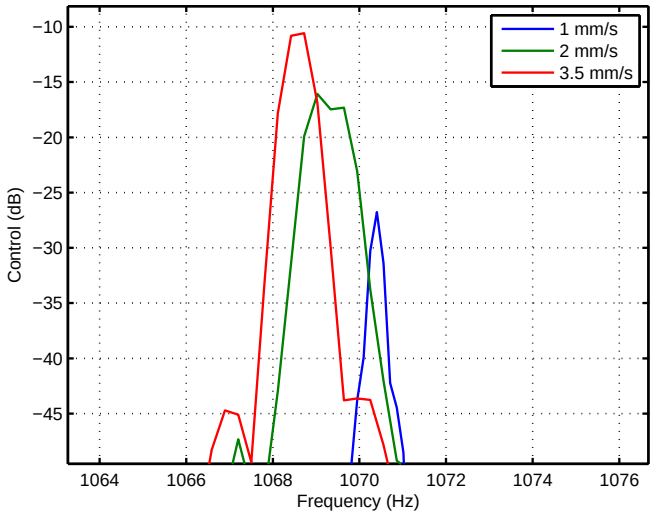

Figure 4.9: Vibration levels of the control input for various feed rates at 20μm depth of cuts and a spin frequency of 100 Hz, chatter was seen at a feed rate of 3.5 mm/s

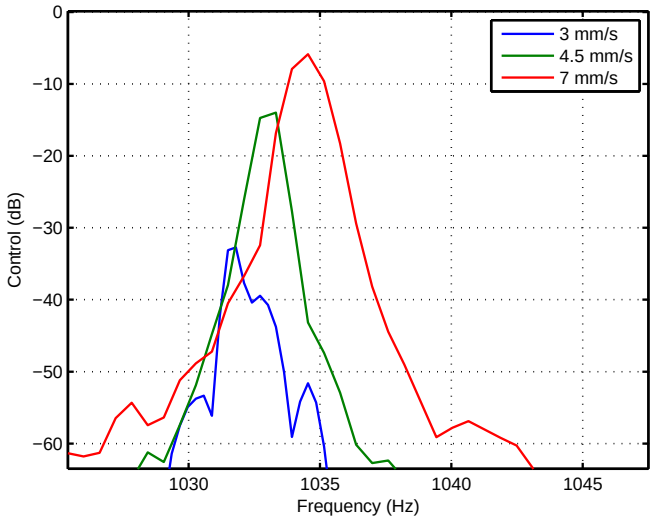

Figure 4.10: Vibration levels of the control input for various feed rates at 20μm depth of cuts and a spin frequency of 150 Hz, chatter was not observed at the higher spin frequency

4.3.2 Tracking Error

Figure 4.11 shows the tracking results for a 20 μm circle cut of aluminium. The top plots shows the error spectrum for both with and without cutting, cutting predominately excites the first flexible mode while not affecting the other frequencies too much. The bottom plots show the feedback sensors tracking; the front sensors track a circle (blue) while the back regulates to zero. Figure 4.12 shows the tracking results for a chattered piece. The first flexible mode is excited more during chatter and the tracking error is visibly larger than without cutting.

Figure 4.13 shows tracking error results for a 20/40 μm oval cut as would be expected in a piston wrist pin boring application. Similar to the circle case, only the first flexible mode is excited and the others are not affected too much.

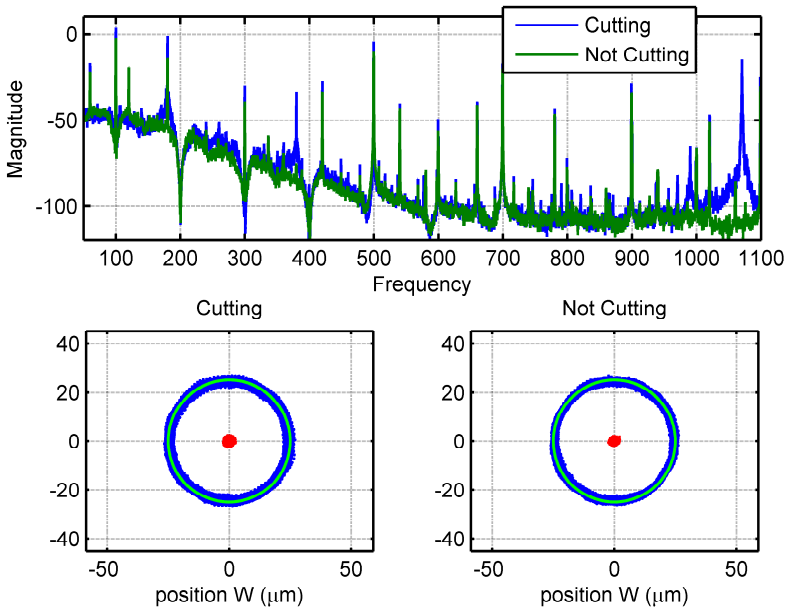

Figure 4.11: Tracking results from a 20 μm circle cut that did not chatter. The top plots shows the error spectrum with and without cutting. The bottom plots show the feedback sensors tracking; the front sensors track a circle (blue) while the back regulates to zero (red).

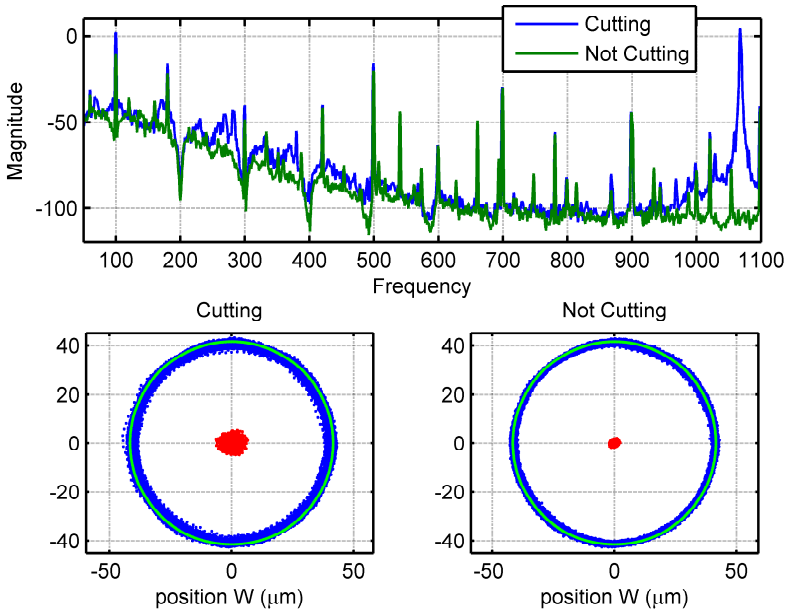

Figure 4.12: Tracking results from a 20 μm circle cut that did chatter. The top plots shows the error spectrum with and without cutting. The bottom plots show the feedback sensors tracking; the front sensors track a circle (blue) while the back regulates to zero (red).

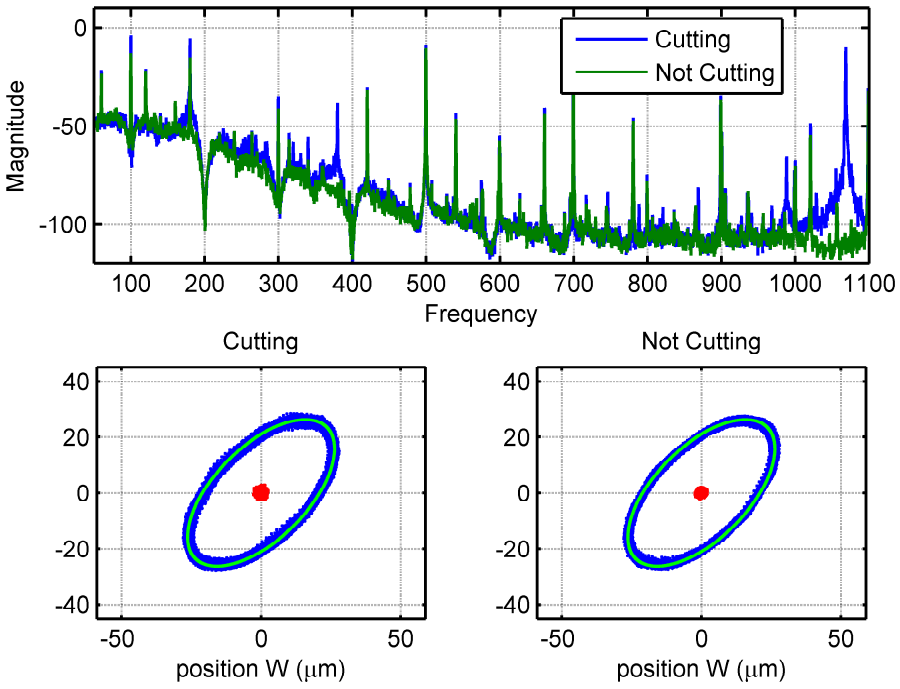

Figure 4.13: Tracking results from a 20/40 μm oval cut that did not chatter. The top plots shows the error spectrum with and without cutting. The bottom plots show the feedback sensors tracking; the front sensors track an oval (blue) while the back regulates to zero (red).

4.4 Fault Detection

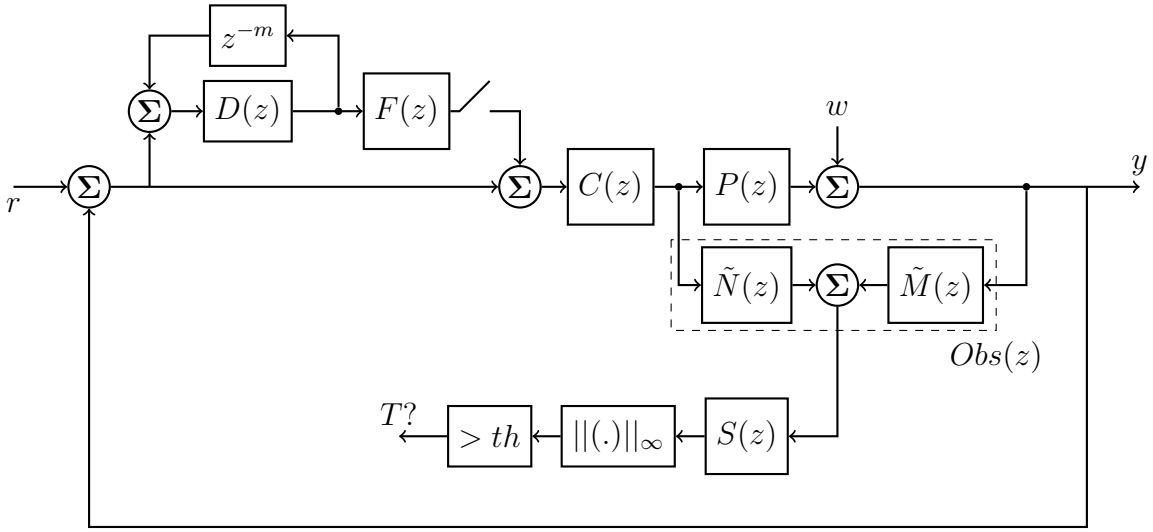

Figure 4.14: The fault detection scheme

As noted the cutting process introduces extra dynamics that the system must be robust against. The overall cutting process along with the unstable magnetic bearing system is very complex and unexpected behavior can occur that can be catastrophic; therefore, a fault detection scheme that is able to handle unexpected behavior is necessary. The main idea behind fault detection is if the system behavior deviates from the model then to reconfigure the system into a safer state.

Figure 4.14 shows the control system with fault detection included. If a fault is detected, then the add-on repetitive control is disconnected from the system and the AMBS is levitated by the robust LQGi controller. The observer is constructed such that only the model is weighted, hence it is a low gain observer, or the smallest observer gain that stabilizes the open loop system. The residual from the observer is then filtered through the nominal sensitivity, which gives an indication of the frequency region where the system is robust. If this signal is greater than a preset threshold, then the add-on repetitive controller is disconnected and the cutting process stopped.

CHAPTER 5

Vibration Suppression

In this chapter, we consider the problem of spinning the rotor along its inertial axis which reduces the amount of vibration transmitted to the housing and the synchronous current at the spin frequency. An adaptive feeedforward algorithm is used for this purpose. The adaptive feedforward algorithm is able to treat both the inertial balancing and geometrical centering problem and is advantageous in many respects. First, the seemingly opposites tasks (ones places a notch and the other infinite control action in the feedback) can be switch between the same algorithm. Also, since they both have a LTI equivalent, both can be analyzed using the wide range of LTI techniques. Lastly, the adaptive feedforward algorism injects references to cancel the disturbance, therefore it inherently identifies the mass imbalance or misalignment and can be turned off during operation if needed. The internal model type controllers do not have this luxury.

5.1 Problem Setup and Adaptive Algorithm

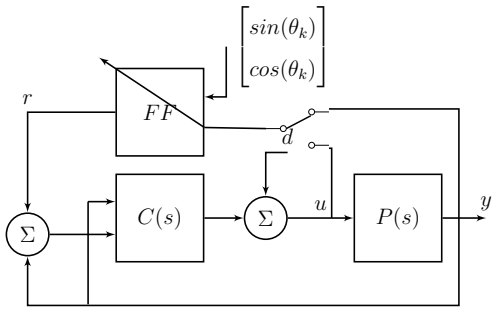

Figure 5.1: Block diagram of the adaptive feedforward controller with sinusoidal regressors

Figure 5.1 shows the block diagram for the problem considered. The plant ($P(s)$) is nxn,

square, and can be unstable with output y and input u. The plant is also assumed to be pre-stabilized by a 2-dof controller ($C(s)$) which, for example, can be designed using LQG methods. There is also assumed to be an input disturbance at m narrow band frequencies given by

$$\mathbf{d} = \sum_{k=1}^{m} \mathbf{c_k} sin(\omega_k t + \boldsymbol{\theta_k}) \tag{5.1}$$

The goal of the controller is to minimize the control input u or the output y at the at the specified frequencies by injecting the appropriate signal r. The most simple approach in minimizing u is to place a notch filter in the control loop, but this may perturb the closed loop too much and cannot adapt when the frequencies are changing. The standard approach in minimizing y is based on the internal model principle, which is to introduce infinite control action at the specified frequencies and it has similar issues as the notch filter. In this paper, we use an adaptive feedforward approach to minimize either u or y.

To minimize the control input or plant output a gradient descent algorithm for the phase and gain of the reference signal r is used. The controller minimizes the following instantaneous cost

$$J = \mathbf{e}^T \mathbf{e} \tag{5.2}$$

where $\mathbf{e}$ can be either $\mathbf{u}$ or $\mathbf{y}$. Given that the controller can be represented as $C(s) = \begin{bmatrix} C_1(s) & C_2(s) \end{bmatrix}$,and defining the transfer function

$$S(s) = (I + (C_2(s) - C_1(s))P(s))^{-1} \tag{5.3}$$

then from figure 5.1, the control input can be written as

$$\mathbf{u} = S(s)[(C_1(s) - C_2(s))P(s)\mathbf{d} + C_2(s)\mathbf{r}] \tag{5.4}$$

Similarly, the plant output $\mathbf{y}$ can be written as

$$\mathbf{y} = S(s)[P(s)\mathbf{d} + P(s)C_2(s)\mathbf{r}] \tag{5.5}$$

Since the goal is to minimize u or y at discrete frequencies, the reference can be parameterized as

$$\mathbf{r} = \sum_{k=1}^{m} \mathbf{a_k} sin(\omega_k t) + \mathbf{b_k} cos(\omega_k t) \tag{5.6}$$

where $\mathbf{a_k}$ and $\mathbf{b_k}$ are the $nx1$ unknown array of fourier coefficients, which the adaptive controller attempts to identify. Then, depending on whether u or y is minimized, the complementary transfer function $T(s)$ is defined as

$$T(s) = \begin{cases} S(s)C_2(s), & \text{if } \mathbf{e} = \mathbf{u} \\ S(s)P(s)C_2(s), & \text{if } \mathbf{e} = \mathbf{y} \end{cases} \tag{5.7}$$

The update for the fourier coefficients is derived by a simple gradient descent law

$$\begin{bmatrix} \dot{\mathbf{a_k}} \\ \\ \dot{\mathbf{b_k}} \end{bmatrix} = \mu \begin{bmatrix} \frac{dJ}{d\mathbf{a_k}} \\ \\ \frac{dJ}{d\mathbf{b_k}} \end{bmatrix} \tag{5.8}$$

The gradient of the cost, eqn 5.2, can be evaluated by using the expression of $\mathbf{u}$ or $\mathbf{y}$ and equation 5.6 and 5.7. Then the update law becomes

$$\begin{bmatrix} \dot{\mathbf{a_k}} \\ \\ \dot{\mathbf{b_k}} \end{bmatrix} = \mu \begin{bmatrix} T(s)^T[sin(\omega_k t) I_{nxn}]\mathbf{e} \\ \\ T(s)^T[cos(\omega_k t) I_{nxn}]\mathbf{e} \end{bmatrix} \tag{5.9}$$

The notation used here is that

$$\begin{aligned} &T(s)^T[sin(\omega t) I_{nxn}] = \\ &\begin{bmatrix} T(s)[sin(\omega t)\mathbf{e_1}] & T(s)[sin(\omega t)\mathbf{e_2}] & ... & T(s)[sin(\omega t)\mathbf{e_n}] \end{bmatrix} \end{aligned} \tag{5.10}$$

$\mathbf{e_n}$ is the standard basis vector with a one in the n^{th} row and the notation $T(s)[x]$ is the input x filtered through the transfer function $T(s)$.

Since the input in equation 5.9 is either sine or cosine, then neglecting the transient, the update law simplifies to

$$\begin{bmatrix} \dot{\mathbf{a_k}} \\ \\ \dot{\mathbf{b_k}} \end{bmatrix} = \mu \begin{bmatrix} Re[T(j\omega_k)] & -Im[T(j\omega_k)] \\ Im[T(j\omega_k)] & Re[T(j\omega_k)] \end{bmatrix}^T \begin{bmatrix} sin(\omega_k t) I_{nxn} \\ cos(\omega_k t) I_{nxn} \end{bmatrix} \mathbf{e} \tag{5.11}$$

the part of the reference that cancels the k^{th} frequency in the signal is given as

$$\mathbf{r_k} = \begin{bmatrix} sin(\omega_k) I_{nxn} & sin(\omega_k) I_{nxn} \end{bmatrix} \begin{bmatrix} \mathbf{a_k} \\ \mathbf{b_k} \end{bmatrix} \tag{5.12}$$

the total reference signal to cancel all frequencies is then given by

$$\mathbf{r} = \sum_{k=1}^{m} \mathbf{r_k} \tag{5.13}$$

Equations 5.11, 5.12, and 5.13 give the state-space equations for the adaptive feedforward controller.

5.1.1 SISO Adaptive Feedforward

The standard adaptive feedforward control can be derived by assuming $T(s) = I_{nxn}$. This effectively neglects the coupling between channels and treats each input/output pairs as separate SISO systems.

$$\begin{bmatrix} \dot{\mathbf{a_k}} \\ \\ \dot{\mathbf{b_k}} \end{bmatrix} = \mu \begin{bmatrix} \mathbf{e} sin(\omega_k t) \\ \\ \mathbf{e} cos(\omega_k t) \end{bmatrix} \tag{5.14}$$

This is a much simplified descent algorithm to minimize e; but, as is shown in this paper, this type of update law may have slow convergence and high sensitivity to the learning gain especially for multivariable systems.

5.2 LTI Equivalent Controller

The multivariable adaptive feedforward controller given by equations 5.11, 5.12, and 5.13 has a LTI internal model equivalent, equation 5.15.

$$C(s) = \mu \sum_{k=1}^{m} \frac{sRe[T(j\omega_k)]^T + \omega_k Im[T(j\omega_k)]^T}{s^2 + \omega_k^2} \tag{5.15}$$

This can be seen by applying a change to coordinates (equation 5.17) to the state-space system (equations 5.11 and 5.12).

$$\begin{bmatrix} \mathbf{a_k} \\ \mathbf{b_k} \end{bmatrix} = R_k \mathbf{x_k} \tag{5.16}$$

where

$$R_k = \begin{bmatrix} sin(\omega_k t) I_{nxn} & -cos(\omega_k t) I_{nxn} \\ cos(\omega_k t) I_{nxn} & sin(\omega_k t) I_{nxn} \end{bmatrix} \tag{5.17}$$

Then the following LTI state-space system is obtained

$$\dot{\mathbf{x_k}} = \begin{bmatrix} 0_{nxn} & -\omega_k I_{nxn} \\ \omega_k I_{nxn} & 0_{nxn} \end{bmatrix} \mathbf{x_k} + \lambda \begin{bmatrix} Re[T(j\omega_k)]^T \\ -Im[T(j\omega_k)]^T \end{bmatrix} \mathbf{e} \tag{5.18}$$

with output

$$\mathbf{r_k} = \begin{bmatrix} I & 0 \end{bmatrix} \mathbf{x_k} \tag{5.19}$$

By converting the LTI state-space to transfer function and summing over the m harmonics, the result falls out.

The multivariable adaptive feedforward controller is equivalent to m parallel internal model controllers with poles of multiplicity n at the disturbance frequencies. The fact that the time-varying adaptive controller has an equivalent LTI representation has the immediate consequence that the controller can be analyzed using LTI techniques. The block diagram suitable for LTI analysis is shown in figure 5.2. The ability to analyze the adaptive controller using the LTI equivalent is especially useful for multivariable systems with more than one frequency in the disturbance.

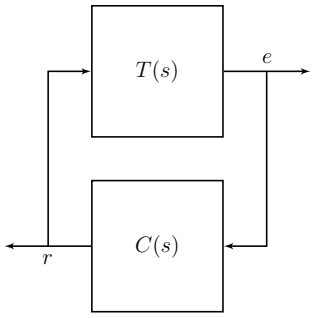

Figure 5.2: Equivalent LTI feedback control system for the adaptive feedforward controller

5.2.1 Stability and Convergence Rate

The most obvious usefulness of the LTI equivalence is to predict the stability of the adaptive controller for various adaption gains. Along the same lines, the convergence rate can also be predicted by evaluating the maximum eigenvalue.

$$\lambda_{conv} = max(Re[\lambda(I_{nxn} + T(s)C(s))^{-1}]) \tag{5.20}$$

The practical usefulness of this is that if the frequency region of the disturbance is known then the LTI control loop can be evaluated for a given adaption gain to ensure stability throughout.

5.2.2 Sensitivity Transfer Functions

Another direct consequence of the LTI equivalence is that traditional sensitivity analysis can be used to evaluate the performance and robustness of the algorithm. By looking at the maximum singular values of the sensitivity function, the frequencies at which e is attenuated or amplified can be determined. Also, the maximum singular value of the complementary sensitivity gives an indication of the robustness of the controller. Again, the range of frequencies can be gridded for varying disturbances and the sensitivity and complementary sensitivity can be analyzed for various adaption gains.

5.3 Implementation Details

Implementation of the controller is done on a processor, so equation 5.11 must be discretized. For the discretization, a simple forward euler approximation, shown in equation 5.21, is used.

$$T_s \begin{bmatrix} \dot{\mathbf{a}}_\mathbf{k} \\ \dot{\mathbf{b}}_\mathbf{k} \end{bmatrix} \approx \begin{bmatrix} \mathbf{a}_\mathbf{k}(t+1) \\ \mathbf{b}_\mathbf{k}(t+1) \end{bmatrix} - \begin{bmatrix} \mathbf{a}_\mathbf{k}(t) \\ \mathbf{b}_\mathbf{k}(t) \end{bmatrix} \tag{5.21}$$

Also, it is assumed the angle is given by an encoder or phase-locked loop which can be used to estimate the angular velocity. For magnetic bearing systems, usually an encoder gives the shaft angle which can be used to synchronize the angle in adaptive algorithm. High-order harmonics can be targeted by multiplying the encoder angle by an integer. Moreover if speed is changing, then adaptive algorithm can be implemented by performing a linear interpolation on the matrix transfer function as shown in equation

$$\begin{aligned} Re[T(j\omega_k)] &\approx \alpha Re[T(j\omega_l)] + (1-\alpha) Re[T(j\omega_{l+1})] \\ Im[T(j\omega_k)] &\approx \alpha Im[T(j\omega_l)] + (1-\alpha) Im[T(j\omega_{l+1})] \end{aligned} \tag{5.22}$$

The transfer function $T(j\omega)$ is gridded at the l nodes by a seperation of δ_ω and stored in a 3-d array, then depending on the speed

$$\alpha = \frac{\omega_{l+1} - \omega_k}{\delta_\omega} \tag{5.23}$$

Obviously the smaller δ_ω the better the interpolation approximates the actual transfer function at the expense of storage. This significantly reduces the implementation cost of the transfer function, especially if the transfer function is multivariable and high order. Lastly, the sine, cosine, and encoder counting can be done on a FPGA which communicates with a processor using FPGA/processor type chips.

5.4 LTI Equivalent Analysis

In this section the LTI equivalence is used to analyze the stability, convergence rate, and robustness of the adaptive feedforward algorithm. Two different cases are analyzed:

1. The standard SISO adaptive feedforward algorthim equation 5.14 and the coupled MIMO adaptive feedforward algorithm equation 5.11.

2. The one frequency algorithm and the two frequency algorithm for the MIMO adaptive feedforward controller

5.4.1 SISO vs MIMO Adaptive Feedforward Algorthm

A first attempt at using an adaptive feedfoward algorithm for unknown narrow band disturbance rejection might be to try the decoupled single input single output version equation 5.14; but, since this method ignores the decoupling between channels it was seen to be unstable. This can be analyzed using the LTI equivalent system as described in 5.2. The analysis in this section was done for the minimization of the control input (u), so the transfer function $T(s)$ was created by using the plant and controller described in Section 5.2.

Figure 5.3 shows the maximum eigenvalue, which corresponds to the convergence rate of the adaptive filter, of the AFC versus the learning gain for various frequencies. The top plot is the MIMO AFC, while the bottom is the SISO AFC. The most striking feature is the SISO algorthim is unstable for all learning gains when attempting to reject frequencies below 100 Hz, while the MIMO AFC is stable for gains less than 300. Also the convergence rate for the MIMO AFC exhibits good convergence rate at throughout the whole frequency range. However, both the MIMO and SISO algorthim have adequate stability and convergence for frequencies above 200 Hz.

The maximum eigenvalue does not give a complete picture of the overall system, since it doesn't caputure the robustness and amplification of other frequencies. Figure 5.4 shows the maximum singular value of the complementary sensitivity transfer function and the sensitivity for a disturbance of 150 Hz at different learning gains. The complementary sensitivity function gives an indication of the robustness of the overall system; it should be small at frequencies where the model is incorrect. From the figure, as the gain increases robustness near the disturbance frequency is compromised. Also, the sensitivity gives an indication of the effect of a disturbance on the output. The figure shows that external

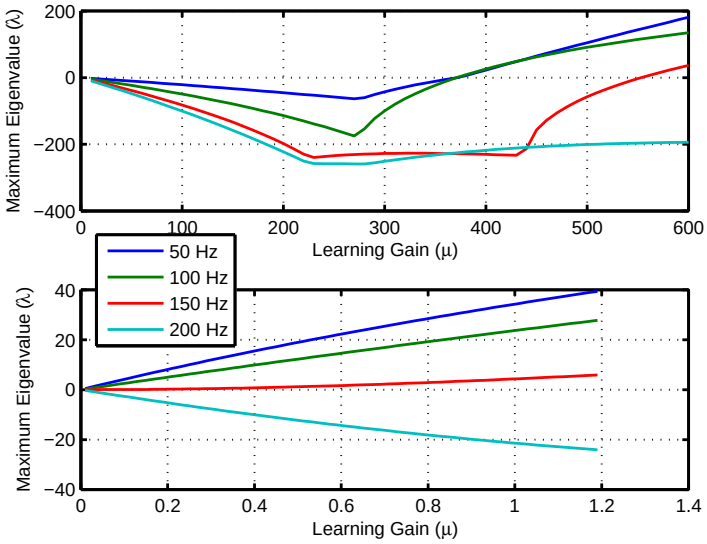

Figure 5.3: Plot of the maximum eigenvalue versus the learning gain for several disturbance frequencies. The top plot is the MIMO AFC algorthm, while the bottom is the standard SISO AFC.

disturbances near the disturbance frequency will be further amplified for increasing learning gains.

Figure 5.5 shows the complementary sensitivity and sensitivity for various disturbance frequencies while holding the learning gain fixed at 100. The MIMO AFC is less robust at lower frequencies for low disturbances but more robust in the high frequency region for the same disturbances. Also, there is more amplification of other frequencies for lower disturbances. These factors depend on the controller and plant, which makes the LTI equivalence useful in analyzing the AFC controllers.

5.4.2 Multiple Frequency Analysis

For a magnetic bearing application, it may be necessary to target harmonics of the spin frequency. The LTI equivalent controller, equation 5.15, can be used to analyze the stability, convergence rate, and robustness for the adaptive system. Once again the goal is to minimize the input control (u), so the appropriate $T(s)$ is chosen, except twice the disturbance

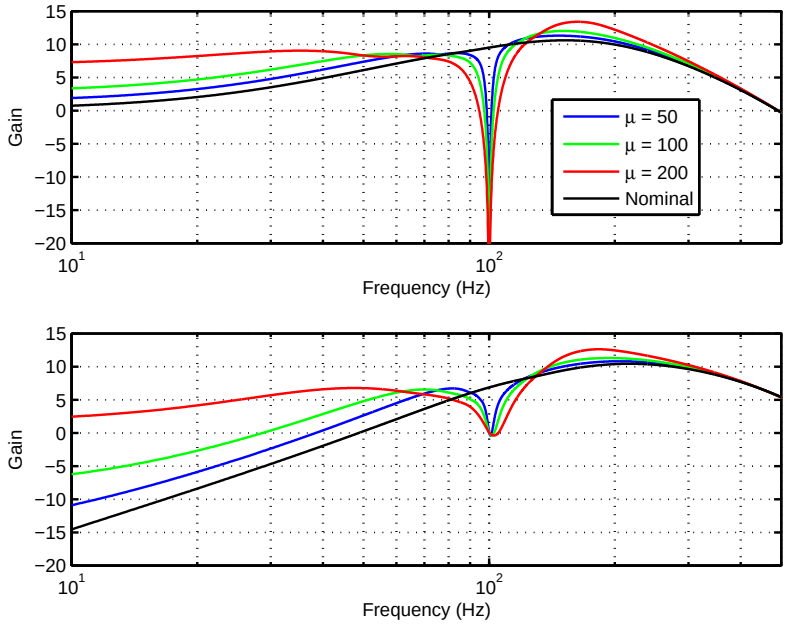

Figure 5.4: The top plot is the maximum singular value of the complementary sensitivity transfer function for various learning gains, while the bottom is the sensitivity. The disturbance frequency is 100 Hz

frequency is targeted as well. In this section, the LTI equivalent system is used to analyze the two frequency algorithm.

Figure 5.6 shows the maximum eigenvalue of the closed-loop system. From the figure, adding an additional internal model narrows the stability margin especially at lower frequencies. Figure 5.7 shows the complementary sensitivity of the overall system when targeting 100 Hz for the single sinusoid case (top plot) and 100/200 Hz for the two frequency case. It is seen that increasing the learning gain not only decreases robustness at all frequencies but can be especially problematic at frequencies in between the desired two. This is even more evident when looking at the sensitivity (Figure 5.8) where for higher learning gains the inter frequency components are amplified.

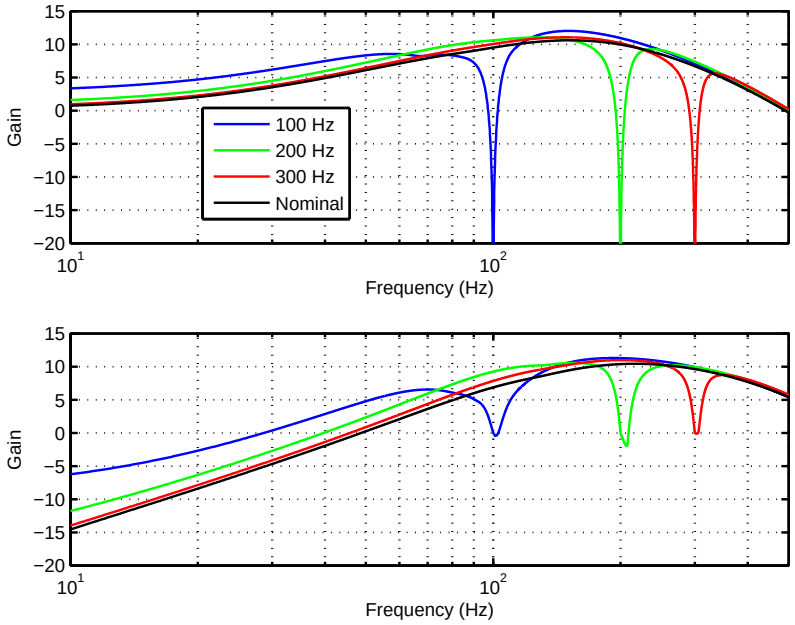

Figure 5.5: The top plot is the maximum singular value of the complementary sensitivity transfer function for various disturbance frequencies, while the bottom is the sensitivity. The learning gain is 100

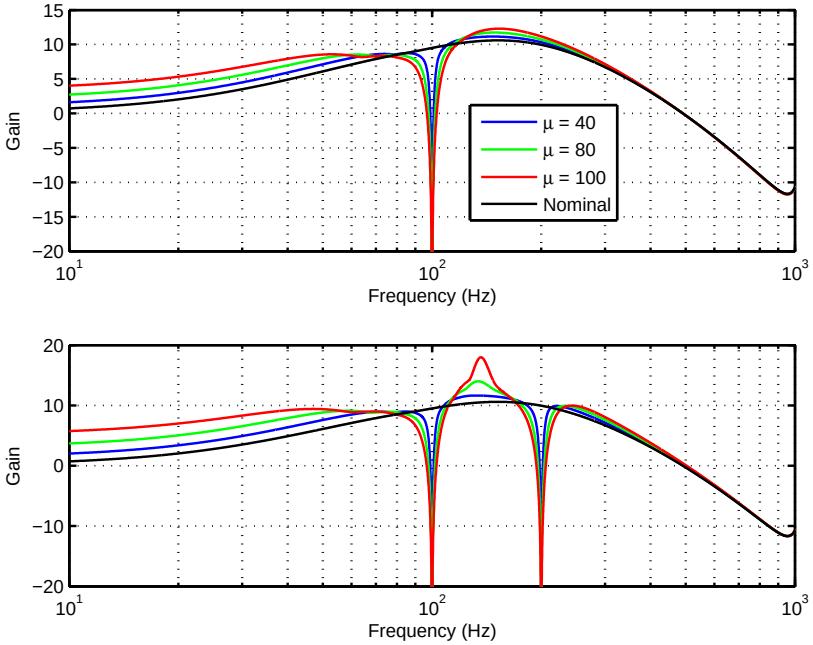

Figure 5.7: The top plot is the maximum singular value of the complementary sensitivity transfer function for a single frequency, while the bottom is the complementary sensitivity for two frequencies at various learning gains and a disturbance frequency of 100 Hz.

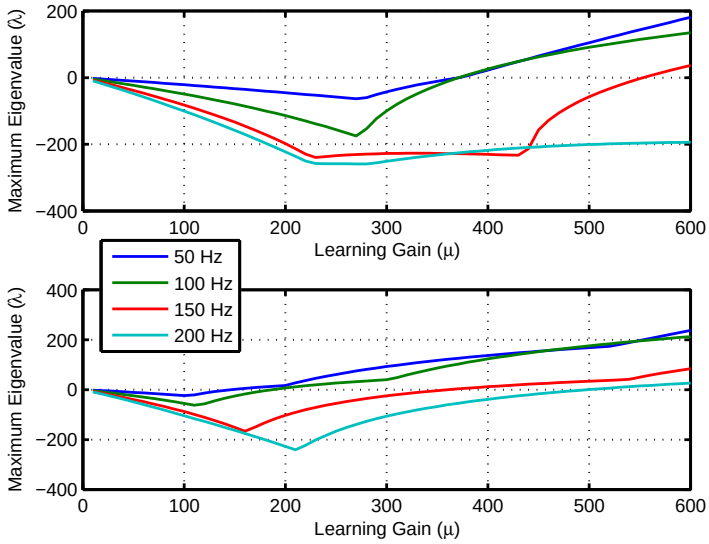

Figure 5.6: The top plot is the maximum eigenvalue value of the overall LTI equivalent system for various disturbance frequencies, while the bottom is the maximum singular value of the overall LTI equivalent system for the same disturbance frequencies and its harmonic.

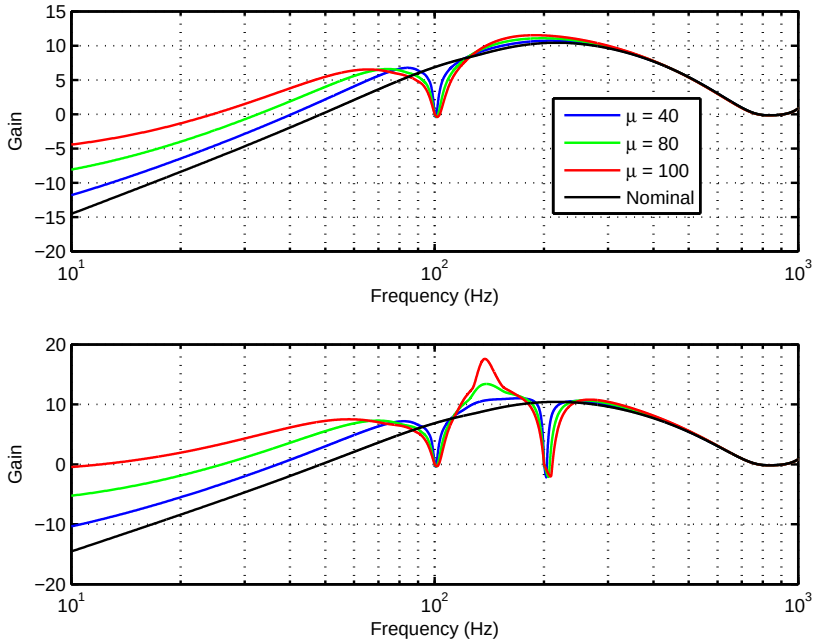

Figure 5.8: The top plot is the maximum singular value of the sensitivity transfer function for a single frequency, while the bottom is the sensitivity for two frequencies at various learning gains.

Based on these observations, the learning gain is chosen based on three criterions

1. Stability of the overall system

2. Adequate convergence rate

3. The sensitivity transfer functions not amplifying unwanted frequency components

5.5 Magnetic Bearing Spin Results

This section presents experimental validation of the multivariable adaptive feedforward controller using LTI design techniques. The controller attempts to minimize the control input and three cases were considered:

1. The control uses the encoder signal to minimize the control input during the transient spin-up stage of the induction motor. Also shown in this section is an external accelerometer used to monitor the housing vibrations.

2. A single frequency adaptive feedforward controller is used to reject the spin frequency at a fixed frequency. The accelerometer was used here to monitor housing vibrations.

3. The spindle was spun at a lower a frequency and a two frequency adaptive feedforward was used to reject the spin frequency and one of its harmonic.

5.5.1 Transient Spin-up Vibration Reduction

From the LTI analysis in section 5.4, standard siso AFC does not work on the test bed because of instability or slow convergence. To highlight the benefits of the MIMO approach, the controller was tested in a transient situation. Namely, the spindle was levitated using the LQGi controller and then spun from stationary to 500 Hz (30,000 RPM). The speed control was done by the internal industrial rexroth three phase motor controller. Figure 5.9 shows the short-time fft of the control signal with the adaptive controller and without it, because of the controller fast transient it is capable of minimizing the control input throughout the varying spin frequency. It is also worth mentioning that the motor spin up is similar to a chirp input disturbance. The adaptive controller is able to bring down the control effort as if it levitating without spinning.

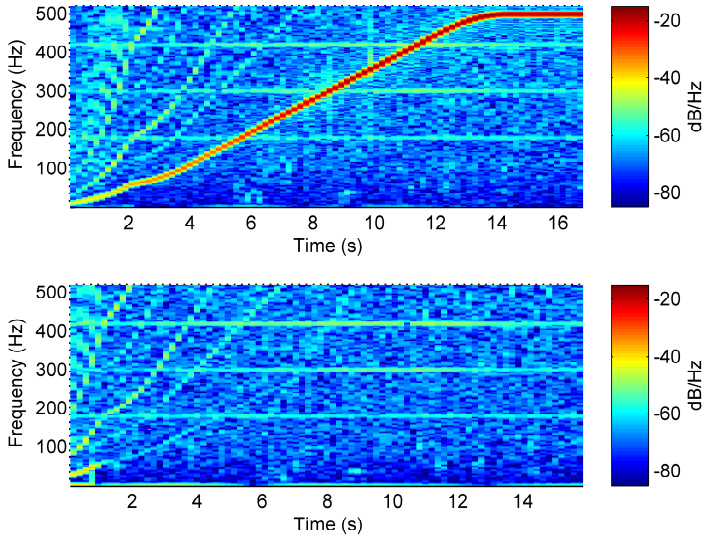

Figure 5.9: Short-time fft plot of the control input for a single channel (others are similar) during a transient spin-up to 500 Hz. The top is without the adaptive controller, while the bottom is with the adaptive controller turned on for a μ value of 20.

Figure 5.10 shows the weights for the first channel adapting during spin-up. Other channels are not shown since they are similar, but there are a total of 8 weight that depend on each other, 2 for each channel. In figure 5.10, top is the weight corresponding to the sine term and bottom is the weight corresponding to the cosine term which determine the phase and gain of the reference signal.

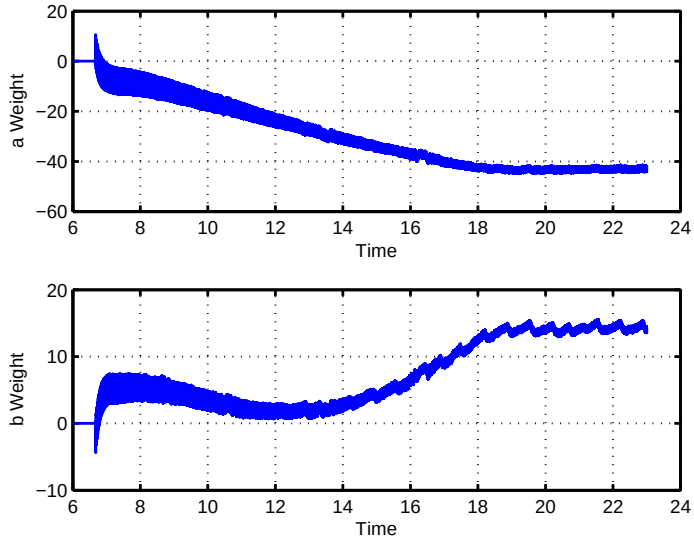

Figure 5.10: The weights for a single channel (others are similar) during the transient spin-up. The top is the weight corresponding to the sine term and bottom is the weight corresponding to the cosine term.

An accelerometer was also mounted on the housing the monitor vibrations. If the control effort is minimized at the spin frequency, then the controller takes no action and is spinning about its inertial axis, or as if it was just purely levitating. In this sense, the AFC is much like placing a notch filter in the control loop to minimize housing vibrations, but with the added benefit that it can adapt to changes in the spin frequency. Figure 5.11 shows the short-time fft of the accelerometer sensor with and without the adaptive controller. The AFC is able to reduce housing vibrations by about 20 dB when compared with just using the LQGi controller alone.

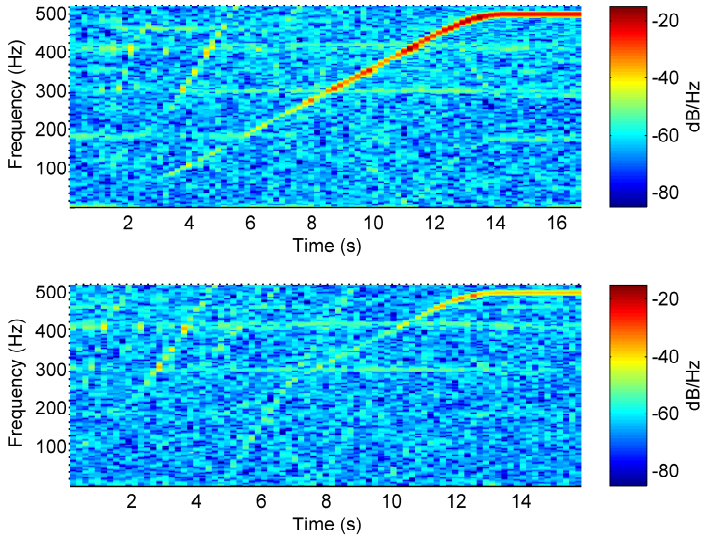

Figure 5.11: Short-time fft plot of the accelerometer mounted on the housing with and without the adaptive controller during the transient.

5.5.2 Steady-State Vibration Reduction

In this section, the spindle is kept at 500 Hz and then steady-state data is collected. This is similar to a constant 500 Hz disturbance. Figure 5.12 shows the power spectral density of the control input under these circumstances. The AFC reduces the control effort by 100 dB at the spin frequency, or it effectively notches out the control effort at that particular frequency. Due to the reduced control effort, the housing vibration also gets attenuated approximately 35 dB (figure 5.13). Also interesting from figure 5.12 is the presence excitation in the control multiples of 60 Hz which creep into the signal. There is content at 180 Hz , 240 Hz, 300 Hz, etc.

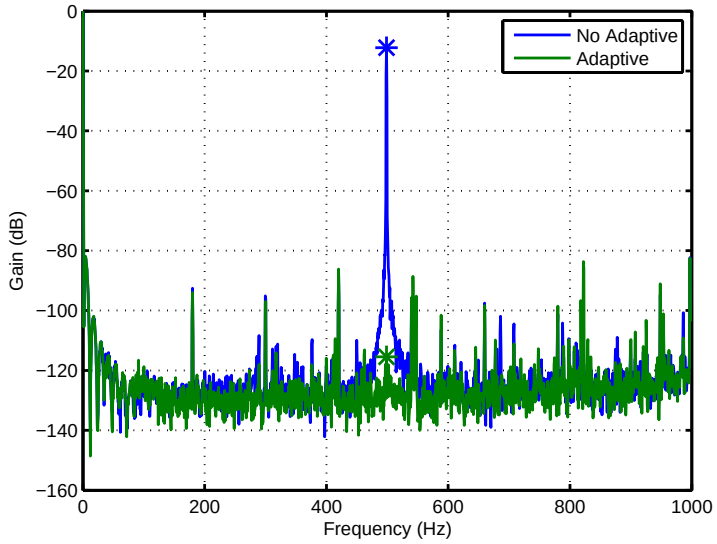

Figure 5.12: Power Spectral Density of the control input for one channel with the spindle spinning at 500 Hz and the controller converged. The blue shows the control input without adaptive and the green with adaptive.

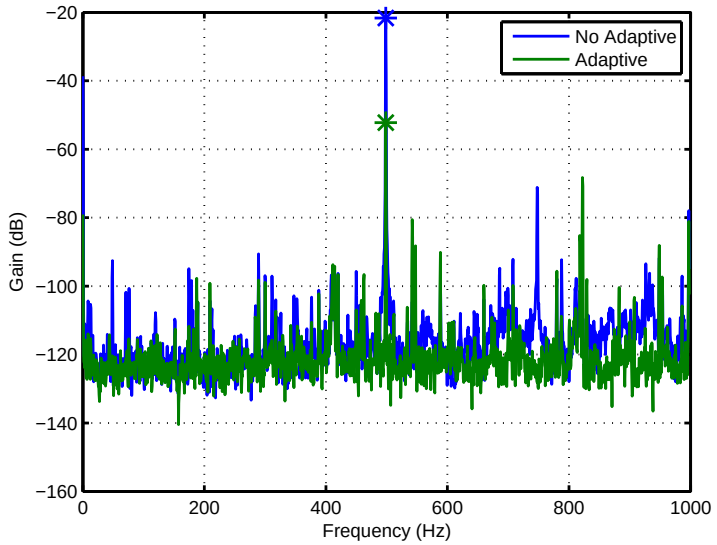

Figure 5.13: Power Spectral Density of the accelerometer mounted on the housing while the spindle is spinning at 500 Hz.The blue shows the control input without adaptive and the green with adaptive.

5.5.3 Two Frequency Control Input Reduction

In the last test, the spindle was spun to 250 Hz and the two frequency AFC was used to reject not only the spin frequency but also a harmonic. Once again the control input was minimized. Figure 5.14 shows the power spectral density of the control input for three cases:

- The blue trace is the spindle spinning with the LQGi controller with the adaptive controller off
- The green trace is the single frequency AFC controller
- The red trace is the double frequency AFC controller

Most striking is the double AFC controller is about to minimize u at the spin frequency (250 Hz) just as well as the single frequency algorithm; but, is also able to completely reject the 500 Hz component. A slight disappoint was the 500 Hz component in the accelerometer reading was not attenuated as expected when using the two frequency algorithm. This is believed to be because the vibrations induced at 2x the spin frequency are not that significant, so there is not much to attenuate.

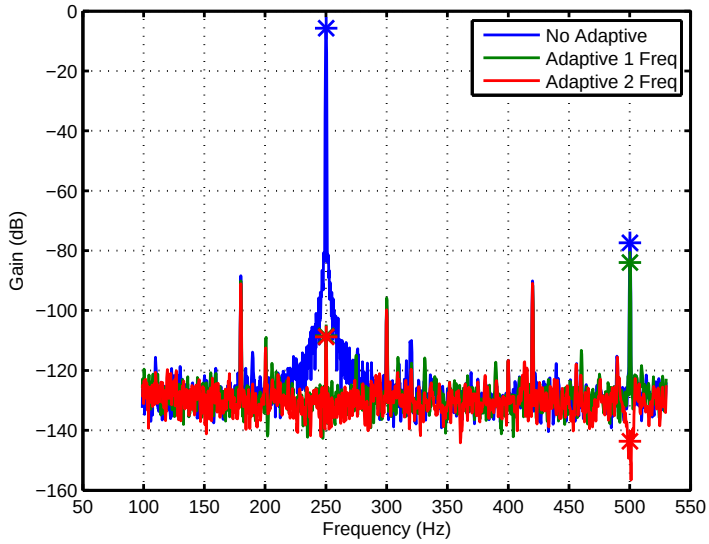

Figure 5.14: Power Spectral Density of the control input for one channel, while the spindle was spinning at 250 Hz. The blue is without the AFC algorthm, the green is the one frequency AFC algorthm, and the red is the two frequency AFC algorthm.

CHAPTER 6

Geometrical Centering of Varying Frequencies

In this chapter, the geometrical centering problem is once again considered; however, with the assumption that there is no encoder measurements available. Essentially, this requires an adaptive frequency estimation algorithm using only the internal signals, and updates of the controller based on the estimation. This type of controller is useful in applications of magnetic bearings where it is desired to geometrically center the spindle while there are unknown narrow band disturbances.

The general problem of compensating for unknown narrow band frequencies has been addressed in literature. In [AKU99],a Youla based internal model for unknown frequencies was applied to an acoustic duct. In this scheme, a FIR Youla parameter was updated by estimating the disturbance using an observer. In [LCR05], the same approach was applied to an active suspension system. In [BD97], an AFC algorithm was used with frequency estimation and another with a phased lock loop. The proposed AFC algorithm with frequency estimation was indirect in that the frequency estimation was decoupled from the updating the control law and not updated at every time step. In the PLL, the controller and phase estimates were updated at every time step.In [MST03], the disturbance was estimated and then fedback to the input for cancellation, known as the disturbance observer (DOB). In [CT12] another DOB scheme, but with robust modification that amounts to using an IIR youla parameter. In [PFX15], the DOB type scheme was applied to a magnetic bearing system, however in SISO manner.

The previous approaches have a few drawbacks that is addressed by the approach used in this thesis. The Youla updates use a FIR approximation to an internal model and need to have a relatively accurate plant model. Using a phased lock loop can be slow and inac-

curate, since there must be phase error for the frequency estimation. Additionally, a PLL is dependant on input amplitude which, as in the magnetic bearing case, can be varying. In DOB schemes accurate estimations of the disturbance is necessary which is difficult across large frequency bands.

The approach in this thesis addresses many of these issues. The error is directly fed into the internal model, so accurate estimation of the disturbance is not necessary. The disturbance is estimated using a closed loop observer, but only for the frequency estimation. Similar to [CT13], an inversion only in the expected frequency band of the disturbance is used for enhanced robustness and ease of implementation. Moreover, the approach is shown to work on the multivariable unstable magnetic bearing system. Lastly, both steady state and transient results for one and two unknown frequencies are presented and compared to using the known frequency version.

6.1 Problem Setup

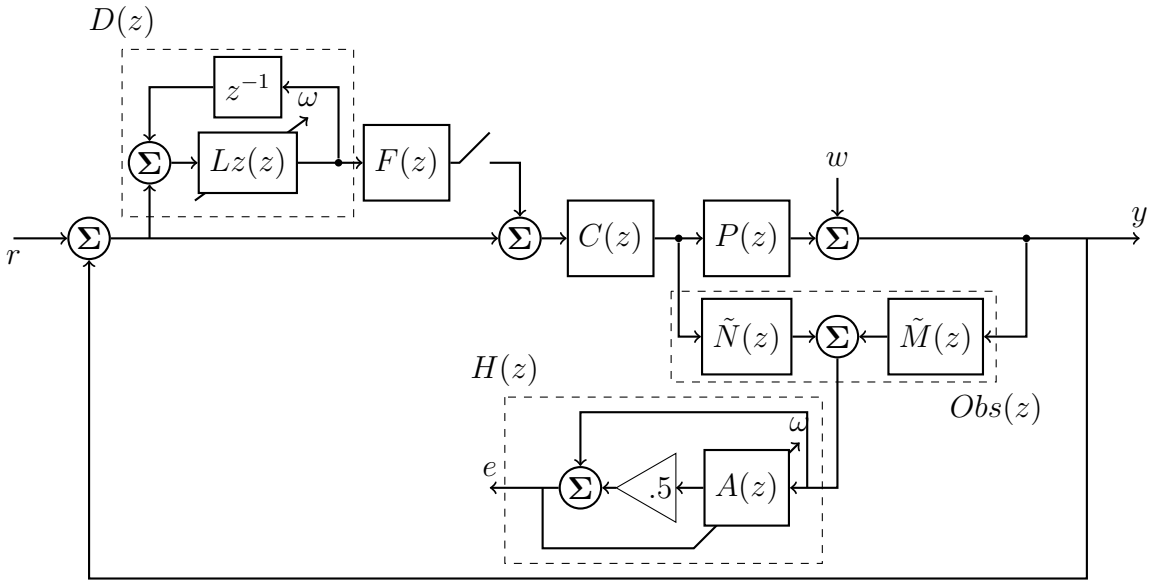

Figure 6.1: Set-up of the unknown sinusoidal disturbance/reference problem

Figure 6.1 shows the overall block diagram for the adaptive control problem. The objective is to reject or track a single or possibly multiple sinusoid frequencies. The added

difficulty is the frequency is assumed to be unknown, so an estimation of the frequency is needed. Moreover, it is also assumed there can be multiple unknown frequencies. Also, the plant $P(z)$ is non-minimum phase, unstable, and multivariable $4x4$. Repetitive control with peak filter modification from the previous chapter is extended to create a time-varying internal model that is capable of handling varying frequencies.

The scheme has 4 major components:

1. the adaptive internal model $D(z)$
2. the inversion filter $F(z)$
3. the disturbance observer $Obs(z)$
4. the frequency estimation $H(z)$

The internal model is responsible for asymptotical error rejection, while the inversion filter ensures stability with some robustness. Also, the observer is used to identify the disturbance frequency for use in the frequency estimation algorithm. The following section will describe in greater detail the four major parts of the approach.

6.1.1 Internal Model

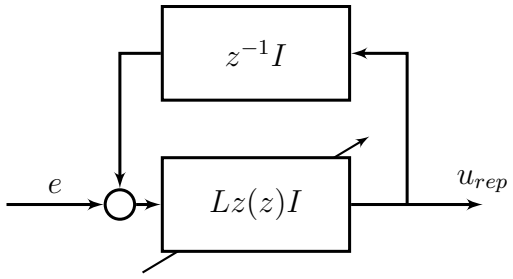

Figure 6.2: The internal model is updated as estimations of the disturbance frequencies is computed.

As in Chapter 3, the goal of the internal model (fig. 6.2) is to have infinite gain at the disturbance frequencies. The filter $L(z)$ is constructed such that it is 1 at the disturbance

frequencies and small elsewhere. The filter is constructed using cascaded notch filters in the following form

$$H_L(z) = \prod_{i=1}^{p} \frac{1 - 2cos(\omega_i)z^{-1} + z^{-2}}{1 - 2\rho cos(\omega_i)z^{-1} + \rho^2 z^{-2}} \tag{6.1}$$

$omega_i$ determines the location of the notch filter while ρ determines the bandwidth of the notch filter. The peak filter can then be constructed as

$$L(z) = 1 - H_L(z) \tag{6.2}$$

It is also important to note, that when using cascaded nothces, the peak filter can also be represented as

$$H_L(z) = \prod_{i=1}^{p} \frac{2(1-\rho)cos(\omega_i)z^{-1} + (\rho^2 - 1)z^{-2}}{1 - 2\rho cos(\omega_i)z^{-1} + \rho^2 z^{-2}} \tag{6.3}$$

Eqn. 6.3 is of relative degree one, therefore it is particularly attractive to provide look aheads for non-casual inversion schemes.

6.1.2 Inversion Filter

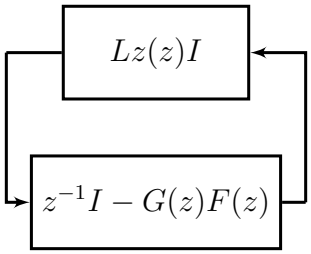

Figure 6.3: Rearrangement of the overall control scheme suitable for small gain, in the adaptive case the filter $L(z)$ is time-varying.

The control diagram can be rearranged into the equivalent block diagram shown in fig 6.3. This is similar to the non-adaptive case in Chapter 3 except the filter $L(z)$ is time varying. Time varying small gain theorem can be used to ensure stability, however it may be too conservative and does not help facilitate inversion filter design. So by assuming the frequency estimates are slowly varying and using frozen values then following stability

condition can be obtained

$$\|(z^{-1}I - F(z)G(z))L(z)\|_\infty < 1 \tag{6.4}$$

Further by restricting the unknown frequencies to be in a certain interval $\omega = \begin{bmatrix}\omega_L & \omega_H\end{bmatrix}$, then the stability condition requires inversion in that band and low gain in others. Specifically,

$$F(z) = \begin{cases} F \approx z^{-1}G^{-1}(z) \text{ if } \omega = \begin{bmatrix}\omega_L & \omega_H\end{bmatrix} \\ F \approx 0 \text{ else} \end{cases} \tag{6.5}$$

This is approximately accomplished by solving the H_∞ model matching problem with appropriate weighting filters as outlined in chapters 3 and 7.

6.1.3 Disturbance Observer

In order to estimate the frequency online, an estimation of the disturbance signal is necessary. Using the control signal or the output is not a robust solution since it is in feedback and these quantities can approach 0. To estimate the disturbance, an observer is designed for the open loop unstable plant using the steady state Kalman filter

$$\hat{x}(k+1) = (A_p - LC_p)\hat{x}(k) + B_p u(k) + Ly(k) \tag{6.6}$$

$$r(k) = -C_p\hat{x}(k) + y(k) \tag{6.7}$$

This can also be represented in transfer function form as

$$r(z) = \tilde{M}(z)y(z) - \tilde{N}(z)u(z) \tag{6.8}$$

where $\tilde{M}(z)$ and $\tilde{N}(z)$ is given as

$$\tilde{M}(z) = C_p(zI - A_p + LC_p)^{-1}L + I \tag{6.9}$$

$$\tilde{N}(z) = C_p(zI - A_p + LC_p)^{-1}B_p \tag{6.10}$$

It is straight forward by writing the error dynamics to obtain the following expression when there is no plant/model mismatch

$$r(z) = \tilde{M}(z)d(z) \tag{6.11}$$

From this equation it it seen the observer gives a filtered representation of the disturbance. Since the only interest is to estimate the frequency of the disturbance, this is suitable as the input to the adaptive frequency estimation scheme outlined next.

6.1.4 Frequency Estimation

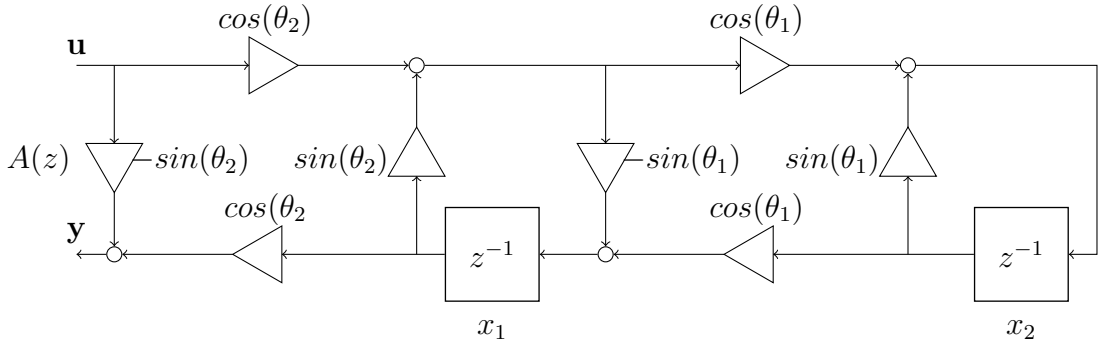

Figure 6.4: Lattice structure for the all pass state,θ_1 controls the location of the notch and is adaptive to minimize the error while θ_1 determines the bandwidth of the notch.

The adaptive frequency estimation algorithm is the one used in [Reg91], and is briefly outlined here. The scheme is based on the normalized lattice version of an all pass filter shown in figure 6.4 whose parameters are adapted based on the following error

$$e(k) = H(z)\tilde{M}(z)d(k) = [\frac{1}{2}(1 + A(z))]\tilde{M}(z)d(k) \tag{6.12}$$

$\tilde{M}(z)d$ is the output of the observer and $H(z)$ is a notch filter based on the all pass normalized lattice. θ_1 determines the location of the notch, while θ_2 determines its bandwidth. For frequency estimation only θ_1 needs to be adjusted and is updated according by the following law

$$\theta_1(k+1) = \theta_1(k) - \mu(k)e(k)x_1(k) \tag{6.13}$$

where x_1 is the output of the delay in the normalized lattice structure. Also the learning gain is normalized so the algorithm is independent of the input signal amplitude

$$\mu(k+1) = \frac{1}{\sum_{k=1}^{n} \lambda^{n-k} x_1^2(k)} \tag{6.14}$$

where λ is a forgetting factor.

An advantage of the algorithm is the estimates are not biased for white noise input components as opposed to direct form parameterizations. Therefore, the frequency estimation will converge to the non-biased solution. Also shown in [Reg91] if the bandwidth is small (narrow notches) then a cascade, as shown in fig 6.5, of filters will give low biased results to estimate multiple frequencies. However, the estimation error will increase when multiple frequencies are close together.

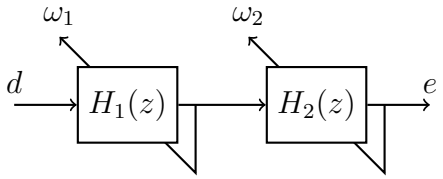

Figure 6.5: Single frequency adaptive frequency estimation algorithm can be cascaded to estimate multiple frequencies provided the bandwidth is small.

6.2 Experimental Results

Experiments to verify the efficiency of the algorithm were performed. The following experiments were conducted:

- During the first experiment, the spindle was spun up to 250 Hz and then spun down, a single internal model was updated to reduce runout.
- The spindle was spun up to 250 Hz and then spun down while a 100 Hz disturbance was injected at the output. An internal model with two frequencies were updated and a cascade of two adaptive algorithms used to estimate both frequencies. This is representative of a time varying disturbance alongside an unknown dominant disturbance.
- The spindle was spun to 125 Hz, while a disturbance at twice the spindle speed was injected. This is representative of the second harmonic of a time varying frequency being excited.

- In the last experiment, the spindle was spun to 250 Hz while a chirp was injected at the output. This is representative of two time varying frequency that may overlap at times.

For all the experiments, the following three controllers were compared:

1. Just LQGi without any internal model as a reference
2. The add-on peak filter with speed estimates from the encoder during spinning and reference speed if injected at the output. This is a best case as the speed is known and only the internal model is updated so there is no feedback from the adaptive frequency estimation.
3. The add-on peak filter with frequency estimates from the adaptive algorithm

This section begins with a discussion of the tuning parameters for the controller. Then experimental results are presented for the 4 experiments described.

6.2.1 Tuning

There are three major tuning parameters in the controller. First, the forgetting factor for the adaptive frequency estimation which mainly determines the transient response of the frequency estimation. Obviously a faster transient response is desired but comes at the expense of larger variations in the estimate. Also, the bandwidth of the notch for the adaptive estimation is important as it determines the resolution of the frequency estimates, a small bandwidth is desired but too narrow may cause convergence issues especially in a noisy environment. Lastly, the bandwidth of the internal model is very crucial because if it is too narrow then error in the frequency estimation can cause instability because of large transients. On the other hand, if it is too wide then it may not be able to properly attenuate the disturbances.

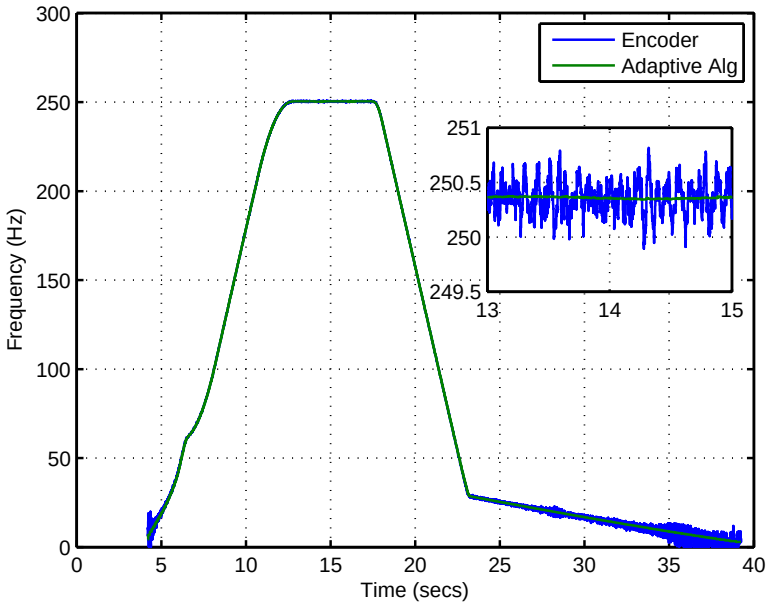

Figure 6.6: The frequency estimates during spin up and down from both the adaptive algorithm and from the encoder.

6.2.2 Spin up with Single Frequency Internal Model

In the first experiment, the spindle was spun was up to 250 Hz and the internal model was updated using both encoder speed estimates and from the adaptive algorithm. Figure 6.6 shows the estimates during spin up and down. From the zoomed in plot the frequency estimation is unbiased with a variance of .5 Hz. Also apparent is the adaptive estimates deteriorate in the very low frequency region since not enough cycles are present for the algorithm. Note also that around 23 seconds the motor driver switches from actively braking during spin down to coasting so a smaller change in frequency occurs after that time.

Figure 6.7 shows the output position of each of the four axis during the spin up and down for the three control strategies. The LQGi controller has the largest amount of error since it is not designed for narrow band rejection. The internal model updates using the encoder reduces the error to near levitation levels and is the best case. The adaptive updates perform just as well as using the encoder, this observation is further quantified in table 6.1 which gives the rms value of the error plot for all three controllers.

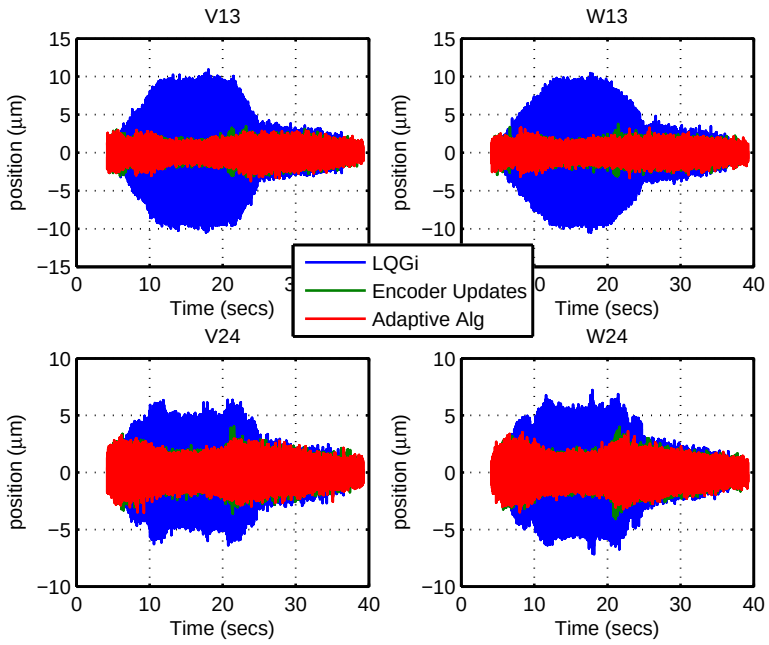

Figure 6.7: Time domain of the output of each of the four axis for the three controllers. The adaptive estimation performs just as well as encoder speed estimates

Figure 6.8 shows the sum of spectrogram of the outputs of each axis. Most important is both internal model approaches are able to reduce the error due to the spin frequency by 20 db while leaving the other unaffected. Interestingly, during coasting, many harmonics of the spin frequency are visible. During spin up, the third harmonic is mainly excited. The mains third harmonic is also present in the output, while there is also a broadband low frequency component.

Channel	RMSe[1]	RMSe[2]	RMSe[3]
V13	4.1	.73	.73
W13	3.9	.66	.66
V24	2.2	.75	.75
W24	2.3	.79	.78

Table 6.1: RMS error for single frequency adaptive during spin up and down with (1)just LQGi, (2) Updating using encoder,(3) updating using adaptive estimation. All units are μm.

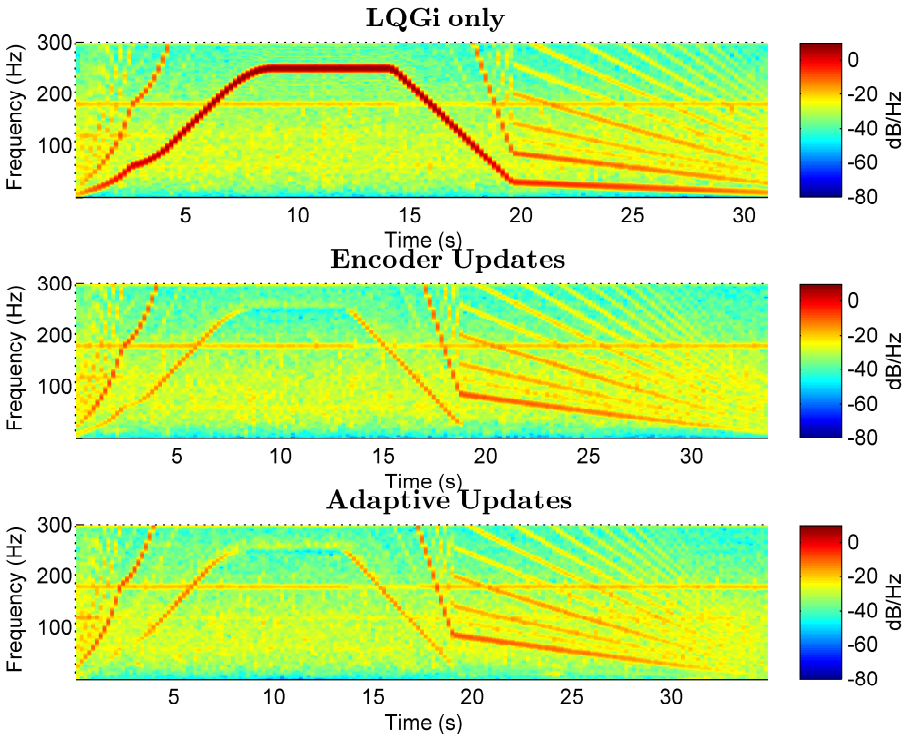

Figure 6.8: Spectrogram of the output error during the spin up and down.

6.2.3 Spin up and Constant Frequency with Two Internal Model

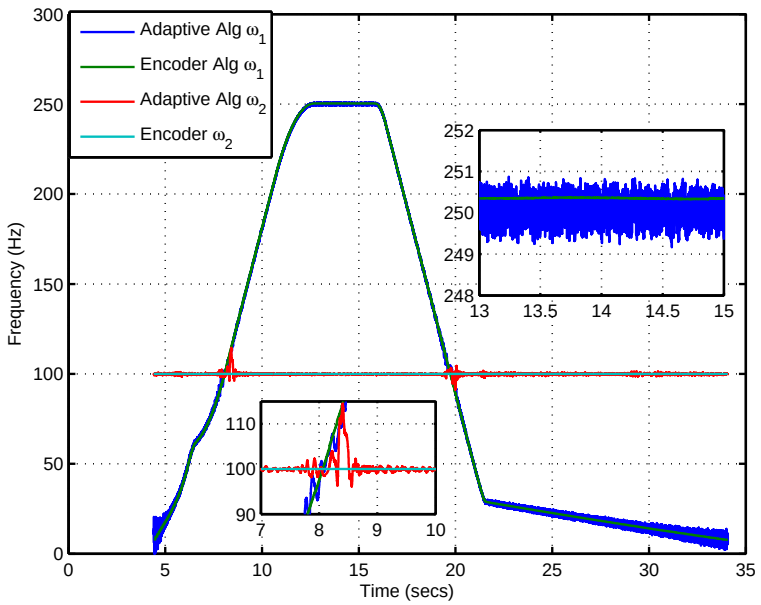

Figure 6.9: The frequency estimates during spin up and down from both the adaptive algorithm and from the encoder/injection reference. Zoomed in plot for the crossover region is also shown.

In this experiment, the spindle was spun up to 250 Hz and then down while a 100 Hz disturbance was injected at the output. Figure 6.9 shows the frequency estimation for both the encoder and adaptive. Two cascaded adaptive frequency estimation algorithms were used. From the figure, it is apparent the estimation of the spin frequency is biased but still less than 1 Hz error. To compensate for this mismatch, the internal model must be widened. Also, during the cross over at 100 Hz, larger errors in the estimation of both frequencies occur which can result in instability if the internal models is too aggressive because of the large transients induced.

Figure 6.10 shows the output during the experiments for all four axis. The adaptive estimate performs just as well as the encoder updates except in the cross over region. Table 6.2 further validate this observation. The rms error for the adaptive updates is slightly larger than the encoder updates but still less than $1\mu m$ of error. It is also interesting to note that

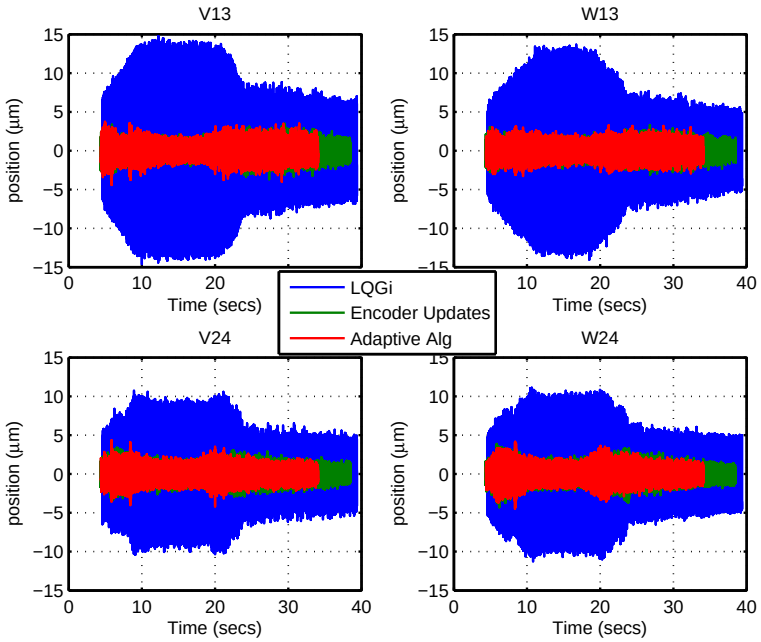

Figure 6.10: Time domain of the output of each of the four axis for the three controllers. The adaptive estimation performs just as well as encoder speed estimates

the encoder update error is the same as the single frequency case.

Figure 6.11 shows the sum of spectrogram of the output errors. Both the adaptive and encoder updates provide 20 dB of attenuation when compared to only LQGi. However, the error during the cross over region is larger when using adaptive updates.

Channel	RMSe[1]	RMSe[2]	RMSe[3]
V13	5.4	.74	.84
W13	4.7	.66	.75
V24	3.7	.75	.78
W24	3.9	.81	.85

Table 6.2: RMS error for 2 frequency disturbance with one constant adaptive during spin up and down with (1)just LQGi, (2) Updating using encoder,(3) updating using adaptive estimation. All units are μm.

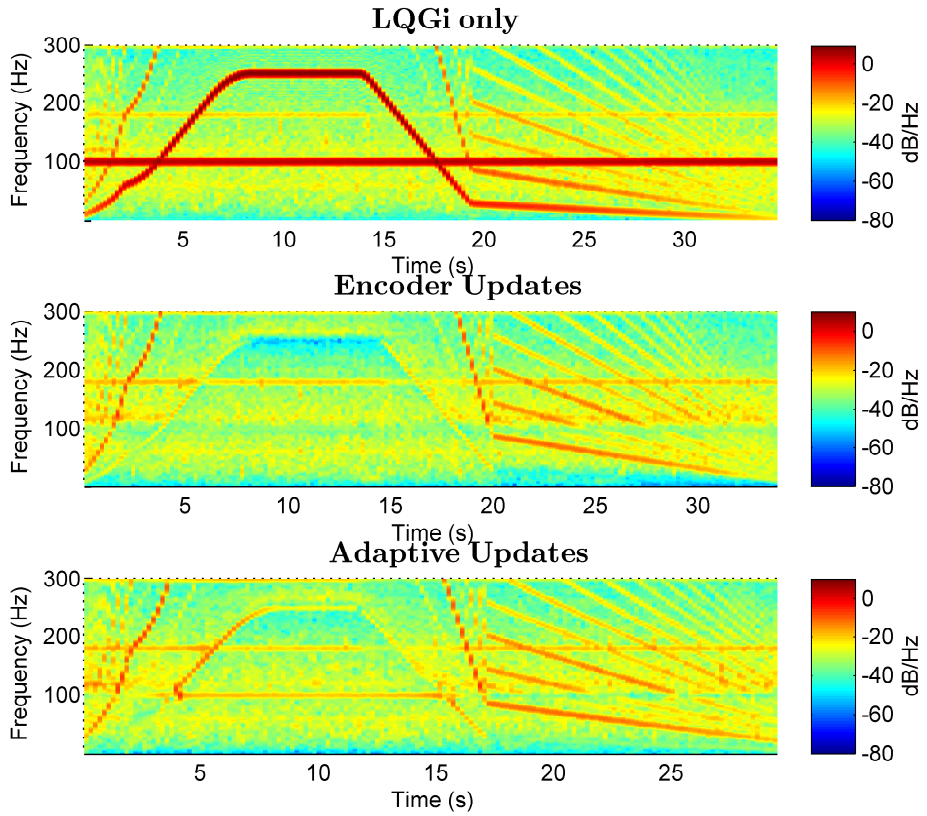

Figure 6.11: Spectrogram of the output error during the spin up and down. The adaptive algorithm has larger error during the crossover region when compared to encoder updates.

6.2.4 Spin up and Double Frequency with Two Internal Model

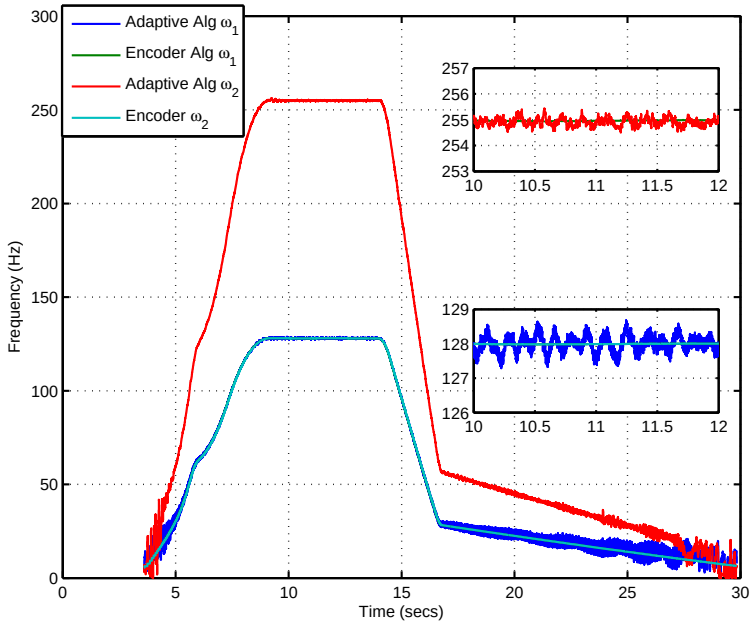

Figure 6.12: The frequency estimates during spin up and down from both the adaptive algorithm and from the encoder and injection reference. The injected frequency is twice that of the spin frequency

In this experiment, the spindle was spun to 125 Hz while a disturbance was also injected at twice the spin frequency. This type of situation is when the 2^{nd} harmonic is excited and the fundamental is unknown. Figure 6.12 shows the estimation of these two frequencies using the adaptive algorithm and the encoder/ reference injection. In this case both frequencies were estimated with .5 Hz of error. Since the frequencies do not cross, there are not any obvious issues using the cascaded structure.

Figure 6.13 show the output of each of the axis for all three control strategies. Both internal models approaches behave similarly and this is verified by table 6.3 which gives the rms the output error during the experiment.

Figure 6.14 shows the sum of the spectrogram during the experiment. Both internal model schemes have a similar error spectrogram throughout the experiment.

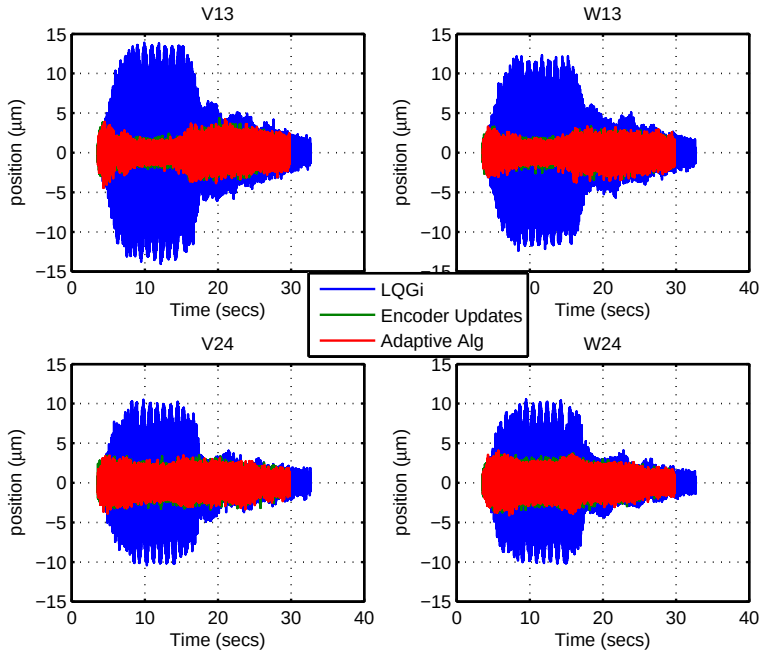

Figure 6.13: Time domain of the output of each of the four axis for the three control. The adaptive estimation performs just as well as encoder speed estimates

Channel	**RMSe**^{1}	**RMSe**^{2}	**RMSe**^{3}
V13	4.2	.88	.91
W13	3.5	.75	.79
V24	2.8	.95	.93
W24	2.9	1.0	1.0

Table 6.3: RMS error for 2 frequency during spin up and down with the other at twice the spin frequency for (1)just LQGi, (2) Updating using encoder,(3) updating using adaptive estimation. All units are μm.

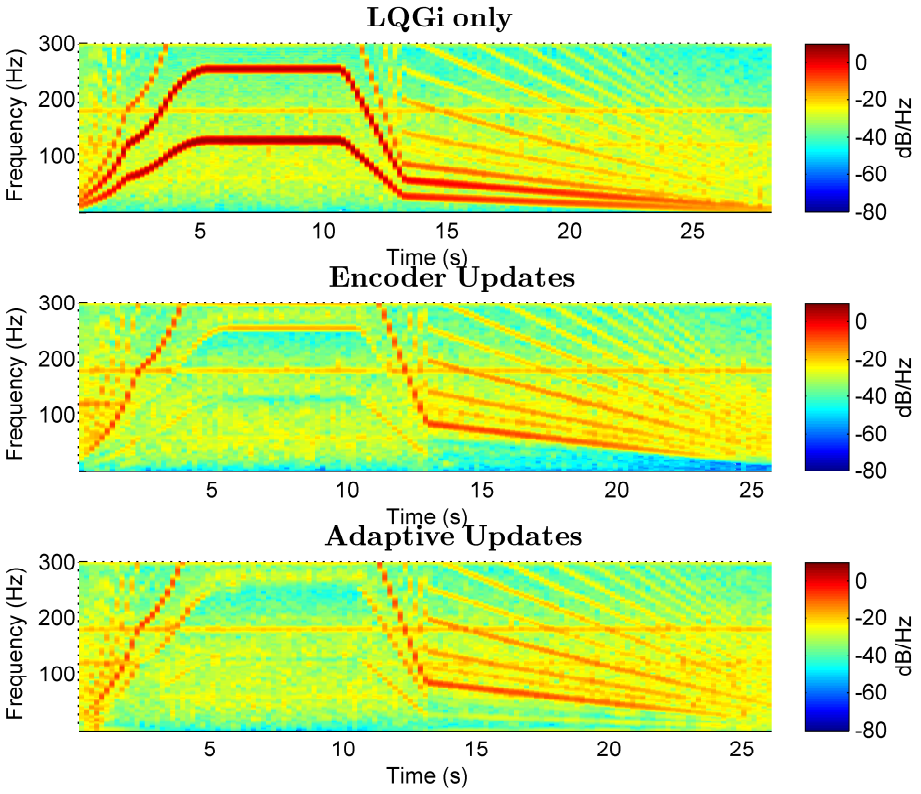

Figure 6.14: Spectrogram of the output error during the spin up and down.

6.2.5 Spin up and Ramp with Two Internal Model

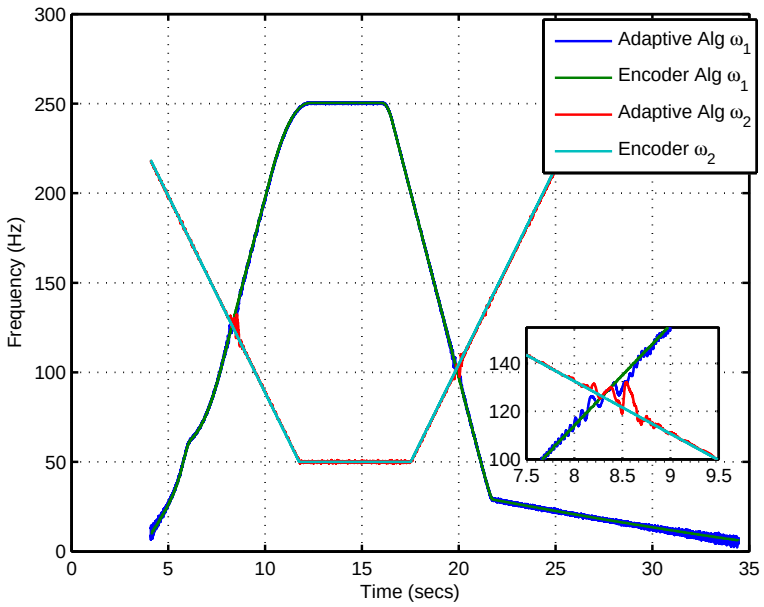

Figure 6.15: The frequency estimates during spin up and down from both the adaptive algorithm and from the encoder and injection reference. An opposite chirp was injected, making sure they cross at some point

In the final experiment, the spindle was spun up to 250 Hz and then back down while an opposite chirp was also injected at the output. In this situation, the controller must compensate for two time varying disturbances that also cross. Figure 6.15 shows the frequency estimation of the two signals. Large estimation errors, seen in the zoomed in plot, occur in the cross over region that must be accounted for by designing a less aggressive internal model. Overall, the cascade adaptive structure is able to track two unknown narrow band signals.

Figure 6.16 show the error during experiments, while table 6.4 show the rms error. The adaptive frequency updates have slightly (.5 μm max) increased rms error when compared to encoder updates.

Figure 6.17 shows the sum of the spectrogram during the experiment. Both internal model schemes have a similar error spectrogram throughout the experiment, with the exception of

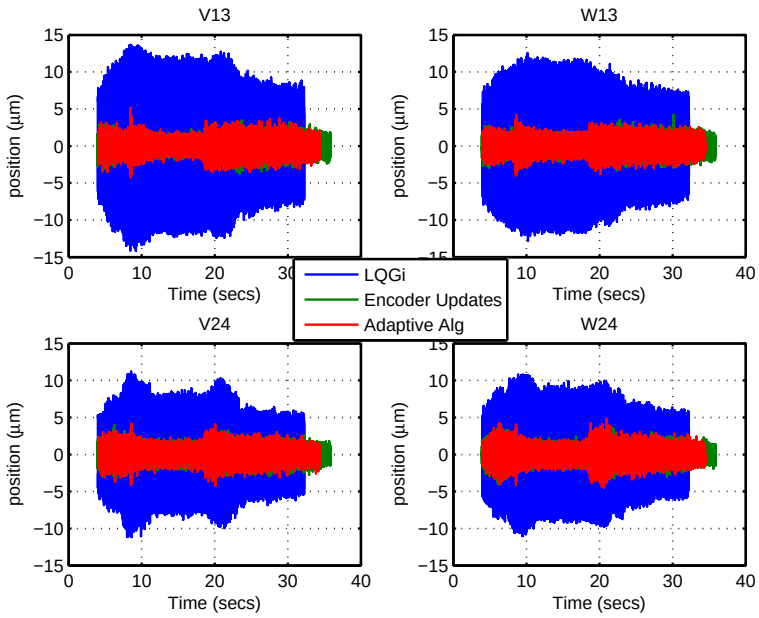

Figure 6.16: Time domain of the output of each of the four axis for the three controllers. The adaptive estimation performs just as well as encoder speed estimates

the cross over region. Here, the increased error when using the adaptive frequency estimation is seen to be 10 dB higher than using encoder speed updates.

Channel	RMSe[1]	RMSe[2]	RMSe[3]
V13	5.5	.76	.81
W13	5.1	.69	.75
V24	3.8	.78	.80
W24	4.2	.83	.87

Table 6.4: RMS error for 2 frequency with one constant adaptive during spin with (1)just LQGi, (2) Updating using encoder,(3) updating using adaptive estimation. All units are μm.

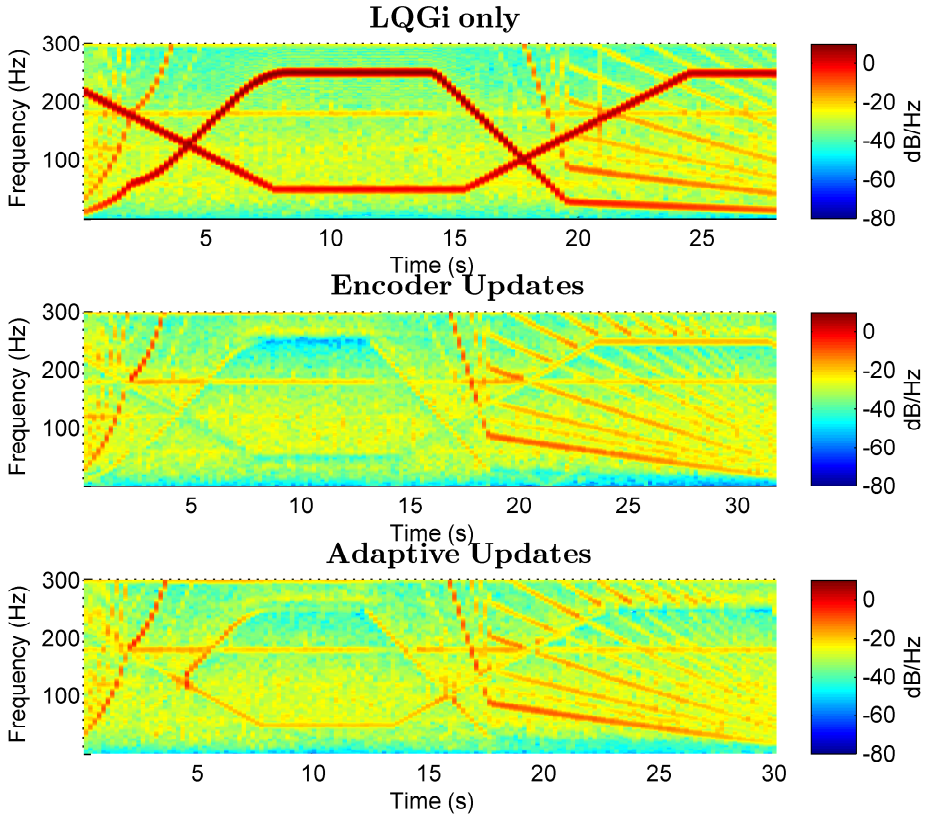

Figure 6.17: Spectrogram of the output error during the spin up and down. The adaptive algorithm has larger error in the crossover region.

CHAPTER 7

Unknown Multivariable Narrow and Broadband Disturbance Rejection

7.1 Introduction

In this chapter, the assumption that the disturbances are sinusoidal is dropped and stochastic or broadband disturbances are also taken into account. Furthermore, the disturbance is also assumed to be unknown, although the plant is known, so an adaptive algorithm is necessary. Once again, the geometrical centering problem is considered so the control scheme minimizes the output variance. On a big picture, the disturbance model needs to identified and the controller adjusted based on that model.

The control strategy is based on the adaptive inverse controller which has been used widely in applications [WW08] . Usually the disturbance model is identified by an LMS algorithm, which suffers from the drawback of slow convergence. In [HL95],RLS updates were first used for Hard Disk Drives, the overall control scheme was expanded to include adaptive plant and disturbance model identification in [TMM12]. The algorithm is known to suffer from high control effort, so in [PTG10] it was extended to include high pass weighting filter for robustness. Additionally, it has also been extended to include internal models into the adaptive controller [WCT09] for enhanced rejection when there are periodic disturbances also present. In [CKB00], a similar adaptive algorithm was done on a siso white box magnetic bearing but with no experimental results.

The main drawback of the approaches stated above is they are essentially siso formulations. First introduced in [TGV13] and later in [TGT16] for laser beam jitter mitigation, a

receding horizon adaptive using rls updates made no assumption about the number of inputs or outputs. The scheme used high pass weighting for robustness but was only applied on single variable system.

In this work, the receding horizon control and another algorithm based upon a decoupling approach is used to compensate for unknown disturbances. Experimental results show the efficiency of both approaches for time-varying and stochastic disturbances. Both methods are shown to work for the flexible AMBS. Furthermore, similarities and differences are highlighted where appropriate.

7.2 Problem Setup

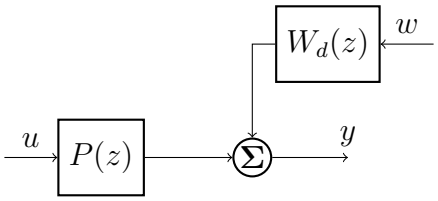

Figure 7.1: Set-up of the unknown disturbance problem

Figure 7.1 shows the set-up for the adaptive control problem. The objective is to find a control input u such that the disturbance in the output y is minimized. If the disturbance was known and the plant was invertible then the control $u = P^{-1}(z)d$ would exactly cancel the disturbance. Many plants, such as the magnetic bearing considered in this dissertation, are non-minimum phase and unstable so a naive inversion technique is not possible. Also, the assumption that the disturbance is known is usually not a realistic one.

A particulary attractive solution is based on the internal model controller and shown in Figure 7.2. A feedback controller $C(z)$ is used to stabilize the plant and provide nominal performance. The disturbance w is estimated using an open-loop observer, $\hat{w} = G(z) - \hat{G}(z)$ where $\hat{G}(z) = \frac{P(z)C(z)}{1+P(z)C(z)}$. The estimated disturbance $\hat{w}$ is then used in the adaptive inverse control formulation to find a FIR filter $Q(z)$ which implicitly identifies the disturbance model. The adaptive filter can be updated using LMS or RLS type adaption algorithms.

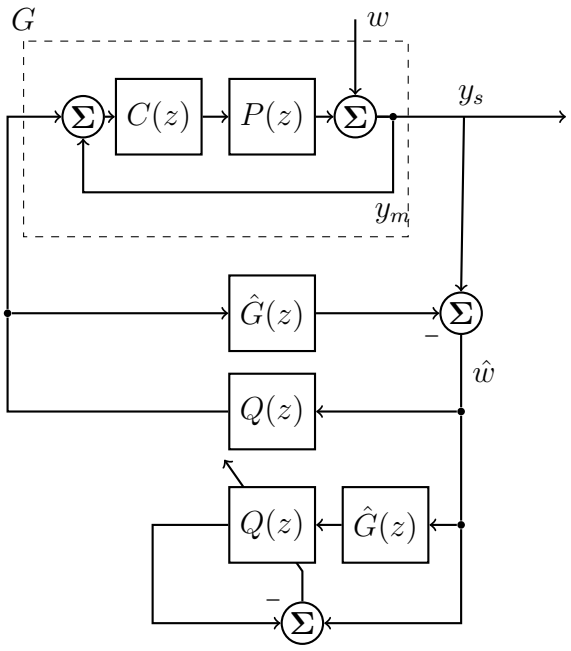

Figure 7.2: The SISO adaptive disturbance rejection control

For the magnetic bearing system under consideration, this SISO type adaptive algorithm cannot be used. The main difficulty comes from the fact that matrices do not commute. In particular,

$$Q(z)\hat{G}(z) \neq \hat{G}(z)Q(z) \tag{7.1}$$

so if there is coupling between the inputs and outputs of a system then the traditional Adaptive Inverse disturbance rejection scheme will not work.

7.3 Receding Horizon Adaptive Control

The finite horizon linear quadratic adaptive controller considers a linear plant with output disturbance given by eqn. 7.2

$$\begin{aligned} x_{k+1} &= Ax_k + Bu_k \\ e_k &= Cx_k + w_k \end{aligned} \tag{7.2}$$

The system matrices are assumed to be known, by an initial system identification exper-

iment. The output disturbance is, however, assumed to be unknown. The objective of the adaptive controller is to find the optimal input u_k that minimize the following cost (eqn. 7.3).

$$J = (\sum_{k=1}^{h} e_k^T e_k + u_k^T R u_k) + x_h^T Q_f x_h \tag{7.3}$$

The first term in the cost minimizes the effect of the output disturbance on the output and the second term punishes the input so that it does not have high gain. The last term, the terminal cost, assures stability of the optimal control sequence.

Indeed the optimal control problem given by eqn, 7.2 and 7.3 is the finite horizon linear quadratic tracking problem, whose solution is known to be a linear feedback control law given by eqn 7.4.

$$u_k = -K_x x_k - K_w \mathbf{w} \tag{7.4}$$

Since the states are not measurable an open loop observer is used and the optimal control law is input into the plant to give

$$\begin{aligned} x_{k+1} &= (A - BK_x)x_k - BK_w \mathbf{w} \\ u_k &= -K_x x_k - K_w \mathbf{w} \end{aligned} \tag{7.5}$$

The controller now consists of two parts: 1) The portion, which along with the open loop observer, contributed by state feedback 2) The portion due to the h future values of the disturbance. Figure 7.3 shows a block diagram of the optimal controller.

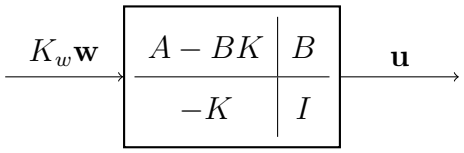

Figure 7.3: The $U(z)$ system of the controller, where the state-feedback portion is embedded in the open-loop observer and the portion due to the future disturbance value are an input to the system

7.3.1 Computing Optimal Gains

Expanding eqn. 7.2, the error sequence can be written as

$$\mathbf{e} = O_x x_k + H_x \mathbf{u} + \mathbf{w} \tag{7.6}$$

where

$$\mathbf{e} = \begin{bmatrix} e_{k+1} \\ e_{k+2} \\ \vdots \\ e_{k+h} \end{bmatrix} \tag{7.7}$$

and the sequences $\mathbf{u}$ and $\mathbf{w}$ are defined similarly. The matrices O_x and H_x are given by

$$O_x = \begin{bmatrix} C \\ CA \\ \vdots \\ CA^h \end{bmatrix} \tag{7.8}$$

$$H_x = \begin{bmatrix} CB & 0 & \dots & 0 \\ CAB & CB & \dots & 0 \\ \vdots & \vdots & \vdots & \vdots \\ CA^{h-1}B & CA^{h-2}B & \dots & CB \end{bmatrix} \tag{7.9}$$

The terminal cost can also be propagated, the following relationships can be verified

$$Q_f^{\frac{1}{2}} x_h = Q_f^{\frac{1}{2}} A^h x_k + H_f \mathbf{u} \tag{7.10}$$

$$H_f = \begin{bmatrix} CA^{h-1}B & CA^{h-2}B & \dots & CB \end{bmatrix} \tag{7.11}$$

The overall cost can then be given by

$$J = \mathbf{e^T e} + \mathbf{u^T} diag(R)\mathbf{u} + x_h^T Q_f x_h \tag{7.12}$$

Then the optimal control sequence can be found by taking the derivative and setting it 0.

$$\frac{dJ}{du} = \frac{de^T}{du}e + diag(R)u + \frac{dx_h^T}{du}x_h \tag{7.13}$$

Finally, the optimal control input is given by

$$\mathbf{u} = (H_x^T H_x + H_f^T H_f)^- 1[(H_x^T O_x + H_f^T A^h)x_k + H_x^T \mathbf{w}] \tag{7.14}$$

This is the desired state-feedback control law and the optimal gains of the unknown disturbance input.

7.3.2 Adaptive Prediction

The control law is non-casual since it depends on future disturbances which is not known. To overcome this an adaptive prediction filter for the control $K_w\mathbf{w}$ is used. To set this up, note that

$$K_w\mathbf{w} = z^h K_w \mathbf{w_p} \tag{7.15}$$

Now, $F(z) = K_w\mathbf{w_p}$ is casual FIR filter and the prediction error can be defined as

$$e = Q(z)z^{-h} - F(z) \tag{7.16}$$

Then the $Q(z)$ can be adapted such that the prediction error is minimized. So the adaptive filter attempts to predict the non-causal control law by using the past data. The overall receding horizon controller is shown in figure 7.4

7.3.3 Multichannel Lattice RLS

In using the receding horizon adaptive controller for multivariable systems, a multichannel adaptive fir scheme is needed; instead of the typical single input single output. The set-up is similar single variable FIR adaption except the regressors can have multiple components. If the input $\mathbf{x}$ is defined as

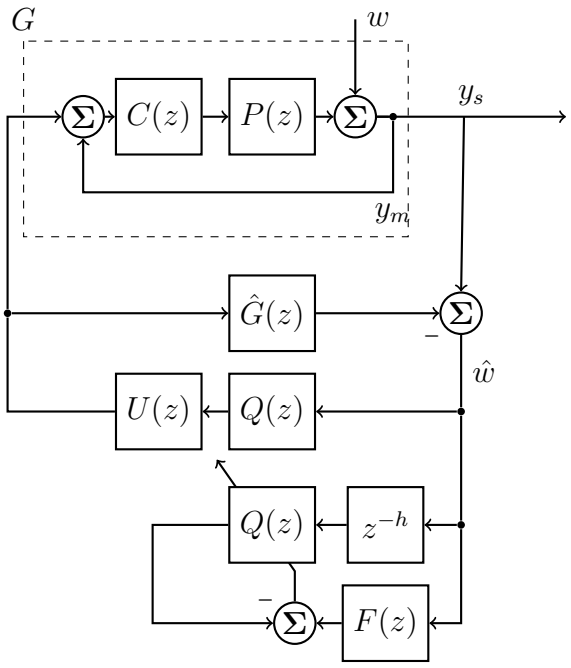

Figure 7.4: The overall Receding Horizon Adaptive Control consisting of an observer for w and adaptive prediction for the non-causal part

$$\mathbf{x}(t) = \begin{bmatrix} x_1(t) & x_2(t) & ... & x_m(t) \end{bmatrix} \tag{7.17}$$

where m is the number of inputs, for the magnetic bearing system $m = 4$. Similarly, the outputs

$$\mathbf{y}(t) = \begin{bmatrix} y_1(t) & y_2(t) & ... & y_m(t) \end{bmatrix} \tag{7.18}$$

Although both the inputs and outputs do not need to have the same dimensions, we assume they do since this is the case for the magnetic bearing system. The regressors are FIR and composed of N delayed versions of the inputs

$$X(t) = \begin{bmatrix} \mathbf{x}(t) & \mathbf{x}(t-1) & \mathbf{x}(t-2) \ ... \ \mathbf{x}(t-N) \end{bmatrix} \tag{7.19}$$

Then the the goal is find the weights W such that the following error is minimized

$$\mathbf{e}(t) = \mathbf{y}(t) - X(t)W \tag{7.20}$$

The weights are a Nxm matrix. In multichannel adaptive filtering, these weights are adjusted online such that the error is minimized.

RLS adaption is attractive because of its rapid convergence when compared to LMS algorithms. In RLS adaption, the following cost function is considered

$$J = \sum_{t=1}^{n} \lambda^{t-n} \mathbf{e}^T(t)\mathbf{e}(t) \tag{7.21}$$

The standard RLS algorithm based on the matrix inversion lemma can be used to update the weights; but it is well known that this algorithm is numerically unstable which can cause the algorithm to diverge in certain applications. The QR algorithm is more numerically robust than the traditional RLS. Eqn. 7.22 briefly describes the Givens QR algorithm.

$$Q(\theta) \begin{bmatrix} R(t-1) \\ \mathbf{x}(t) \end{bmatrix} W = \begin{bmatrix} R(t) \\ \mathbf{0} \end{bmatrix} W = Q(\theta) \begin{bmatrix} \mathbf{y_q}(t-1) \\ \mathbf{y}(t) \end{bmatrix} = \begin{bmatrix} \mathbf{y_q}(t) \\ \mathbf{e_q}(t) \end{bmatrix} \tag{7.22}$$

At each instant of time, a series of givens rotations are used to annihilate the incoming regressors to form a triangular matrix R. The same series of rotations are also applied to the output sequence $y(t)$ and the previous rotated output sequence $y_q(t-1)$ to form the new rotated sequence $y_q(t)$ and the rotated error $e_q(t)$. In some applications, only the error is of concern and this completes the algorithm. However, if the weights are explicitly necessary as would be the case for adaptive control applications, then an additional backsolve step is necessary.

$$W = R(t)^{-1}\mathbf{y_q}(\mathbf{t}) \tag{7.23}$$

Figure 7.5 describes the QR algorithm pictorially.

If the rotation angles are given, then they can be used to rotate the incoming output data into the error. The hybrid QR and lattice algorithm find these angles by taking advantage of the shift structure of the input data sequence, instead of computing explicit givens rotations. Figure 7.6 gives the overall structure of the lattice algorithm. The key idea is that a QR algorithm parameters can be shown to be equivalent to a normalized lattice. Moreover, the reflection coefficients can be obtained from the forward prediction problem; while, the QR

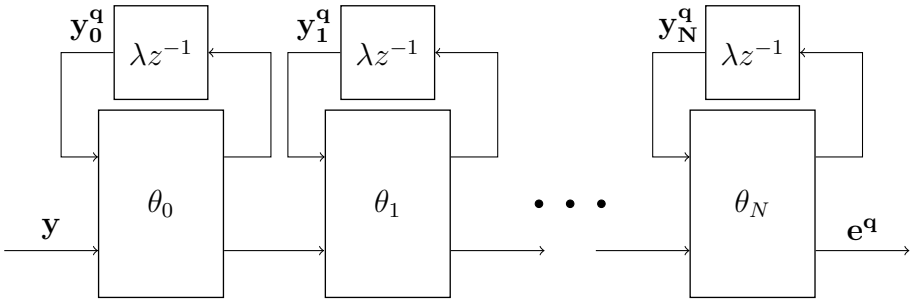

Figure 7.5: The McWhirter structure of the QR algorithm. The rotations obtained from the regressors are used on the rotated output data and the incoming output to produce the error.

given angles can be obtained from the backward prediction errors. The taps of the lattice structure are also the rotated output vector.

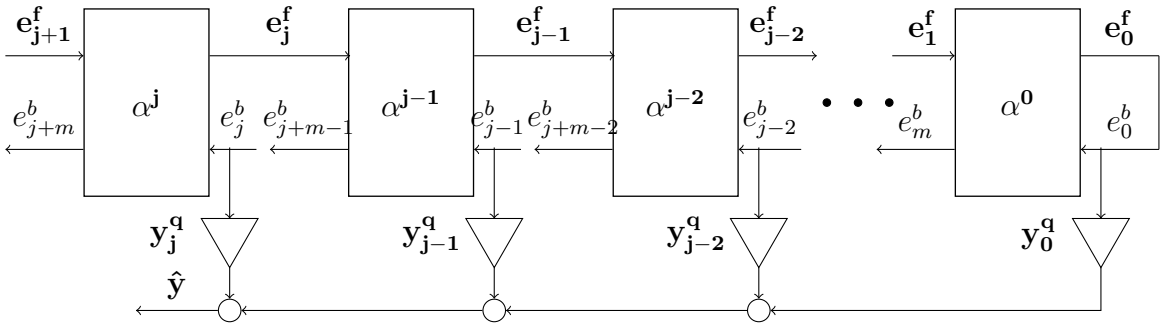

Figure 7.6: The overall structure of the lattice algorthm giving the forward and backward normalized prediction errors with the taps as the rotated output vector.

Other than being numerically stable, by taking advantage of the shift structure of the input regressors the lattice algorithms are of $O(N)$ complexity when compared to $O(N^2)$ for QR and standard RLS. Another advantage is that lattice this lattice algorithm is order recursive. So it will not only give the N^{th} order optimal FIR filter but also all orders less than N for no extra computational burden.

7.3.4 Results

Experimental results were conducted on the magnetic bearing system. Three different test cases were ran:

- The spindle was spun up from purely levitating to 350 Hz both with and without the adaptive controller
- White noise filtered through a 4^{th} order low pass butterworth filter and then injected at the output was used to simulate broadband noise and then tested with and without the adaptive controller
- the broadband noise was also injected during spin up to see if the adaptive controller can handle both broadband and narrow band spin up

It is also worth noting the 4x4 multichannel lattice adaptive filter of order 3 was used for the results in this section.

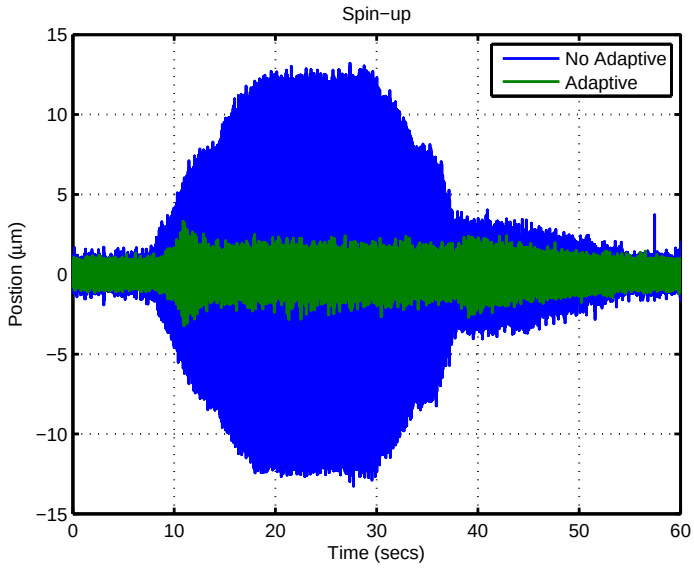

Figure 7.7: the position of one of the axis during spin up to 350 Hz and then back down. The first 5 seconds the rotor is simply levitating.

Figure 7.7 shows the position of one of the axis during spin-up with and without the adaptive controller. The spindle was purely levitating for the first 8 seconds, then the rotor

began to spin up to 350 Hz, finally at 30 seconds it was spun down to rest. The time domain shows the adaptive controller is able to minimize the variance of the output even during spin up transients. Furthermore the position error is less than $2\mu m$ when the adaptive controller is used.

7.3.4.1 Just Levitating

During the purely levitating period from 0 to 8 seconds, as shown in figure 7.8, the adaptive controller is able to attenuate the error about 10 dB below 150 Hz. Although the spectrum does slight raise in the higher frequency region.

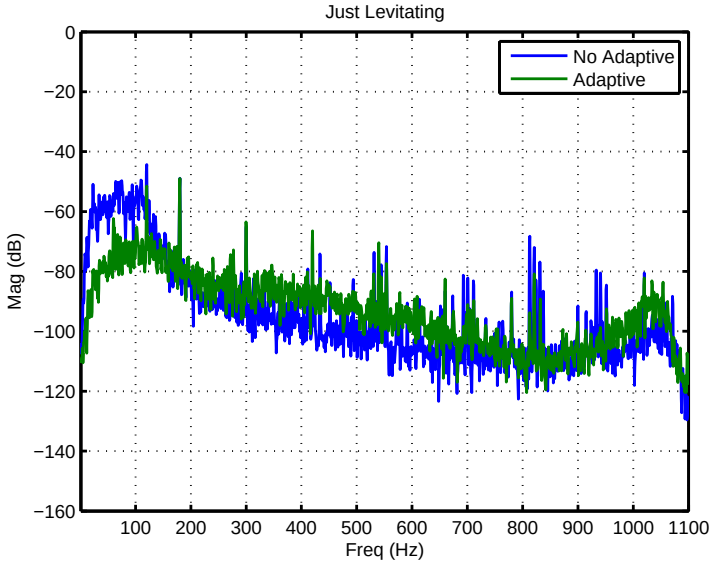

Figure 7.8: The effect of the adaptive control during only levitation.

7.3.4.2 Spinning at 350 Hz

Figure 7.9 shows the power spectrum of the position error while the rotor is spinning at 350 Hz. A 40 dB reduction in the error at the spin frequency is seen. Equally important to note is that the adaptive controller has no knowledge about the frequency (ie. it does not use encoders or any form of frequency measurement) but is still able to attenuate the spin frequency.

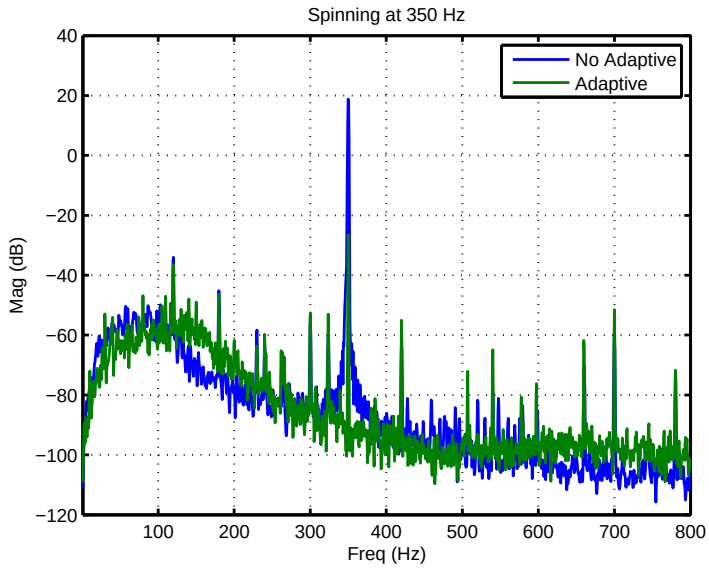

Figure 7.9: While spinning at 350 Hz the adaptive controller is able to attenuate the position error by 40 dB.

7.3.4.3 Spin up Transient

Figure 7.10 shows the spectrogram of the position during spinup. The adaptive controller is able to attenuate the position error by 40 dB even during transients. Once again the adaptive controller has no knowledge about the frequency, and is purely adapting to the estimated disturbance signal.

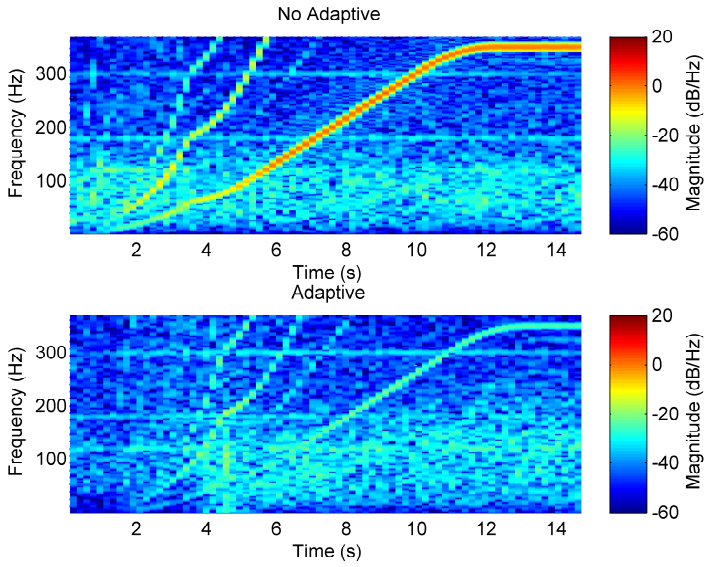

Figure 7.10: During transient spin-up the adaptive controller is able to reduce the position error by 40 dB.

7.3.4.4 Broadband injection

Figure 7.11 shows the position error while a broadband disturbance was injected at the output to simulate broadband disturbance. The adaptive controller was turned on and off at 12 and 34 seconds, to visualize the transient response. The adaptive controller reduces the position error to less than $2\mu m$.

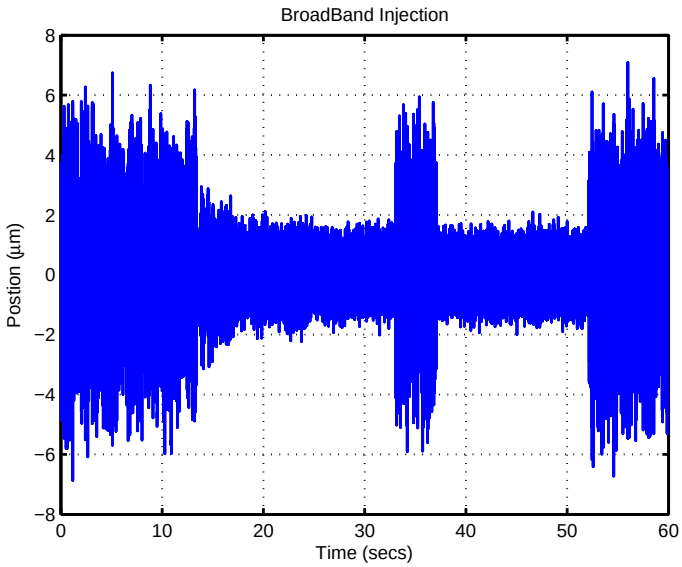

Figure 7.11: The position error when broadband disturbance is injected. At 12 and 34 seconds the adaptive controller is turned off.

Figure 7.12 shows the power spectrum of the position error with and without the adaptive controller. The adaptive controller is able to reduce the error in the low frequency region where the disturbance is but amplifies in the higher frequency region.

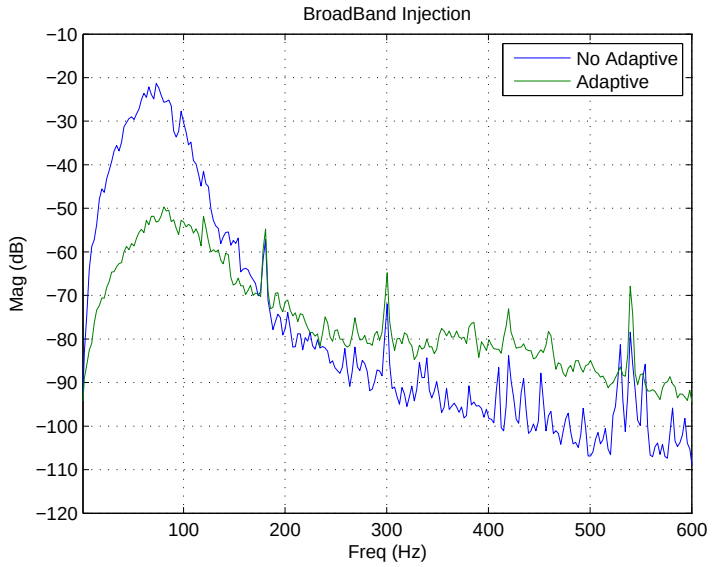

Figure 7.12: Power spectrum of the error with and without the adaptive controller during broadband disturbance injection.

7.3.4.5 Broadband injection During Spin up

In this experiment the rotor was spun up to 350 Hz while a broadband disturbance was also injected. Figure 7.13 shows the time domain results. Clearly, the adaptive controller is minimizing the output position.

Figure 7.14 shows the spectrogram of the position error during spin up. The adaptive controller attenuates the low frequency broadband disturbance while also rejecting the time varying spin frequency.

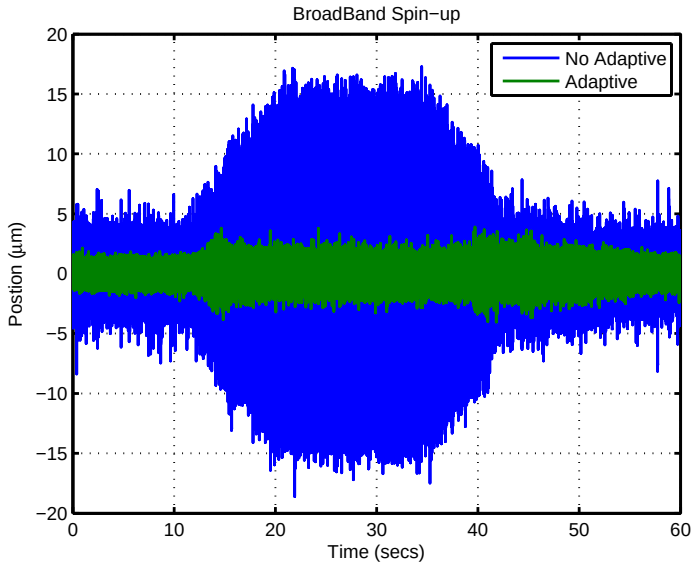

Figure 7.13: Plot of the position error for one of the axis during spin-up with disturbance injection.

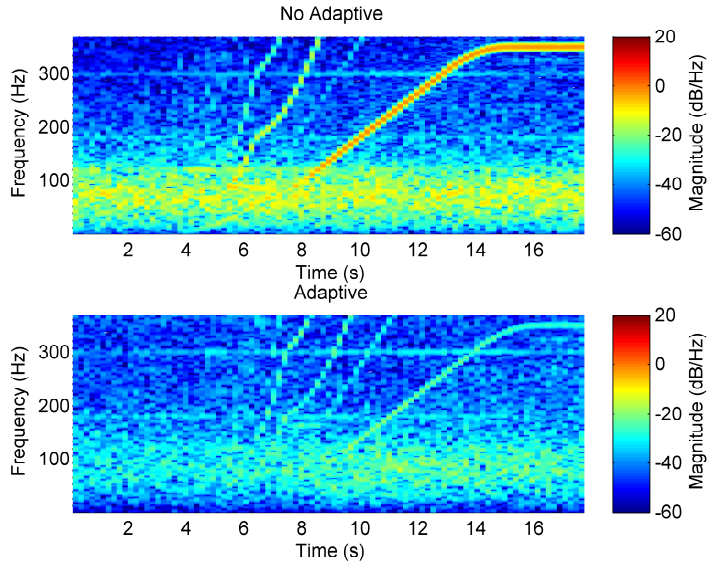

Figure 7.14: Spectrogram of the position during spin up with broadband disturbance injection.

7.4 Receding Horizon as Delayed Inverse

Figure 7.15 shows the maximum singular value of

$$e = z^{-h}I - U(z)F(z)G(z) \tag{7.24}$$

the interpretation is that in the low frequency region where the error is small the adaptive controller is a delayed inverse of the closed loop system. Using high pass weightings increases robustness but at the the cost of a performance. This is the main idea behind the decoupling adaptive control design in the next section which allows for the inversion to shaped.

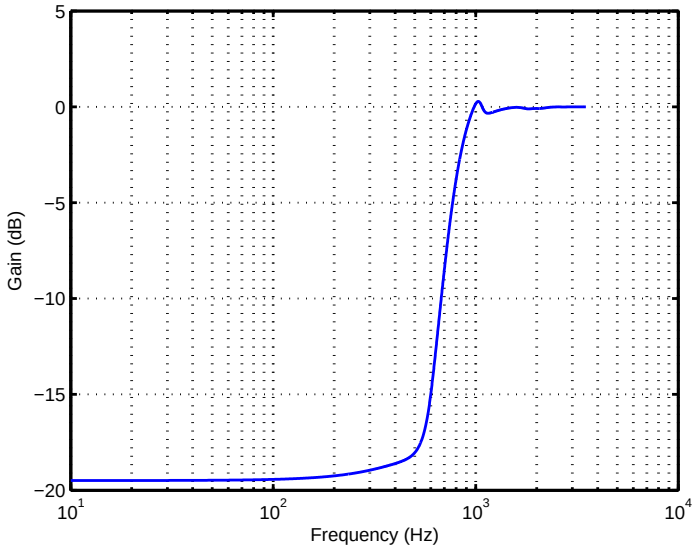

Figure 7.15: maximum singular value of the receding horizon delayed inverse error.

7.5 Decoupling Adaptive Disturbance Rejection

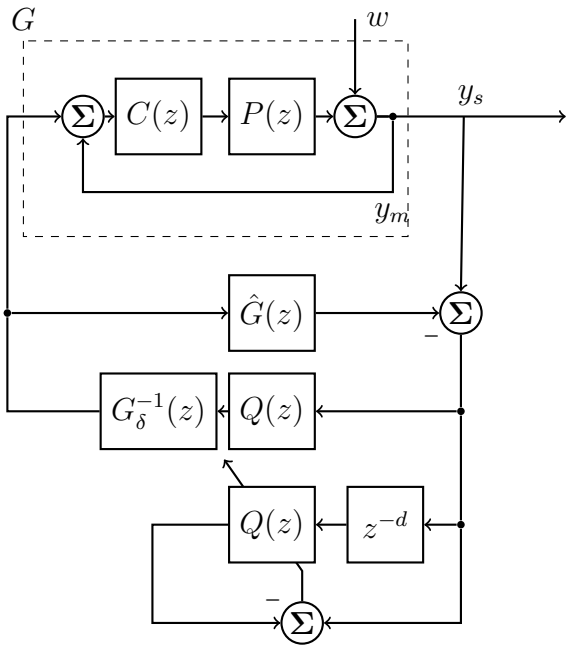

Figure 7.16: The H^∞ adaptive control diagram.

The Decoupling adaptive control scheme explicitly constructs a delayed inverse offline and then uses an adaptive prediction filter to compensate for the delay. The overall control diagram is shown in figure 7.16.

7.5.1 Inverse Design

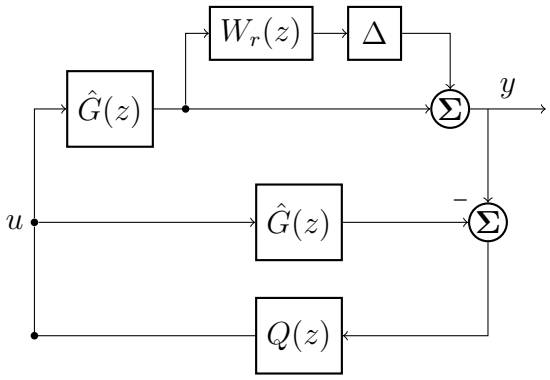

Figure 7.17: The typical internal model controller.

To motivate the Decoupling approach it is useful to consider the standard internal model controller shown in figure 7.17. The stability condition given in eqn. 7.25 can be derived by the small gain theorem.

$$||W_r(z)\hat{G}(z)Q(z)||_\infty < 1 \tag{7.25}$$

Also the sensitivity can be shown to be

$$S(z) = I - G(z)Q(z) \tag{7.26}$$

From the sensitivity it is clear for disturbance rejection the controller $Q(z)$ needs to invert the plant. However, for robustness the controller needs to have small gain in the region $W_r(z)$ is greater than 1. Therefore, the controller needs to invert the plant in the low frequency region of disturbance rejection but needs to have low gain in the high frequency region where the plant is now know as well.

Both of these criteria, can be cast into the following problem eqn 7.27

$$\min_{F(z)\in RH_\infty} \left\| \begin{matrix} [z^{-d}I - G(z)G_\delta^{-1}(z)]W_1(z)r(t) \\ W_2(z)u(t) \end{matrix} \right\|_\infty \tag{7.27}$$

and is shown in figure 7.18 There are three tuning knobs in this formulation: 1) the delay

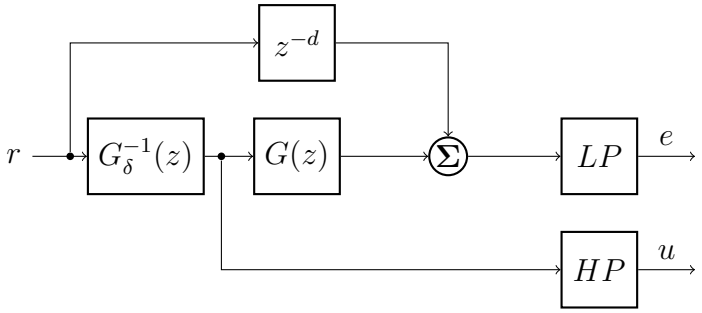

Figure 7.18: The H^∞ problem setup.

length d 2) the lowpass weight on the error 3) the high pass weight on the control input. Increasing the delay length gives a better inversion, but the adaptive prediction filter needs to be able to compensate for it. The lowpass and high pass weighting filters shape the inversion so it inverts in the low frequency region and has low gain in the high frequency region.

7.5.2 Adaptive Prediction

In the low frequency region where the inversion is good

$$G(z)G_{\delta}^{-1}(z) \approx z^{-d}I \tag{7.28}$$

then

$$y \approx (I - z^{-d}Q(z))W_d w \tag{7.29}$$

and the plant is essentially decoupled. An adaptive prediction for the disturbance d steps ahead can be used to compensate for the delayed inverse design.

7.5.3 Results

7.5.3.1 Spinning at 350 Hz

The experiments are similar to that of the receding horizon adaptive controller. The adaptive control order is 3 and the inversion horizon length is 10. Figure 7.19 shows the position error while spinning at 350 Hz, the error is reduced by 40 dB.

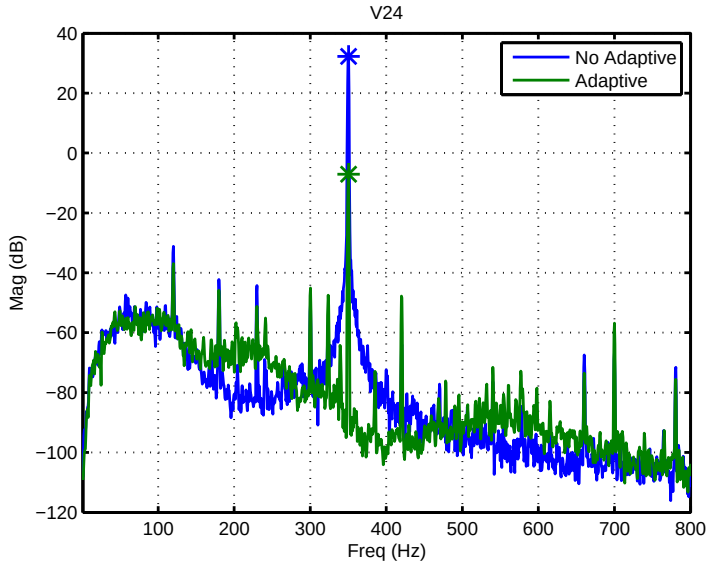

Figure 7.19: The adaptive controller stead-state error while spinning at 350 Hz.

7.5.3.2 Spin Up

Figure 7.20 shows the spectrogram of the position error during spin up. The adaptive controller is able to attenuate the error by 40 dB.

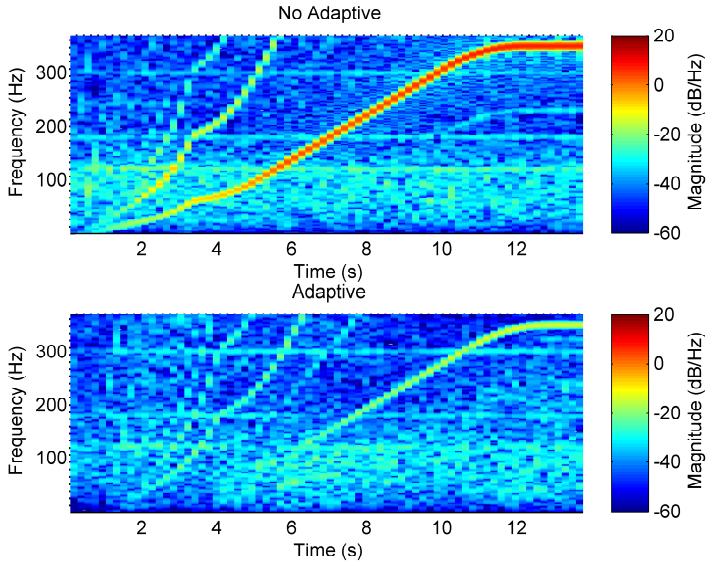

Figure 7.20: Spectrogram of the position error during spin-up.

7.5.3.3 Broadband Disturbance Rejection

Figure 7.21 shows the power spectrum when a broadband disturbance is injected into the output.

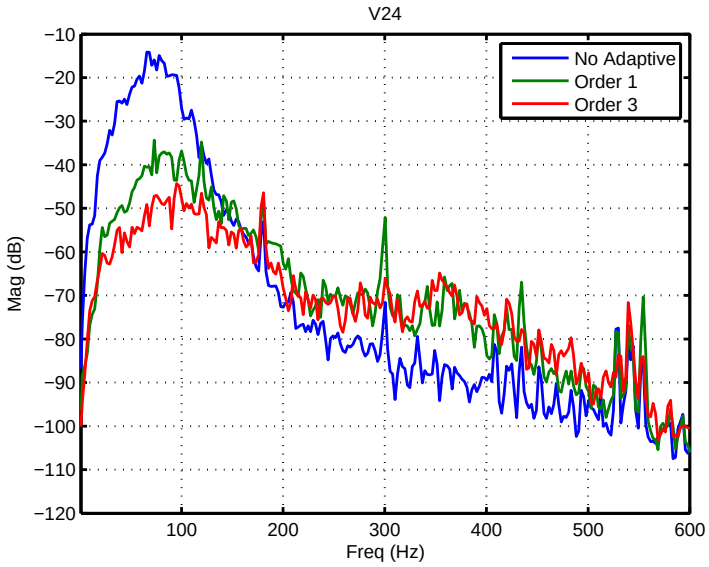

Figure 7.21: Power Spectrum of the position error with the broadband output disturbance injected.

7.5.4 Analysis of Decoupling Approach

Figure 7.22 shows the maximum singular value of

$$e = z^{-d}I - G(z)G_{\delta}^{-1}(z) \tag{7.30}$$

which from the previous section is an indication of the the sensitivity for the overall system. In the low frequency region, e is small and adequate disturbance attenuation can be expected.

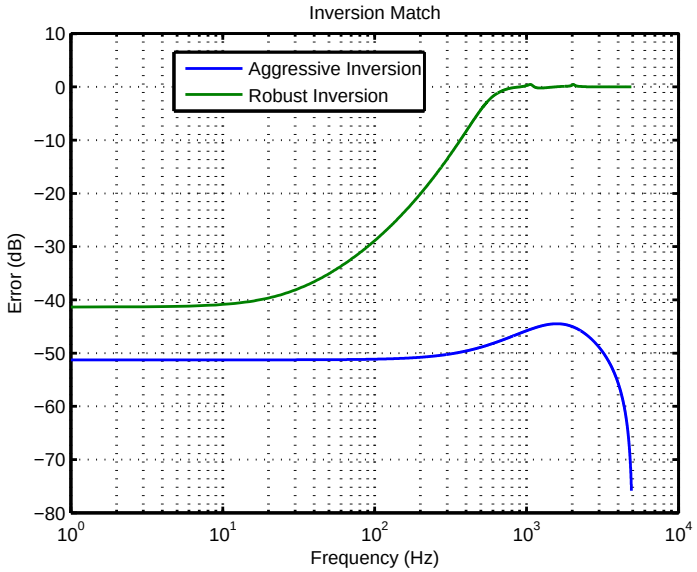

Figure 7.22: Delayed inversion matching error for both the aggressive and robust inversion.

Figure 7.23 shows the maximum singular value of

$$T(z)W_r(z) = G_{\delta}^{-1}G(z)W_r(z) \tag{7.31}$$

which gives an indication of the robustness of the system. Indeed choosing the proper weights is essential for a robust adaptive controller design. Lastly figure 7.24 shows the gains of the aggressive inversion and the robust inversion. The robust inversion rolls off at high frequency and does not amplify high frequency noise and plant/model mismatch.

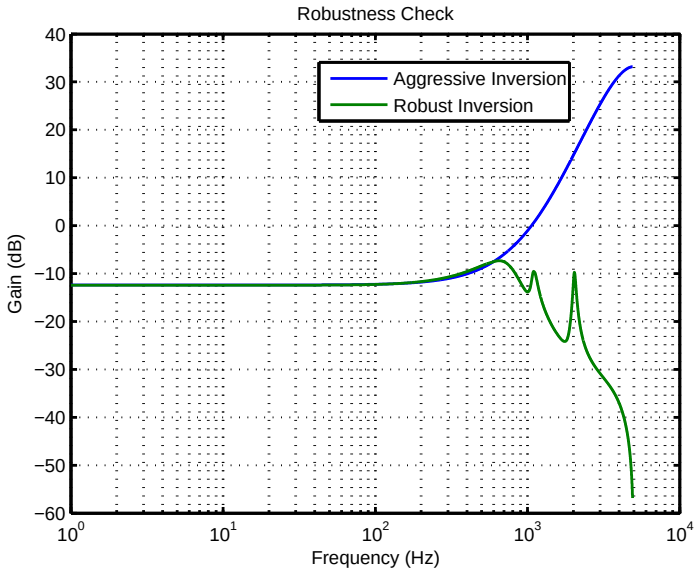

Figure 7.23: Robustness criteria for an aggressive high performance inversion and a robust inversion.

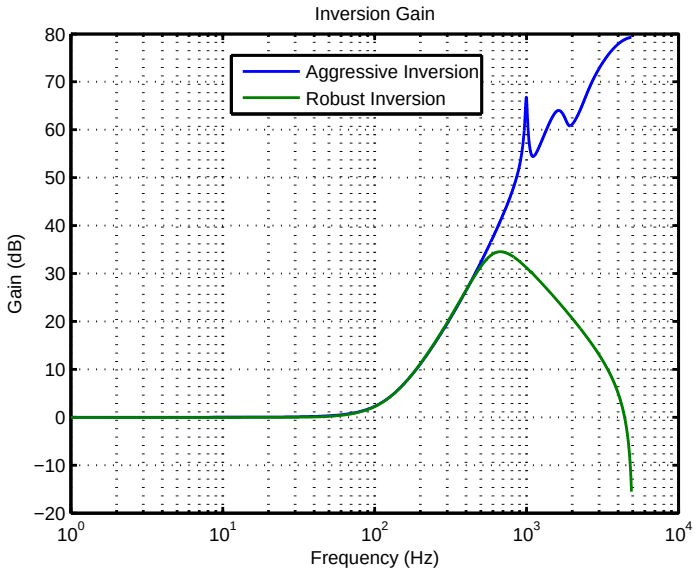

Figure 7.24: The gain of both the aggressive and robust inversion.

CHAPTER 8

Boost Rectifier for THD Minimization

8.1 Introduction

Rectification is concerned with converting AC power into DC. However, often rectification techniques introduce unwanted current harmonics in the utility. It is well known that these harmonics cause voltage distortion, heating, noise, and reduce the capability of the line to provide energy [SSC03]. Thus, it is no surprise that utility companies enforce standards on the levels of harmonics [GCP03]. Because of this fact, there has been plenty of research interest in rectifiers from both a circuit design and control perspective.

Power factor correction uses power transistors to shape the input current in order to achieve unity power factor. By controlling the switching of the transistors, a properly designed power factor scheme can achieve close to unity power factor. In this work, a typical boost rectifier is used to showcase the control algorithm. While it is true that different topology has a great impact on the power factor, the interest in this work is the control algorithm. The goal of the controller is threefold: 1) make the current in phase with the input voltage 2) reduce the harmonics in the input current 3) regulate the output DC voltage.

To meet the aforementioned goals, researchers have studied many different strategies. The typical strategy is a high bandwidth current loop and a low bandwidth voltage loop based on simplified models [WJ97]. Aside from linear controllers, in [MDM08] a sliding mode controller was applied to a linear model obtained from feedback linearization for a single phase active filter. Additionally, in [PRC09] a predictive controller based on a model of the current was used.

For a DC/DC converter, it is quite easy to design a controller to achieve zero steady state

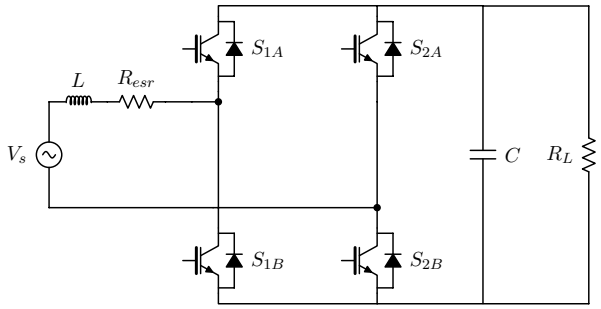

Figure 8.1: Schematic of the Boost Rectifier

error using a PI controller; however, for a rectifier, the control design is more challenging because the current and voltage are AC quantities. In [FY01], a harmonic controller based an internal model for a sinusoid was used to track the first fundamental, but this approach can be difficult to implement in continuous time. Therefore in [MRA05] a DQ transformation is proposed to convert the AC variables into DC quantities so a well-designed Proportional-Integral controller can reduce the errors of the fundamental component to zero in steady state.

A challenging aspect of the rectifier is that it is a nonlinear system, and not amendable to the abundant linear control techniques. Additionally, the point to linearize about is not well defined (the current and voltage are sinusoids). In [SSP03], the linearization points of the AC quantities are chosen to be the RMS value, but this is not the true equilibrium point. In this paper, we expand on [MRA05] and propose to linearize the system in the DQ rotating frame where all the AC quantities become DC variables, so that linear control techniques can be readily applied.

Although PI control in the DQ rotating frame guarantees zero steady state error, it does not compensate for the harmonics other than fundamental. In order to have compensation for other harmonics, a repetitive control, based on internal model principle [FW76b], is applied to the rectifier. In [ZW03], a repetitive controller is applied to a three phase rectifier using an internal dead-beat controller which makes the closed loop system look like a three siso delay systems. This approach is however sensitive to plant mismatch and start-up since it divides by the output voltage. Therefore in this paper, using the linear model in the DQ

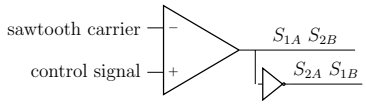

Figure 8.2: Comparator for the PWM

coordinates, a simple multi-variable repetitive controller is added on to compensate for the harmonics.

8.2 Modelling and System ID

Shown in figure 8.1 is the boost rectifier. The boost rectifier consists of 4 IGBTs which form a full bridge, an input inductor, and an output capacitor. Simply, the rectifier converts the AC source voltage (usually the grid) into a DC output voltage. Not to be overlooked is the equivalent series resistance (ESR) of the inductor. As we will be shown in section 8.3, this resistance determines the boost capabilities of the rectifier. The controller must adjust the duty cycle of the transistors to "shape" the current while regulating the output DC voltage. The power factor (PF) is the ratio of the actual power into the rectifier over the apparent power. For a perfectly sinusoidal input voltage, PC is as shown in Eq. 8.1 [EM07]

$$PF = \frac{cos\phi}{\sqrt{1 + THD^2}} \tag{8.1}$$

where

$$THD = \sqrt{\frac{\sum P_{harmonics}}{P_{fundmentals}}} \tag{8.2}$$

In order to achieve unity power factor, the current harmonics must be reduced and input current must be in phase with the input voltage.

8.2.1 Sinusoidal PWM and Sampling Synchronization

For the boost rectifier topology, transistors on the same leg cannot be closed at the same time in order to avoid a short circuit. For this paper, we use a simple sinusoidal PWM, as shown in Figure 8.2, to switch the transistors. A reference triangular signal is compared to

the control signal input (or the duty cycle) which outputs a boolean to transistors S_{1A} and S_{2B} and its complement to S_{1B} and S_{2A}. Clearly, all four transistors change state at the same time; therefore, proper dead time is necessary to avoid shorting the circuit during the switching transients.

Along the same lines, the switching done by the PWM modulator will create high frequency ripples in the circuit. According to the Nyquist sampling theorem, the sampling rate should be at a frequency such that the spectrum of the signal is negligible at the Nyquist frequency. This would require a sampling frequency at least an order of magnitude higher than the switching frequency. Unfortunately since the hardware capability limits the sampling frequency from being too fast, the Nyquist sampling theorem must be violated. However, if the sampling processes are synchronized with the PWM carrier signal properly, the effect of aliasing can be attenuated and the sampled data will be in close proximity to the average value of the actual signal. These issues are discussed in more detail in [BM06] .

8.2.2 State Space Model and System Identification

In order to develop model-based controllers, a mathematical model of the boost rectifier is needed. Assuming ideal switching and applying KCL and KVL, the model shown in figure 8.3 can be obtained where s is 1 or 0 for the IGBTs in the circuit.

$$\begin{bmatrix} \dot{I}_L \\ \dot{V}_C \end{bmatrix} = \begin{bmatrix} \frac{V_s}{L} - (s_{1A} - s_{2A})\frac{V_C}{L} - \frac{R_{esr} I_L}{L} \\ -\frac{V_c}{R_L C} + (s_{1A} - s_{2A})\frac{I_L}{C} \end{bmatrix} \tag{8.3}$$

The difficulty with the given model is that the switching is binary, so by taking the average value of the switching over one PWM cycle the average model of the boost rectifier, is obtained in Eqn. 8.4.

$$\begin{bmatrix} \dot{I}_L \\ \dot{V}_C \end{bmatrix} = \begin{bmatrix} -\frac{R_{esr}}{L} & -\frac{D}{L} \\ \frac{D}{C} & -\frac{1}{R_L C} \end{bmatrix} \begin{bmatrix} I_L \\ V_C \end{bmatrix} + \begin{bmatrix} \frac{V_s}{L} \\ 0 \end{bmatrix} \tag{8.4}$$

Now Equation 8.4 is a continuous, bilinear model. Also since the PWM frequency and sampling are synchronized, the model is valid up to the PWM frequency. It is important

to notice that for a constant duty cycle, the model is linear; therefore, by performing a frequency sweep with only V_s varying the model can be validated. Figures 8.3 and 8.4 show the frequency response of the actual system against the linear state space model (parameters of the circuit are given in Table 8.1) at a duty cycle of .3 and .5, respectively; other duty cycles showed similar good behavior. The frequency response comparison validated the average bilinear model for the rectifier and allowed it to be used for control design.

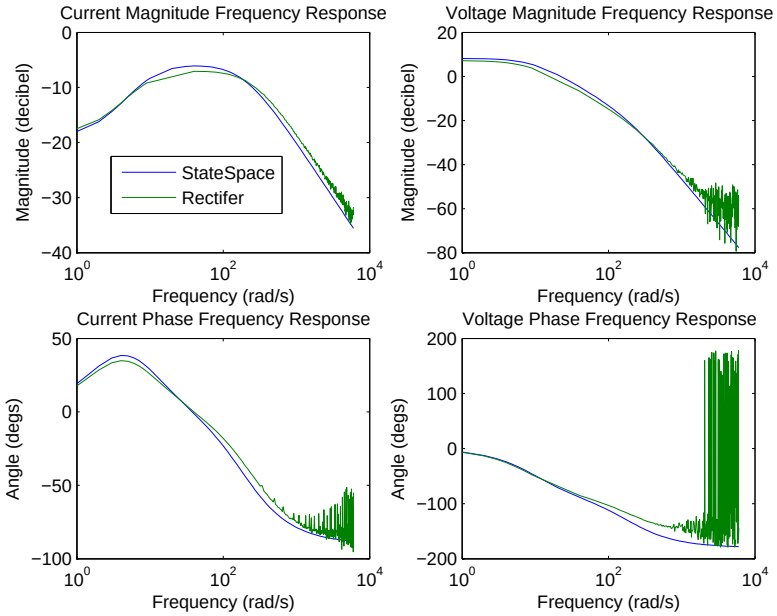

Figure 8.3: Bode Plot of Boost Rectifier with .3 Duty

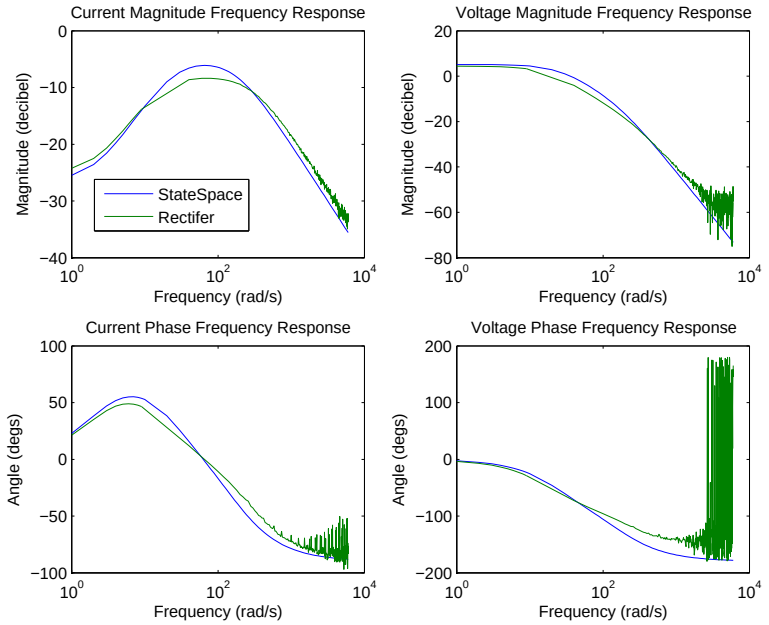

Figure 8.4: Bode Plot of Boost Rectifier with .5 Duty

8.3 DQ Linearized Model

In order to apply linear control design techniques, the model needs to be linearized and equilibrium points chosen. For the output DC voltage Vc, it is straight forward to choose the desired output DC voltage as the equilibrium point. As for the input voltage VAC, it varies from positive peak to negative peak which makes it difficult to choose a reasonable equilibrium point. These issues can be circumnavigated by linearizing the model in the DQ coordinates.

To apply a DQ transformation to single phase converters, two orthogonal quantities are needed. In three phase power systems, the original components are first transformed to the stationary $\alpha\beta$ frame where they are in pairs and orthogonal. Then the DQ transformation matrix in Eqn 8.5 is applied to further transform the orthogonal components into the synchronous DQ rotating frame. A similar procedure as outlined in [ZCS02] is done for single phase inverters, where the quantities are delayed 90 degrees into $\alpha\beta$ coordinates, then the transformation (Eqn. 8.5) is applied to the orthogonal coordinates.

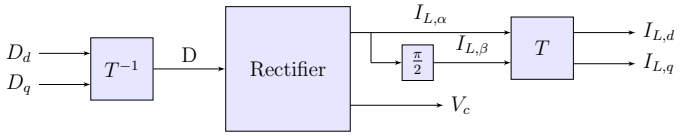

Figure 8.5: Diagram of the Single Phase DQ Transformation for the Boost Rectifier

$$\begin{bmatrix} I_d \\ I_q \end{bmatrix} = \begin{bmatrix} \cos(\omega t) & \sin(\omega t) \\ -\sin(\omega t) & \cos(\omega t) \end{bmatrix} \begin{bmatrix} I_\alpha \\ I_\beta \end{bmatrix} \tag{8.5}$$

8.3.1 DQ Model for Boost Rectifier

A similar DQ transformation as in the inverter case can be applied to single phase boost rectifier. The scheme is graphically shown in Figure 8.5. The current, I_L, is delayed by 90 degrees to form two orthogonal quantities. Since the capacitor voltage is to be regulated at DC, it is assumed to be the same in both the α and β coordinates. With this assumption, there are two orthogonal quantities, and the rectifier model can be written as in Eqn. 8.6

$$\begin{aligned} \begin{bmatrix} \dot{I_{L,\alpha}} \\ \dot{I_{L,\beta}} \end{bmatrix} &= -\begin{bmatrix} I_{L,\alpha} \\ I_{L,\beta} \end{bmatrix} \frac{R_{esr}}{L} + \begin{bmatrix} V_\alpha \\ V_\beta \end{bmatrix} \frac{1}{L} - \begin{bmatrix} D_\alpha \\ D_\beta \end{bmatrix} \frac{V_c}{L} \\ \dot{V_c} &= \frac{1}{2C} \begin{bmatrix} D_\alpha & D_\beta \end{bmatrix} \begin{bmatrix} I_{L,\alpha} \\ I_{L,\beta} \end{bmatrix} - \frac{V_c}{R_L C} \end{aligned} \tag{8.6}$$

Now applying the DQ transformation and using the product rule, the model in the DQ coordinates can be obtained (Equation 8.7). The DQ model is bilinear in both the current and voltage equations, however the sinusoidal quantities are constant which makes the linearization points more intuitive.

$$\begin{bmatrix} \dot{I_{L,d}} \\ \dot{I_{L,q}} \end{bmatrix} = \begin{bmatrix} \frac{-R_{esr}}{L} & \omega \\ -\omega & \frac{-R_{esr}}{L} \end{bmatrix} \begin{bmatrix} I_{L,d} \\ I_{L,q} \end{bmatrix} - \begin{bmatrix} D_d \\ D_q \end{bmatrix} \frac{V_c}{L} + \begin{bmatrix} V_d \\ V_q \end{bmatrix} \frac{1}{L}$$
$$\dot{V_c} = \frac{1}{2C} \begin{bmatrix} D_d & D_q \end{bmatrix} \begin{bmatrix} I_{L,d} \\ I_{L,q} \end{bmatrix} - \frac{V_c}{R_L C} \tag{8.7}$$

8.3.2 Equilibrium Points and Linearization

By setting the derivatives in Eqn. 8.7 to zero, the equilibrium points can be found. Moreover, the equilibrium points give the boost condition of the boost rectifier. The points chosen to linearize about are the desired output voltage ($\bar{V_c}$), the given input source voltage ($\bar{V_d}, \bar{V_q} = 0$), and the desired current in the quadrature coordinate ($I_q = 0$). This gives three equations and three unknowns, which can be solved for the equilibrium points. Combining the three equations gives Eqn. 8.8.

$$\bar{V_d} D_d^2 - \bar{V_c} D_d - \frac{2R_{esr}\bar{V_c}}{R} = 0 \tag{8.8}$$

Equation 8.8 is a second order polynomial for D_d which is restricted to be real. Enforcing the realness of D_d, gives the boost condition shown in Eqn. 8.9. This limits how much the output can be boosted up if the R_{esr} is known. Also, if R_{esr} is considred 0, it is apparent that the output can be boosted as high as desired.

$$\bar{V_c}^2 < \bar{V_d}^2 [\frac{E}{8R_{esr}}] \tag{8.9}$$

Finally, the linearized model, shown in Equation 8.10, can be derived by evaluating the derivatives of the states at the equilibrium point.

$$\begin{bmatrix} \delta\dot{I}_{L,d} \\ \delta\dot{I}_{L,q} \\ \dot{V_c} \end{bmatrix} = \begin{bmatrix} \frac{-R_{esr}}{L} & \omega & -\frac{\bar{D_d}}{L} \\ -\omega & \frac{-R_{esr}}{L} & -\frac{\bar{D_d}}{L} \\ \frac{\bar{D_d}}{2C} & \frac{\bar{D_q}}{2C} & -\frac{1}{R_L C} \end{bmatrix} \begin{bmatrix} \delta I_{L,d} \\ \delta I_{L,q} \\ V_c \end{bmatrix} + \begin{bmatrix} -\frac{\bar{V_c}}{L} & 0 \\ 0 & -\frac{\bar{V_c}}{L} \\ \frac{\bar{I_{L,d}}}{2C} & \frac{\bar{I_{L,q}}}{2C} \end{bmatrix} \begin{bmatrix} \delta D_d \\ \delta D_q \end{bmatrix} \tag{8.10}$$

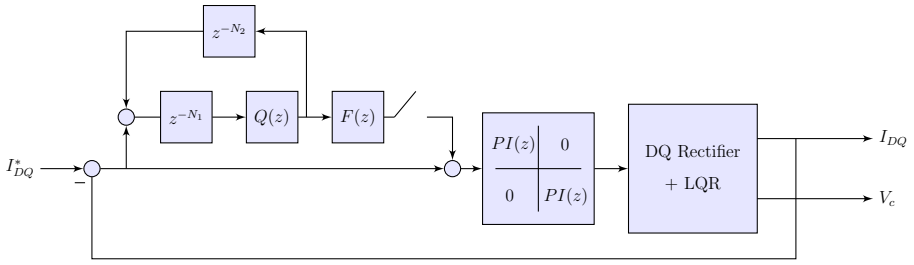

Figure 8.6: Block Diagram of the Plug-in Repetitive Control

8.4 PI, Repetitive, and Resonator Control

In this section three controllers will be described: 1) The traditional PI controller 2) add-on repetitive controller 3) add-on resonator controller. In the DQ coordinates a PI controller can track the fundamental frequency, but is not able to reject unwanted harmonics. Repetitive control is able rejection harmonics, while the resonator controller can target specific harmonics with possible greater attenuation.

8.4.1 PI Control

A typical control strategy is PI in the fixed frame (without the DQ transformation). This controller can behave well if it is properly tuned. Since it is well-known that a PI cannot perfectly track sinusoidal references, the DQ coordinates are attractive since all sinusoidal quantities become a constant which a PI can perfectly track. Therefore, first a PI controller was designed in the DQ coordinates by discretizing the continuous linear DQ model. To speed up the system, a LQR state feedback controller was used, then two diagonal PI controllers were wrapped around as shown in Figure 3.1.

8.4.2 Repetitive Add-On

When the switch in Figure 8.6 is closed, the repetitive controller is added on to the existing PI control. Repetitive control relies on an accurate model to track or reject periodic signals. In order to design a repetitive controller, filters $F(z)$ and $Q(z)$ need to be determined. It is known that for the add on repetitive controller to be stable the inequality in Eqn. 8.11 is a

sufficient condition [Lon10b].

$$\|(I - F(z)H(z))Q(z)\|_\infty < 1 \tag{8.11}$$

In Eqn. 8.11, $H(z)$ is the nominal closed-loop transfer function from reference input to output with the PI controller. From the stability equation it is easy to see that the inequality is satisfied when $F(z) = H^{-1}(z)$. In order to obtain the inverse of the closed loop system, three assumptions are made: 1) the system is minimum phase 2) the relative degree is the same for each sub-system 3)the system is square. Luckily, all of these assumptions are satisfied for the MIMO state space model, Eqn 8.10, for the rectifier in the DQ coordinates.

Given these assumptions, a simple inversion can be obtained as follows. First the closed loop discretized system can be written as in Eqn. 8.12

$$\begin{aligned} x(k+1) &= A_{cl}x(k) + B_{cl}u(k) \\ y(k) &= C_{cl}x(k) \end{aligned} \tag{8.12}$$

Using the state-space model, the d step look-ahead (d is the relative degree of the system) can be written as in Eqn 8.13

$$\begin{aligned} x(k+1) &= A_{cl}x(k) + B_{cl}u(k) \\ y(k+d) &= C_{cl}A_{cl}^{d}x(k) + C_{cl}A_{cl}^{d-1}B_{cl}u(k) \end{aligned} \tag{8.13}$$

Defining $\tilde{C} = C_{cl}A_{cl}^{d}$ and $\tilde{D} = C_{cl}A_{cl}^{d-1}B_{cl}$, the inverse of the look-ahead system in state space form is as shown in Eqn 8.14. The look-ahead requirement can be emulated by using the appropriate delays in the internal model as is done in the standard SISO case [TTC89b].

$$\begin{aligned} x(k+1) &= (A_{cl} - B_{cl}\tilde{D}^{-1}\tilde{C})x(k) + \tilde{D}y(k+d) \\ u(k) &= \tilde{D}^{-1}\tilde{C}x(k) + \tilde{D}^{-1}y(k+d) \end{aligned} \tag{8.14}$$

Ideally, the inverse guarantees that the inequality in Eqn 8.11 is satisfied. However, at high frequencies, the model is usually not accurate, which can violate the inequality. The Q

filter, which is 1 at low frequencies and near 0 at high frequencies, can provide robustness to this mismatch. For the rectifier, the Q filter is chosen as shown in Eqn 8.15. $Q(z)$ is a noncasual and diagonal 2 by 2 system or order N_q.

$$Q(z) = \begin{bmatrix} q(z) & 0 \\ 0 & q(z) \end{bmatrix} \tag{8.15}$$
$$q(z) = (.25z + .5 + .25z^{-1})^{N_q}$$

Having described the design of $F(z)$ and $Q(z)$, it is important to note they are both noncasual filters of order d and N_q respectively. N is defined to be the number of samples in one period of the reference signal and it determines the number of delays in the repetitive control structure. The noncasual filters can be mimicked by borrowing from the overall delay. Equations 8.16 and 8.17 show the number of delays needed in the repetitive control structure (Figure 8.6).

$$N_1 = N - d - N_q \tag{8.16}$$
$$N_2 = d \tag{8.17}$$

8.4.3 Resonator Add-on

In order to generate an internal model at the desired frequencies, a filter $L(z)$ is designed so to satisfy

$$L(z^{-1}) = \begin{cases} L = 1 \text{ if } \omega = \omega_{k=1,2,\ldots p} \\ L \approx 0 \text{ if } \omega \neq \omega_k \end{cases} \tag{8.18}$$

where the filter reaches unity at p number of frequencies and is approximately zero elsewhere. When placed in a positive feedback loop, the internal model generators infinite control action at the desired frequencies while producing none at the others. The design of L

filter can be reduced to an All Pass design problem. This can be see by equation 8.19, where $A(z)$ is a high order all pass filter. Therefore, by designing an all pass filter with correct phase at the prescribed frequency a suitable $L(z^{-1})$ filter can be obtained

$$L(z) = \frac{1}{2}(1 - A(z)) \tag{8.19}$$

To design the All pass filter, the approach described in [PT97] is used. It can be readily verified that phase of an all pass filter is given by

$$\theta_A = -2M\omega + 2\arctan(\frac{\sum_{k=1}^{2M} a_k \sin(k\omega)}{1 + \sum_{k=1}^{2M} a_k \cos(k\omega)}) \tag{8.20}$$

given a phase response at $2M$ points then eqn 8.20 can be cast as linear system

$$\tan(\beta_i) = \sum_{k=1}^{2M} [\sin(k\omega_i) - \tan(\beta_i)\cos(k\omega)]a_k \tag{8.21}$$

where i ranges from 1 to $2M$.

The basic idea is seen from 8.19. By designing an all pass filter that has 180 degrees of phase at the peak frequencies and +/- 90 degrees of phase at the peak bandwidths, equation 8.19 will produce multiple peak filter. When the All pass filter has 180 degrees of phase then equation 8.19 will be one as desired. Moreover by setting the phase to be 90 degrees at $w_i - \frac{BW}{2}$ the -3 dB point is set. This highlights one of the benefits of this design approach, the bandwidth and peak locations can be set independently. Another advantage of using this linear system approach for the design of $L(z)$ filter is the condition number determines if placement of the peaks is possible. Put in other words, placing peaks too close together will make the linear system very ill conditioned.

A sufficient condition for the stability of the resonator is given by equation 8.22. The inversion used in the repetitive control design will not work in this case since $L(z^{-1})$ has relative order zero and is therefore unable to absorb any look aheads. Using the fact that $L(z^{-1})$ is unity at the interested frequencies and nearly zero elsewhere, the inequality 8.22 can be approximated by an interpolation constraint (equation 8.23). Assuming $F(z) = A_0 + A_1 z^{-1} ... A_N z^{-N}$, namely has FIR structure, the interpolation can be casted as a least squares problem (equation 8.25). The FIR inversion filter is interpolated at M points which

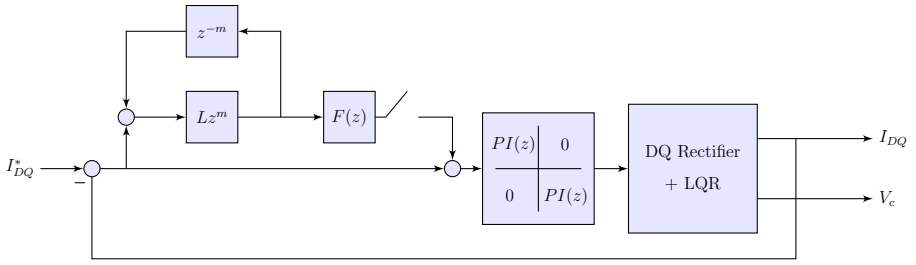

Figure 8.7: Block Diagram of the Plug-in Resonator

are at and around the interested frequencies. Since the solution to the least squares is restricted to be real, it is a constrained phase least squares problem which the solution is given by 8.26. Design of the inverse filter using the method describes is an iterative process with the order of the filter and interpolation points as tuning knobs. Once a solution is obtained, it can be substituted into the inequality 8.22 to verify it meets the stability condition.

$$\|(I - F(z)H(z))L(z)\|_\infty < 1 \tag{8.22}$$

$$F(e^{j\omega_i}) = H(e^{j\omega_i})^{-1} \tag{8.23}$$

$$\omega_i = \omega_1 ... \omega_p \tag{8.24}$$

$$\begin{bmatrix} I & e^{-j\omega_1}I & e^{-2j\omega_1}I... & e^{-Nj\omega_1}I \\ . & . & . & . \\ . & . & . & . \\ I & e^{-j\omega_M}I & e^{-2j\omega_M}I... & e^{-Nj\omega_M}I \end{bmatrix} \begin{bmatrix} A_0 \\ . \\ . \\ A_N \end{bmatrix} = \begin{bmatrix} H(e^{j\omega_1})^{-1} \\ . \\ . \\ H(e^{-j\omega_M})^{-1} \end{bmatrix} \tag{8.25}$$

$$A_{fir} = Re(A^*A)^{-1}Re(A^*H(e^{j\omega})) \tag{8.26}$$

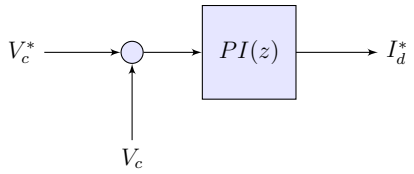

Figure 8.8: Outer PI Loop for Voltage Control

8.4.4 Outer Voltage Loop

To regulate the capacitor voltage, an outer voltage loop is wrapped around the current loop. The error is formed as shown in Figure 8.8 and fed into a PI controller, which gives the I_d reference (Iq reference is 0) to the current loop. The main design criterion is that the bandwidth of the outer PI loop must be smaller than the current loop, or else unwanted distortion of the current may result. Many authors use the same outer voltage loop, so its design will not be discussed any further. Except to say that using the linear DQ model 8.7 another LTI controller can be designed for the outer loop if necessary.

8.5 Experimental Results

8.5.1 Experiment Setup

The schematic in figure 8.1 was the hardware set up. A ST IGBT module and an optocoupler for isolation was used for the IGBT bridge. The input sinusoidal voltage was created using a TI OPA541 power amp, so a simple amplifier circuit can mimic the power source. The inductor current was measured across a 1Ω shunt resistor, while the capacitor voltage was measured using a divider circuit. All signals were fed into a NI 7833 R card running on a PC target, which has a FPGA that handled PWM, synchronization, sampling, and delay. The PC target communicated with the FPGA and ran all the control algorithms. National Instrument's Labview makes this FPGA and PC target communication relatively easy. Table 8.1 shows the values of the parameters used for the experiment. Also, the pwm (sampling) frequency was chosen to be 10 KHz.

Table 8.1: Experimental Parameters

Parameter	Value
L	10 mH
C	6 mF
R	75 Ω
V_{in}	12 VAC

8.5.2 Experimental Results

The desired output voltage was set at 15 V and the input frequency at 50 Hz. Three different controllers were compared: 1) a PI controller in the DQ coordinates 2) a repetitive add-on was added 3) a resonator was added on.

The rest of this section shows results first the current and duty cycle for the three controllers. Then the output voltage regulation for the each of controller. Followed by a harmonics analysis of the input current and the phase of the current wrt the input voltage for each of controller.

8.5.2.1 DQ Current and Duty

As shown in figure 8.9, the repetitive and resonator add-on is more aggressive than the PI controller. The duty cycle plot also shows a diode non-linearity at the zero crossing in the circuit which the controller attempts to compensate for. Repetitive controller had a Q filter of order two; lower order Q filters were shown to be unstable since the controller attempts to over correct for the non-linearity.

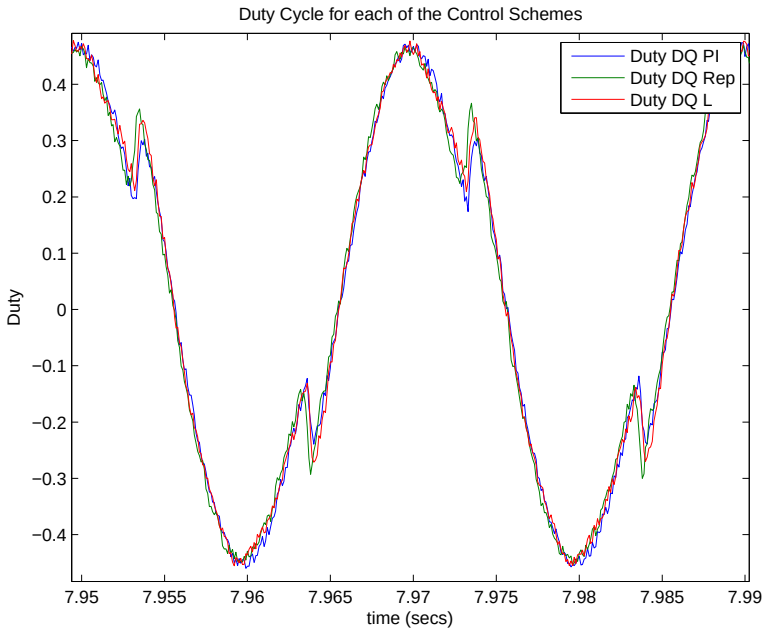

Figure 8.9: Duty Cycle for the Three Controllers

The advantage of the add-on repetitive is clearly seen in the DQ currents. As shown in figure 8.10, the repetitive controller reduces the variation in both the D and Q currents. The nonlinearities in the circuit create harmonics which a simple PI controller is not able to fully reject.

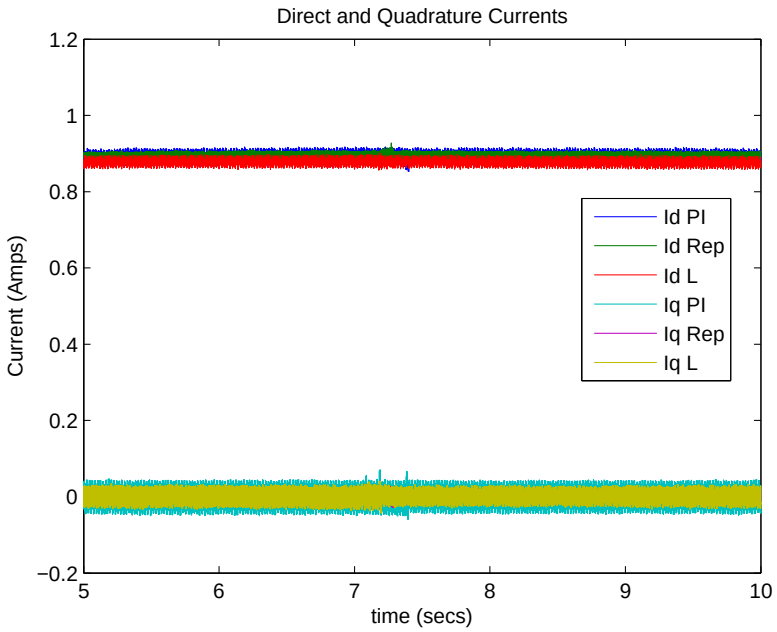

Figure 8.10: Current in the DQ Coordinates for PI and Add-on Repetitive

8.5.2.2 Output Voltage

The output voltage is shown in Figure 8.11. From 0 to 1 seconds, an open loop sinusoidal duty cycle is fed in; afterwards, the controller is turned on. The settling time for all controllers are the similar since the same PI bandwidth was chosen for the outer loop, and was chosen to be long so the controller does not interfere with the current loop controller.

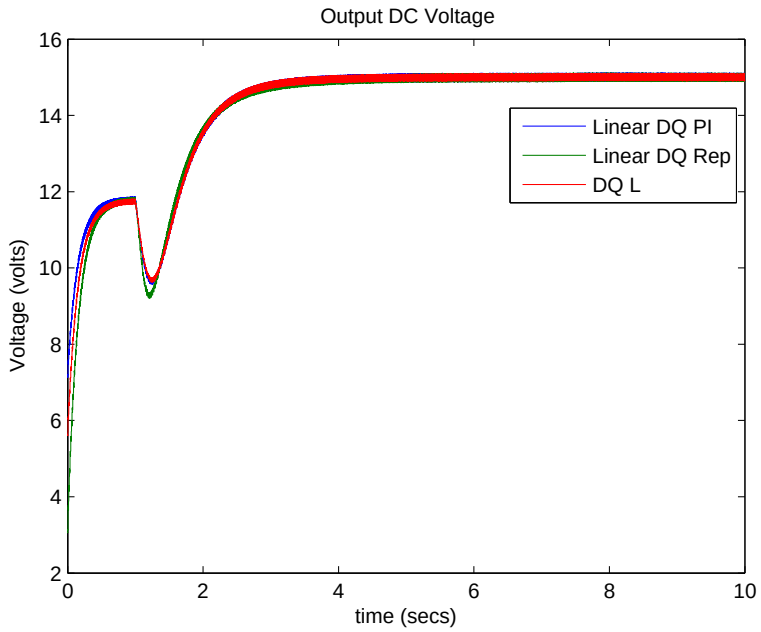

Figure 8.11: Output Voltage for the Three Controllers

8.5.2.3 Harmonics

As stated in Eqn 8.1, the power factor is dependant on both the phase and THD of the input current. Shown in Figure 8.12 is the the harmonic content of the current using the three different controllers. The fundamental is tracked well by all controllers, which indicates the current amplitude is approximately equal. This is expected because of the outer PI voltage loop. The $L(z^{-1})$ was designed to have peaks at 50 Hz, 150 Hz, 200 Hz, 250 Hz, 300 Hz, and 400 Hz.

From Table 8.3, it is clear that the add-on repetitive controller is able to significantly reduce the harmonics. PI in the DQ frame reduces harmonics by 2 dB. This improvement pales in comparison to the add on repetitive, which attenuates harmonics over 20 dB, showing that PI alone may not be able to satisfactorily meet harmonic requirements, even in the DQ coordinates.

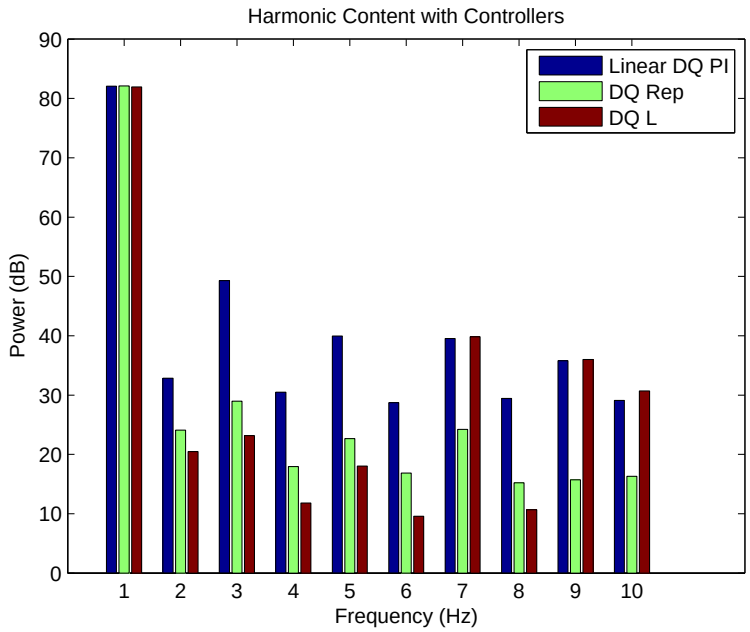

Figure 8.12: Harmonic Content for the Three Controllers

Table 8.2: THD in DB for the Three Controllers

Controller	THD (dB)
DQ PI	-31
DQ Rep	-51
DQ L	-56

Table 8.3: Phase for the Three Controllers

Controller	Phase (deg)
DQ PI	.648
DQ Rep	.646
DQ L	.648

8.6 Conclusion

In this chapter, we have two main results for the standard single phase boost rectifier: 1) The formulation of a linear model in the DQ domain suitable for controller design 2) A MIMO repetitive add-on controller was designed using the linear model to reduce harmonics not compensated for by a nominal controller. In the process of deriving the linear model, analysis of the equilibrium points gave the boost condition for the rectifier. Experimental results proved the effectiveness of using the linear model for controller design and of the repetitive controller for reducing harmonics. The methodology can be used for designing controllers that operate at near unity power factor.

Future work can include analyzing the controller design from a robust point of view using the linear model. Also using the model to develop other types of linear controllers.

CHAPTER 9

Conclusions and Future Directions

This thesis presents an experimental investigation for an active magnetic bearing system (AMBS) specifically for cutting applications. A high order ARX identification method conducted within stabilized feedback loops followed by balanced truncation model reduction was efficient and effective in obtaining the open loop unstable multivariable AMBS dynamic model, which agrees well with the system's frequency response data. Also the severe flexible nature of the spindle is seen in the frequency response both while stationary and spinning, which facilitates the need for robust controller design. The experimentally obtained model is augmented to include the tip dynamics by impulse hammer testing that allows for the inclusion on cutting dynamics into the overall control system.

In cutting application there are two main concerns: the tip tracking a profile and avoidance of chatter instability. Therefore, based on the identified model, a two-step optimal repetitive controller was designed for minimal error tracking. The first controller consisted of a control input weighted linear quadratic control with integral action that ensured stability, broadband performance, and robustness. Then a plug-in multivariable repetitive controller with modifications for enhanced performance and non-harmonic compensation was designed by optimal model matching that highlights the classical trade-off between robustness and performance. A cutting force model was incorporated into the overall system, and stability lobes obtained for optimal cutting conditions.

Vibration reduction is crucial in applications of magnetic bearings such as energy storage. An adaptive feedforward control was seen to be effective in reducing housing vibrations even while the spin frequency is changing. The regressors were filtered through a multivariable filter obtained from gradient descent. The adaptive controller has a linear time invariant

state space representation from which the deviations of the add-on adaptive from the nominal sensitivity and complementary sensitivity can be analyzed. Experimental results did indeed show that vibrations can be reduced even while the spindle speed is changing.

The single input single output adaptive inverse control was extended to the multivariable case and demonstrated to be effective in rejecting narrow and broadband disturbances. Two formulations that can accommodate multivariable plants were considered: the receding horizon adaptive control and the decoupling adaptive control. Both methods need a multivariable adaptive filter such as RLS or LMS; in this thesis a multivariable lattice RLS filter was chosen for its numerical stability and $O(N)$ complexity. Experimental results on the magnetic bearing system show the effectiveness of both control schemes.

Lastly, there were two main results for the standard single phase boost rectifier: 1) The formulation of a linear model in the DQ domain suitable for controller design 2) A MIMO repetitive add-on controller with peak filter modification was designed using the linear model to reduce harmonics not compensated for by a nominal controller. In the process of deriving the linear model, analysis of the equilibrium points gave the boost condition for the rectifier. Experimental results proved the effectiveness of using the linear model for controller design and the repetitive controller for reducing harmonics. The methodology can be used for designing controllers that operate at near unity power factor.

Some future directions can be summarized

1. The augmented model and a cutting chatter model can be used with H_∞ control methods to stiffen the tip at the flexible model.

2. In an effort to make the rotor system "smart", more advanced fault detection schemes can be used.

3. Additionally, the broadband adaptive control techniques can be used to compensate for disturbances introduced by the cutting process.

References

[AKU99] Foued Ben Amara, Pierre T Kabamba, and A Galip Ulsoy. "Adaptive sinusoidal disturbance rejection in linear discrete-time systemsPart II: Experiments." *Journal of Dynamic Systems, Measurement, and Control*, **121**(4):655–659, 1999.

[BCK09] Hannes Bleuler, Matthew Cole, Patrick Keogh, R Larsonneur, E Maslen, Y Okada, G Schweitzer, A Traxler, Gerhard Schweitzer, Eric H Maslen, et al. *Magnetic bearings: theory, design, and application to rotating machinery*. Springer Science & Business Media, 2009.

[BD97] Marc Bodson and Scott C Douglas. "Adaptive algorithms for the rejection of sinusoidal disturbances with unknown frequency." *Automatica*, **33**(12):2213–2221, 1997.

[BHW10] HMNK Balini, Ivo Houtzager, Jasper Witte, and Carsten W Scherer. "Subspace identification and robust control of an AMB system." In *American Control Conference (ACC), 2010*, pp. 2200–2205. IEEE, 2010.

[BM06] Simone Buso and Paolo Mattavelli. "Digital control in power electronics." *Lectures on Power Electronics*, **1**(1):1–158, 2006.

[BSW11] HMNK Balini, Carsten W Scherer, and Jasper Witte. "Performance enhancement for AMB systems using unstable controllers." *IEEE Transactions on Control Systems Technology*, **19**(6):1479–1492, 2011.

[CDX04] Li Cuiyan, Zhang Dongchun, and Zhuang Xianyi. "A survey of repetitive control." In *IEEE/RSJ international conference on intelligent robots and systems*, 2004.

[CK07] Min Chen and Carl R Knospe. "Control approaches to the suppression of machining chatter using active magnetic bearings." *Control Systems Technology, IEEE Transactions on*, **15**(2):220–232, 2007.

[CKB00] MOT Cole, PS Keogh, and CR Burrows. "Adaptive-Q control of vibration due to unknown disturbances in rotor/magnetic bearing systems." In *Control Applications, 2000. Proceedings of the 2000 IEEE International Conference on*, pp. 965–970. IEEE, 2000.

[Cse03] Tibor Cselle. "Piezoelectric adjusting mechanism.", July 1 2003. US Patent 6,586,862.

[CT12] Xu Chen and Masayoshi Tomizuka. "A minimum parameter adaptive approach for rejecting multiple narrow-band disturbances with application to hard disk drives." *IEEE Transactions on Control Systems Technology*, **20**(2):408–415, 2012.

[CT13] Xu Chen and Masayoshi Tomizuka. "Selective model inversion and adaptive disturbance observer for time-varying vibration rejection on an active-suspension benchmark." *European Journal of Control*, **19**(4):300–312, 2013.

[EM07] Robert W Erickson and Dragan Maksimovic. *Fundamentals of power electronics*. Springer Science & Business Media, 2007.

[FHM93] Masayuki Fujita, Kazuhiro Hatake, Fumio Matsumura, and Kenko Uchida. "Experiments on the loop shaping based H, control of a magnetic bearing." In *American Control Conference, 1993*, pp. 8–13. IEEE, 1993.

[FW76a] Bruce A Francis and W Murray Wonham. "The internal model principle of control theory." *Automatica*, **12**(5):457–465, 1976.

[FW76b] Bruce A Francis and W Murray Wonham. "The internal model principle of control theory." *Automatica*, **12**(5):457–465, 1976.

[FY01] Shoji Fukuda and Takehito Yoda. "A novel current-tracking method for active filters based on a sinusoidal internal model [for PWM invertors]." *Industry Applications, IEEE Transactions on*, **37**(3):888–895, 2001.

[GB10] Xiuyan Guo and Marc Bodson. "Equivalence between adaptive feedforward cancellation and disturbance rejection using the internal model principle." *International journal of adaptive control and signal processing*, **24**(3):211–218, 2010.

[GCP03] Oscar Garcia, José Cobos, Roberto Prieto, Pedro Alou, Javier Uceda, et al. "Single phase power factor correction: a survey." *Power Electronics, IEEE Transactions on*, **18**(3):749–755, 2003.

[GH95] Conard Gähler and Raoul Herzog. "Identification of magnetic bearing systems." *Mathematical Modelling of Systems*, **1**(1):29–45, 1995.

[GMH97] Conrad Gahler, Manuel Mohler, and Raoul Herzog. "Multivariable identification of active magnetic bearing systems." *JSME International Journal Series C Mechanical Systems, Machine Elements and Manufacturing*, **40**(4):584–592, 1997.

[HBG96] Raoul Herzog, Philipp Buhler, Conrad Gahler, and Rene Larsonneur. "Unbalance compensation using generalized notch filters in the multivariable feedback of magnetic bearings." *IEEE Transactions on Control Systems Technology*, **4**(5):580–586, 1996.

[HL95] Roberto Horowitz and Bo Li. "Adaptive control for disk file actuators." In *Decision and Control, 1995., Proceedings of the 34th IEEE Conference on*, volume 1, pp. 655–660. IEEE, 1995.

[Jan03] Magnus Jansson. "Subspace identification and ARX modeling." *Proceedings of SYSID 2003*, 2003.

[KHF95] Carl R Knospe, R Winston Hope, Stephen J Fedigan, and Ronald D Williams. "Experiments in the control of unbalance response using magnetic bearings." *Mechatronics*, **5**(4):385–400, 1995.

[KLT04] Byung-Sub Kim, Jianwu Li, and Tsu-Chin Tsao. "Two-parameter robust repetitive control with application to a novel dual-stage actuator for noncircular machining." *IEEE/ASME Transactions on mechatronics*, **9**(4):644–652, 2004.

[KT16] Christopher Kang and Tsu-Chin Tsao. "Control of Magnetic Bearings for Rotor Unbalance With Plug-In Time-Varying Resonators." *Journal of Dynamic Systems, Measurement, and Control*, **138**(1):011001, 2016.

[LCR05] Ioan Doré Landau, Aurelian Constantinescu, and Daniel Rey. "Adaptive narrow band disturbance rejection applied to an active suspensionan internal model principle approach." *Automatica*, **41**(4):563–574, 2005.

[Lia13] Jiancheng Liang. "Method of forming piston pin holes and boring system therefor.", August 13 2013. US Patent 8,506,215.

[Lju99] Lennart Ljung. "System identification: Theory for the user, ptr prentice hall information and system sciences series." *ed: Prentice Hall, New Jersey*, 1999.

[LM96] Lennart Ljung and Tomas McKelvey. "Subspace identification from closed loop data." *Signal processing*, **52**(2):209–215, 1996.

[Lon10a] Richard W Longman. "On the Theory and Design of Linear Repetitive Control Systemsg." *European Journal of Control*, **16**(5):447–496, 2010.

[Lon10b] Richard W Longman. "On the Theory and Design of Linear Repetitive Control Systemsg." *European Journal of Control*, **16**(5):447–496, 2010.

[MB95] William Messner and Marc Bodson. "Design of adaptive feedforward algorithms using internal model equivalence." *International Journal of Adaptive Control and Signal Processing*, **9**(2):199–212, 1995.

[MDM08] José Matas, Luis Garcia De Vicuna, Jaume Miret, Josep M Guerrero, and Miguel Castilla. "Feedback linearization of a single-phase active power filter via sliding mode control." *Power Electronics, IEEE Transactions on*, **23**(1):116–125, 2008.

[MRA05] U de A Miranda, LGB Rolim, and M Aredes. "A DQ synchronous reference frame current control for single-phase converters." In *Power Electronics Specialists Conference, 2005. PESC'05. IEEE 36th*, pp. 1377–1381. IEEE, 2005.

[MST03] Riccardo Marino, Giovanni L Santosuosso, and Patrizio Tomei. "Robust adaptive compensation of biased sinusoidal disturbances with unknown frequency." *Automatica*, **39**(10):1755–1761, 2003.

[NI96] Kenzo Nonami and Takayuki Ito. "μ synthesis of flexible rotor-magnetic bearing systems." *IEEE Transactions on Control Systems Technology*, **4**(5):503–512, 1996.

[NSL15] Amin Noshadi, Juan Shi, Wee Sit Lee, Peng Shi, and Akhtar Kalam. "System Identification and Robust Control of Multi-Input Multi-Output Active Magnetic Bearing Systems." 2015.

[PDA09] Goele Pipeleers, Bram Demeulenaere, Farid Al-Bender, Joris De Schutter, and Jan Swevers. "Optimal performance tradeoffs in repetitive control: Experimental validation on an active air bearing setup." *IEEE Transactions on Control Systems Technology*, **17**(4):970–979, 2009.

[PFX15] Cong Peng, Jiancheng Fang, and Xiangbo Xu. "Mismatched disturbance rejection control for voltage-controlled active magnetic bearing via state-space disturbance observer." *IEEE Transactions on Power Electronics*, **30**(5):2753–2762, 2015.

[PRC09] Marcelo Pérez, Jose Rodriguez, and Antonio Coccia. "Predictive current control in a single phase PFC boost rectifier." In *Industrial Technology, 2009. ICIT 2009. IEEE International Conference on*, pp. 1–6. IEEE, 2009.

[PT97] Soo-Chang Pei and Chien-Cheng Tseng. "IIR multiple notch filter design based on allpass filter." *Circuits and Systems II: Analog and Digital Signal Processing, IEEE Transactions on*, **44**(2):133–136, 1997.

[PTG10] Néstor O Pérez-Arancibia, Tsu-Chin Tsao, and James S Gibson. "Saturation-induced instability and its avoidance in adaptive control of hard disk drives." *IEEE Transactions on Control Systems Technology*, **18**(2):368–382, 2010.

[Reg91] Phillip A Regalia. "An improved lattice-based adaptive IIR notch filter." *IEEE transactions on signal processing*, **39**(9):2124–2128, 1991.

[SBL94] Beale Shafai, S Beale, P LaRocca, and E Cusson. "Magnetic bearing control systems and adaptive forced balancing." *IEEE Control Systems*, **14**(2):4–13, 1994.

[SSC03] Bhim Singh, Brij N Singh, Ambrish Chandra, Kamal Al-Haddad, Ashish Pandey, and Dwarka P Kothari. "A review of single-phase improved power quality AC-DC converters." *Industrial Electronics, IEEE Transactions on*, **50**(5):962–981, 2003.

[SSP03] VB Sriram, Sabyasachi SenGupta, and Amit Patra. "Indirect current control of a single-phase voltage-sourced boost-type bridge converter operated in the rectifier mode." *Power Electronics, IEEE Transactions on*, **18**(5):1130–1137, 2003.

[SZQ04] Juan Shi, R Zmood, and L Qin. "Synchronous disturbance attenuation in magnetic bearing systems using adaptive compensating signals." *Control Engineering Practice*, **12**(3):283–290, 2004.

[TGT16] Nolan Tsuchiya, Steve Gibson, Tsu-Chin Tsao, and Michel Verhaegen. "Receding-Horizon Adaptive Control of Laser Beam Jitter." *IEEE/ASME Transactions on Mechatronics*, **21**(1):227–237, 2016.

[TGV13] Jonathan Tesch, Steve Gibson, and Michel Verhaegen. "Receding-horizon adaptive control of aero-optical wavefronts." *Optical Engineering*, **52**(7):071406–071406, 2013.

[TMM12] Teng-Tiow Tay, Iven Mareels, and John B Moore. *High performance control*. Springer Science & Business Media, 2012.

[Tsa94] Tsu-Chin Tsao. "Optimal feed-forward digital tracking controller design." *Journal of dynamic systems, measurement, and control*, **116**(4):583–592, 1994.

[TTC89a] Masayoshi Tomizuka, Tsu-Chin Tsao, and Kok-Kia Chew. "Analysis and synthesis of discrete-time repetitive controllers." *Journal of Dynamic Systems, Measurement, and Control*, **111**(3):353–358, 1989.

[TTC89b] Masayoshi Tomizuka, Tsu-Chin Tsao, and Kok-Kia Chew. "Analysis and synthesis of discrete-time repetitive controllers." *Journal of Dynamic Systems, Measurement, and Control*, **111**(3):353–358, 1989.

[VBL13] Gijs van der Veen, Marco Bergamasco, Marco Lovera, Michel Verhaegen, et al. "Closed-loop subspace identification methods: an overview." *IET Control Theory & Applications*, **7**(10):1339–1358, 2013.

[WCT09] Yigang Wang, Kevin C Chu, and Tsu-Chin Tsao. "Adaptive Control for Deterministic Trajectory Tracking and Random Disturbance Rejection With Application to Nano-Precision Positioning of a Halbach Linear Motor." In *Proceedings of the ASME 2009 Dynamic Systems and Control Conference DSCC2009 October*, pp. 12–14, 2009.

[WJ97] Simon Wall and Robin Jackson. "Fast controller design for single-phase power-factor correction systems." *Industrial Electronics, IEEE Transactions on*, **44**(5):654–660, 1997.

[WT86] John P Whitacre and HG Trainer. "Piston pin bore treatments for high performance diesel engines." Technical report, SAE Technical Paper, 1986.

[WW08] Bernard Widrow and Eugene Walach. *Adaptive inverse control, reissue edition: a signal processing approach*. John Wiley & Sons, 2008.

[ZCS02] Richard Zhang, Mark Cardinal, Paul Szczesny, and Mark Dame. "A grid simulator with control of single-phase power converters in DQ rotating frame." In *Power Electronics Specialists Conference, 2002. pesc 02. 2002 IEEE 33rd Annual*, volume 3, pp. 1431–1436. IEEE, 2002.

[ZS01] Shiyu Zhou and Jianjun Shi. "Active balancing and vibration control of rotating machinery: a survey." *Shock and Vibration Digest*, **33**(5):361–371, 2001.

[ZW03] Keliang Zhou and Danwei Wang. "Digital repetitive controlled three-phase PWM rectifier." *Power Electronics, IEEE Transactions on*, **18**(1):309–316, 2003.

[ZZW08] Peng Zhai, Cheng-rui Zhang, Xin-liang Wang, Lei Qin, and You-zhi Qin. "Novel mechanism for boring non-cylinder piston pinhole based on giant magnetostrictive materials." *Journal of Shanghai University (English Edition)*, **12**:363–367, 2008.